Università degli Studi di Modena e Reggio Emilia

Dipartimento di Scienze Fisiche, Informatiche e Matematiche

Corso di Dottorato di Ricerca in Physics and Nano Sciences

Unravelling the tribochemistry of organometallic complexes at iron interfaces by ab-initio simulations

Relatrice

Prof.ssa M. Clelia Righi

Candidato

Stefan Peeters

Coordinatore del Corso di Dottorato

Prof. Stefano Frabboni

Ciclo XXXIII

Acknowledgements

I wish to express my gratitude to my supervisor, Prof. M. Clelia Righi, for her guidance and her constant encouragement during these years. Her great motivation is an example for many young scientists and students and I consider myself lucky to have been accepted in her research group in the first place.
Thanks to the collaboration with Total S.A. I had the valuable opportunity to stay for three months at the Solaize Research Center in Lyon to work with many dedicated people among which I wish to acknowledge Sophie Loehlé, Denis Lançon and Benoit Thiebaut for their support and kindness.
I consider Paolo Restuccia, Michael Wolloch and Alessandra Ciniero, former members of the group, as mentors during these three years. Their advice was a compass both inside and outside work for which I am very grateful. I wish them a very successful life ahead.
I am very thankful for the company of Giulio Fatti as a colleague and as a friend. The discussions with him and his initiative made my PhD experience much richer. I also thank my other colleague, Gabriele Losi, for his constant support and friendship since the very beginning of this path.
Thanks to Celeste Maschio, Giulia Righi and Jacopo Fregoni for their invaluable help, discussions and for making the time spent in Modena happier.
At the Physics department of the University of Modena I received the help of many, among which I would like to thank Prof. Mauro Ferrario and Prof. Carlo Calandra for their support and valuable discussions, and Prof. Franca Manghi and Prof. Rita Magri for the very fulfilling experience of explaining the exercises of their course to the bachelor's students.
At these lectures I met Chiara Corsini, with whom I had the pleasure to work on one of the chapters of this thesis. I deeply thank her for her contributions and her valuable company.
Outside the university I would like to thank my lovely parents and my dearest friend Matteo Zaganelli. A special thought goes to who provided me with their selfless support during this experience.

Contents

Introduzione **5**

Introduction **6**

1 Theoretical background **8**
1.1 Tribology in a nutshell . . . 8
1.2 Mechanochemistry and tribochemistry . . . 10
1.3 Computational approaches to unravel tribochemical reactions . . . 11
1.4 Materials to reduce friction . . . 13
1.4.1 Friction modifier additives . . . 14
1.4.2 Solid lubricants . . . 15

2 Characterization of Molybdenum Dithiocarbamates by First-Principles Calculations **18**
2.1 Introduction . . . 18
2.2 Methods . . . 19
2.3 Results and discussion . . . 20
2.3.1 The standard MoDTC complex . . . 20
2.3.2 Fragmentation of sMoDTC . . . 21
2.3.3 Isomers and oxidized molecules . . . 23
2.3.4 Partial charges on Mo atoms . . . 30
2.3.5 Role of the carbon chain . . . 31
2.3.6 Simulation of vibrational spectra . . . 32
2.3.7 Effect of the solvent on the molecular structure . . . 34
2.4 Conclusions . . . 37

3 Tribochemical Reactions of MoDTC Lubricant Additives with Iron by Quantum Mechanics/Molecular Mechanics Simulations **39**
3.1 Introduction . . . 39
3.2 Methods and systems . . . 40
3.3 Results and Discussion . . . 43
3.3.1 QM/MM simulations . . . 43
3.3.2 Adsorption and dissociation on iron . . . 45
3.3.3 Discussion . . . 48
3.4 Conclusions . . . 49

4 The Run-In Period of MoDTC Lubricant Additives: The Effect of Surface Oxidation by QM/MM Simulations and Tribological Experiments **50**
4.1 Introduction . . . 50
4.2 Methods and Systems . . . 51
4.2.1 Experimental Techniques . . . 51

4.2.2 Computational Approach . . . 51
4.3 Results and Discussion . . . 53
4.3.1 Characterization and Tribological Tests on the Oxidized Surfaces . . . 53
4.3.2 Molecular Adsorption and Dissociation in Static Conditions . . . 55
4.3.3 Molecular Adsorption and Dissociation in Tribological Conditions . . . 56
4.3.4 Discussion . . . 57
4.4 Conclusions . . . 59

5 Experimental and Ab-Initio Characterization of Mononuclear Molybdenum Dithiocarbamates in Lubricant Mixtures 60
5.1 Introduction . . . 60
5.2 Methods . . . 61
5.2.1 Experimental techniques . . . 61
5.2.2 Computational techniques . . . 62
5.3 Results . . . 63
5.3.1 Separation of S525 and characterization of the collected fractions . . . 63
5.3.2 Characterization and tribological test of the collected fractions . . . 64
5.3.3 Calculated molecular properties . . . 66
5.3.4 Fragmentation of isolated mMoDTC . . . 67
5.3.5 Chemisorption and fragmentation on iron . . . 69
5.4 Conclusions . . . 73

6 Adsorption and Dissociation of Ni(acac)$_2$ on Iron by Ab Initio Calculations 75
6.1 Introduction . . . 75
6.2 Methods . . . 75
6.3 Results and Discussion . . . 76
6.3.1 Properties of isolated Ni(acac)$_2$ . . . 76
6.3.2 Adsorption and fragmentation on iron . . . 80
6.3.3 Bond dissociation on iron . . . 81
6.4 Conclusions . . . 83

7 Final remarks and future perspectives 85
7.1 Future perspectives . . . 86

Appendices 87

A Supporting Information for: Characterization of Molybdenum Dithiocarbamates by First Principles Calculations 88
A.1 Convergence test on the relative stability of isomers . . . 88
A.2 Comparison of calculated structural data with experiments . . . 88
A.3 Comparison between the computer programs . . . 91
A.3.1 Formation energy of sMoDTC . . . 91
A.3.2 Energy difference between isomers and sMoDTC . . . 91
A.3.3 Energy difference between substituted compounds and sMoDTC . . . 92
A.4 Partial charges . . . 93
A.5 Experimental IR spectrum of MoDTC . . . 93

B Supporting Information for: Tribochemical Reactions of MoDTC Lubricant Additives with Iron by Quantum Mechanics/Molecular Mechanics Simulations **96**
B.1 Preparation of the QM/MM systems 96
B.2 Cutoff for the kinetic energy of the wave functions 96
B.3 Details on the dissociation of MoDTC complexes on iron 96

C Reorganization of central units of MoDTC to form amorphous MoS_x **98**
C.1 Methods and Systems 98
C.2 Results 100

D Supporting Information for: Experimental and Ab-Initio Characterization of Mononuclear Molybdenum Dithiocarbamates in Lubricant Mixtures **103**
D.1 Concentration of sulfur and molybdenum in the collected fractions 103
D.2 Electronic spectra 103

E Supporting Information for: Adsorption and Dissociation of $Ni(acac)_2$ on Iron by Ab Initio Calculations **105**
E.1 Convergence test 105

Introduzione

L'attrito è un fenomeno comune che si verifica ogni volta che due materiali in contatto si trovano in moto relativo. Dissipazioni dovute all'attrito causano enormi costi dal punto di vista energetico ed ambientale. Si è stimato che circa il 25% dell'energia impiegata nei trasporti e nella produzione industriale viene persa a causa dell'attrito. Comprendere l'attrito e come controllare i fenomeni tribologici è un compito di fondamentale importanza che ha coinvolto gli sforzi della comunità scientifica sin dagli inizi della scienza moderna. Buona parte della complessità dei fenomeni tribologici risiede nel gran numero di processi chimici e fisici che si verificano durante lo scorrimento all'interfaccia sepolta, che è particolarmente difficile da caratterizzare sperimentalmente in tempo reale. Le simulazioni al calcolatore, ed in particolare le simulazioni da principi primi, offrono la possibilità di descrivere accuratamente le interazioni tra superfici a contatto e monitorare i meccanismi tribologici. Questa tesi esplora le proprietà chimico-fisiche di complessi organometallici che sono - o potrebbero essere - di particolare interesse per la tribologia. Questo lavoro si concentra principalmente sulla reattività tribochimica dei ditiocarbammati di molibdeno (MoDTC), additivi lubrificanti ampiamente usati nell'industria automobilistica. Sono noti per via della loro capacità di formare disolfuro di molibdeno (MoS_2) in condizioni tribologiche, un materiale in grado di ridurre l'attrito dell'acciaio di circa un ordine di grandezza. Comprendere il meccanismo di funzionamento di questi additivi sui substrati metallici è essenziale per il design di additivi lubrificanti innovativi e più sostenibili. In questo lavoro presentiamo un completo studio ab initio del MoDTC. Sono riportate proprietà strutturali, elettroniche e vibrazionali di questi composti, assieme alle loro energie di dissociazione e le loro stabilità relative. L'ossidazione del MoDTC è stata esplorata in diverse condizioni ed è stata identificata la posizione più favorevole per gli atomi di ossigeno nel composto. Presentiamo una descrizione dei primi istanti della reazione tribochimica del MoDTC sul substrato di ferro grazie a simulazioni dinamiche secondo lo schema Quantum Mechanics/Molecular Mechanics (QM/MM), che ha permesso di chiarire il meccanismo dissociativo di MoDTC dibattuto da lungo tempo. Test tribologici e calcoli ab initio, sia in condizioni statiche che dinamiche, hanno permesso di spiegare il ruolo dell'ossidazione superficiale dei substrati nei primi stadi della dissociazione e di fornire una prima descrizione sistematica del MoDTC mononucleare, una forma alternativa dell'additivo che si trova nelle miscele lubrificanti. Un altro composto studiato in questa tesi è il nichel acetilacetonato, $Ni(acac)_2$, un noto precursore di molte specie chimiche differenti per via delle sue proprietà catalitiche. Questo composto non è mai stato preso in considerazione in ambito tribologico, ma è interessante studiare la sua interazione con substrati metallici perché la sua reattività può cambiare in presenza di sollecitazioni meccaniche. Poiché le nostre simulazioni hanno mostrato un completo accordo fra i meccanismi di dissociazione di MoDTC e $Ni(acac)_2$, proponiamo qui una possibile generalizzazione di tale modello dissociativo. Un altro importante risultato del lavoro è aver applicato per la prima volta tecniche QM/MM per lo studio degli additivi lubrificanti. L'accordo degli esperimenti in silico con quelli eseguiti in laboratorio nell'ambito di questo stesso progetto dimostra che l'approccio computazionale che abbiamo introdotto è un valido strumento di indagine che può essere utilizzato con successo per disegnare nuovi additivi lubrificanti e più in generale materiali per ridurre l'attrito.

Introduction

Friction is a common phenomenon that occurs every time two materials in contact are in relative motion. Energy losses due to friction cause huge energetic and environmental costs. In fact, it has been shown that approximately 25% of the total energy consumed in transportation, power generation and manufacturing is lost due to friction [1]. This massive energy consumption can be reduced by improving the technologies to reduce friction. Holmberg and Erdemir showed in 2017 that it would be possible to reduce the energy losses by 40% in 15 years by improving tribology [2]. Understanding friction and how to control tribological phenomena is a task of fundamental importance that has been involving the effort of the scientific community since the birth of modern science. The microscopic origin of friction still needs to be completely understood, because the tribological phenomena can be very difficult to describe. Most of the complexity of these phenomena resides in the wide number of chemical and physical processes that occur at the sliding buried interface, which is very hard to characterize experimentally. Computer simulations offer the possibility to elucidate tribological mechanisms at the molecular level in real time. First principles simulations are particularly suited for this task because they can accurately describe both the electronic and ionic degrees of freedom, which are important to model tribochemical reactions, i.e. the chemical reactions occurring in the presence of mechanical stresses. Compression and shear forces can in fact promote chemical reactions similarly to light and heat and studying tribochemistry is essential to fully understand the mechanism of function of lubricant materials. Among them, friction modifiers and solid lubricants are of particular relevance: the former are added to liquid lubricants and mainly operate in the boundary lubrication regime, where the oil is squeezed out from the interface and the asperities of the material are in contact, while the latter are used in dry conditions and mostly operate by separating and protecting the surfaces while offering low resistance to sliding.

This thesis explores the physico-chemical properties of organometallic complexes that are - or could be - of particular interest for tribology. The core of this work focuses on the tribochemical reactivity of molybdenum dithiocarbamates (MoDTCs), organomolybdenum friction modifier additives widely used in the automotive industry. They are well-known compounds because of their capability to form molybdenum disulfide (MoS_2) in tribological conditions, which is a solid lubricant composed by layers that can reduce the friction of steel of around one order of magnitude [3]. Understanding the mechanism of function of these additives and their interaction with the metallic substrates is essential to optimize currently employed lubricant mixtures, to reduce their negative impact on the environment and to gain valuable insight for the design of innovative and more sustainable friction modifiers. The work concerning the tribochemistry of MoDTC is organized as follows:

- Chapter 2 contains a comprehensive ab-initio study of the properties of MoDTC. Structural, electronic and vibrational data of the standard MoDTC chemical structure are reported, along with the energies to dissociate the isolated complex, the relative stability of different MoDTC structures and the role of oxygen in these compounds. Oxidation of MoDTC structures was explored for a wide range of conditions and the most favorable position for oxygen atoms in MoDTC was identified. Supporting information for this work is included in Appendix A.

- Chapter 3 describes the initial steps of the tribochemical reaction of MoDTC on the iron substrate. Dynamic simulations following the scheme of Quantum Mechanics/Molecular Mechanics (QM/MM)

allowed to monitor in real time the tribochemical reactions occurring at the iron interface. This study aims at clarifying the debated dissociation mechanism of MoDTC. Supporting information for this work is included in Appendix B, while a preliminary study concerning the reorganization of central units of MoDTC to form an amorphous MoS_x structure is presented in Appendix C.

- Chapter 4 focuses on the role played by oxygen on the metallic substrate in the tribochemistry of MoDTC. Tribological tests and ab initio calculations, both in static and tribological conditions, were combined to investigate the role of surface oxidation in the first dissociative steps of the additives which lead to the formation of the beneficial MoS_2 tribolayers.

- Chapter 5 contains the first systematic study on mononuclear MoDTC, one of the alternative forms of standard MoDTC present in the lubricant mixtures, by a combined experimental and computational approach. The mononuclear form of MoDTC could be in equilibrium with the most common dimeric structures and most likely presents different tribological properties than the dimers because of their different chemistry. Supporting information for this work is included in Appendix D.

Another complex considered in this thesis is nickel acetylacetonate, $Ni(acac)_2$, a well-known precursor for many different chemical species due to its catalytic properties. This compound was never studied for tribological purposes, yet its interaction with metallic substrates is worthy to explore because its reactivity might change in the presence of mechanical stresses. Chapter 6 reports a preliminary study on the adsorption and the dissociation of this complex. After an evaluation of structural and electronic properties of $Ni(acac)_2$, the comparison between different dissociation patterns reveals that the most favorable pattern for the complex adsorbed on iron is different from the one suggested by considering the strength of the bonds in the isolated complex, in complete analogy with the results observed for MoDTC. An attempt to generalize this dissociation model is made in this work. Supporting information for this work is included in Appendix E.

Another important achievement of this work is the innovative application of QM/MM techniques for the study of lubricant additives. The agreement between the in silico experiments and the ones carried out in the laboratory in the framework of this project demonstrates that the computational approach we introduced is a valid investigation tool that can be successfully employed for the design of new lubricant additives and, more generally, new materials to reduce friction.

Chapter 1

Theoretical background

This chapter introduces the theoretical foundations of tribochemical reactions. After a brief summary of the most relevant discoveries in tribology, the following topics will be presented: the concepts of mechanochemistry and tribochemistry, along with few examples, a brief overview of successful computational methods to study tribochemical reactions, and finally common materials to reduce friction.

1.1 Tribology in a nutshell

Tribology is the science of friction, lubrication and wear. It is multidisciplinary, encompassing physics, chemistry, mechanics and materials science.

Practical problems related to friction affected humanity since the beginning of history. In ancient times these problems were solved heuristically and smart solutions were found by employing the materials available in the environment [4]. The first systematic studies on dry friction were carried out by Leonardo da Vinci more than two centuries before Newton. However da Vinci never published his studies, that remained unknown for nearly two more centuries, since the establishment of modern science. In the 17^{th} century Guillaume Amontons re-discovered these laws, stating that friction is directly proportional to the applied load and independent of the contact area:

$$F_{\text{friction}} = \mu F_{\text{load}} \tag{1.1}$$

where the proportionality constant μ is the coefficient of friction, an empirical property of the sliding materials. In 1785, Charles Augustin de Coulomb confirmed experimentally the Amontons' laws and found also that the kinetic friction does not depend of the sliding velocity. Furthermore, he understood that the origin of friction was to be searched at smaller scales: microscopic asperities and the cohesion between the sliding surfaces have a major impact in determining friction [5]. These findings constitute the foundation of the theory of dry friction.

The industrial developments occurred in the 19th century required to effectively control friction. Lubrication of the sliding surfaces is one of the most efficient ways of reducing friction. In the 19^{th} century, several scientists such as Osborne Reynold [6] and Richard Stribeck [7, 8] contributed to the phenomenological understanding of lubricated friction, resulting in the introduction of the Stribeck curve, reported in Figure 1.1. This curve identifies three different lubricating regimes, boundary lubrication, mixed and hydrodynamic regimes, as a function of the sliding velocity, the applied load and the lubricant viscosity.

Although these important advances provided a phenomenological description of friction at the macroscopic level, the underlying mechanism of friction at smaller scales were still mostly unexplored. During the 50's, Frank Philip Bowden and David Tabor provided new insights on the connection between macro- and microscopic friction, by introducing the concepts of real area of contact, composed by many nano-asperities interacting among each other, and adhesive friction and wear [9]. The development of the groundbreaking technology of the Surface Forces Apparatus (SFA) by Tabor and Jacob Nissim Israelachvili [10, 11] revealed

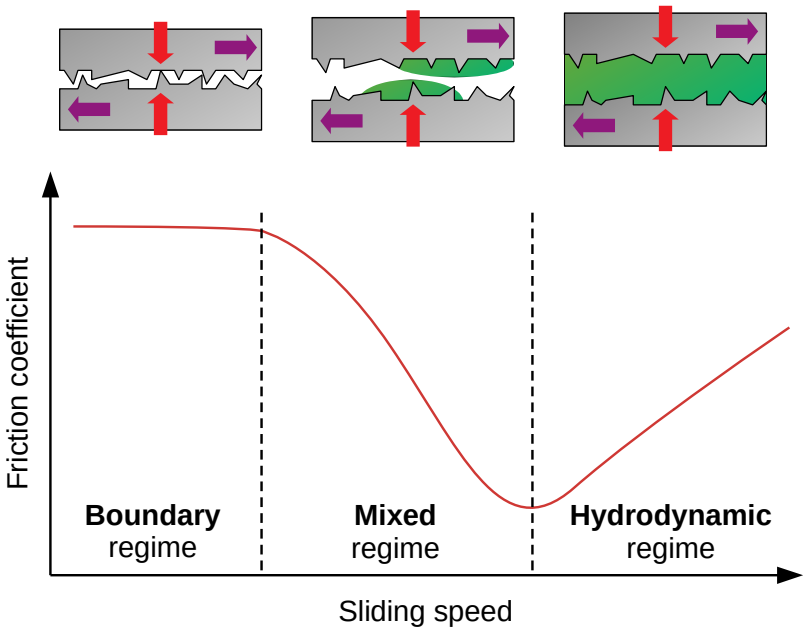


Figure 1.1: The Stribeck curve identifies three friction regimes. In the boundary lubrication regime, low speeds and high loads generate high friction coefficients. In fact, the lubricant is squeezed out of the interface because the asperities are in contact. The friction drop starts with the mixed lubrication regime, reaching a minimum at the beginning of the hydrodynamic regime.

that friction forces can be experienced even in the presence of negative loads. This effect, which cannot be observed at the macroscopic scale, is due to the adhesive forces of chemical and physical nature arising at the tribological interface.

The advent of new experimental techniques paved the way for the development of nanotribology. The first studies in this new field began with the advent of Atomic Force Microscopy (AFM) [12–14]. In this apparatus, a single-asperity tip is connected to a cantilever, whose deflections can measure normal forces. With later improvements, lateral forces could be measured as well, significantly reducing the complexity of the tribological problem by studying a single asperity instead of many. The new experimental observations, coupled with new theoretical models, allowed to describe the energy dissipation during sliding due to a stick-slip motion and identify the role of commensurability, i.e. the situation in which the atoms of one surface fall in the energy minima of the mated surface. Avoiding this interlocking mechanism between the two surfaces leads to the phenomenon of superlubricity [15]. Other electronic and optical techniques such as Auger Electron Spectroscopy (AES) and Low Energy Electron Diffraction (LEED) also provided new insights in tribology because it became possible to identify single crystal structures and the thin films adsorbed on the surfaces [16–18]. X-ray Photoelectron Spectroscopy (XPS) is another technique able to distinguish the chemical species present on the surfaces, their oxidation state and their chemical environment [19] and is a commonly employed technique to this day for the *post-mortem* characterization of tribological samples [20]. To better describe tribological events at the atomistic level, computer simulations

were employed as a powerful tool, mainly in the form of Molecular Dynamics (MD) [21], as described in detail in Section 1.3.

1.2 Mechanochemistry and tribochemistry

Mechanochemistry is the branch of chemistry that focuses on the chemical reactions induced by mechanical stresses, such as compression and shear. Since the ancient times, rubbing and grinding have always been common techniques to manipulate materials. Modern mechanochemistry begins in the nineteenth century, when Matthew Carey Lea described for the first time how certain compounds reacted differently under the effect of mechanical stresses and heat. He observed that silver and mercuric halides decomposed by trituration in a porcelain mortar, while they remained undecomposed when heated [22]. The term *mechanochemistry* was invented by Wilhelm Ostwald in 1919, when he described mechanical stresses as one of the several ways to introduce energy in a system to promote chemical reactions, similarly to heat and light in the fields of thermochemistry and photochemistry [23]. Ball milling is one of the most used techniques to induce mechanochemical transformations. This technique has a long history, yet several technological advancements make ball milling a convenient technique to this day, because it allows the synthesis of many compounds in the absence of solvents [24].

In tribological conditions, normal and shear stresses act on the chemical species present at the interface. The mechanochemical reactions occurring in tribological conditions are studied in the field of tribochemistry [25]. Most often the chemical species at the interface interact with surrounding compounds and substrates that can catalyze their reactivity. Furthermore, the heat generated to dissipate the frictional forces can influence the mechanism of these chemical reactions. Triboemission, that is the emission of particles or light induced by the mechanical stresses, can also occur. All these sources of complexity make tribochemical reactions a formidable problem to tackle.

When heat promotes chemical reactions, an Arrhenius equation can be used to describe the relationship between the local temperature and the reaction rate, as in Equation 1.2:

$$k \propto \exp \frac{-\Delta E_a}{RT} \tag{1.2}$$

where k, ΔE_a, R and T are the rate constant, the activation energy, the universal gas constant and the absolute temperature, respectively. Atomic-scale mechanochemical processes promoted by stresses can be described by an Arrhenius-like equation [26, 27]:

$$k \propto \exp \frac{-\Delta E_a + \sigma \Delta V_a}{RT} \tag{1.3}$$

where σ and ΔV_a correspond to the stress component assisting the tribochemical reaction and the activation volume, respectively. The activation volume is a tensor with six independent components which describes the relationship between the barrier height and the six components of stress. Most often, one stress component will be dominant and therefore ΔV_a can be written as a scalar quantity. In this case, the activation volume represents the volume over which the stress must be dissipated for the reaction to occur [28]. However, the physical interpretation of the activation volume is the subject of active research to this day because it is still a debated concept.

Among the tribochemical reactions that involve the lubricants, oxidation is one of most common, and it is often undesired. The hydrocarbon chains constituting the lubricant oil, in fact, can host additional oxygen atoms when they experience high temperatures and stresses. This phenomenon leads to the formation of

peroxides, responsible for corrosive wear [29, 30]. Antioxidants are molecules designed to minimize the effects of oxygen on the lubricant, by offering alternative destinations for the oxygen atoms and avoiding the degradation of the molecules of the oil [31, 32]. Oxidation can involve also the substrates, because the removal of material due to wear can expose native surfaces that can quickly react with the environmental molecules, with a possible impact on the mechanical properties of the solid [25, 33]. The role of oxygen in the tribochemistry of molybdenum dithiocarbamate additives will be described in the following chapters of this thesis.

Another remarkable example of tribochemical reactions is the decomposition of the additives and the release of key elements that modify the chemical composition of the surface, with a consequent modification of adhesion and friction. Extreme pressure (EP) additives, which are active in the regime of boundary lubrication, break down at the asperity contact and form protective tribofilms that prevent the formation of bonds across the interface which can cause the seizure of the moving parts [34, 35]. Polymerization and cross-linkage can occur for hydrocarbons and amorphous carbon materials under mechanical stresses [36–38]. Such chemical transformations can generate complex carbon nanostructures, with different sp^2/sp^3 ratios, able to spatially separate the two surfaces in motion and minimize the chemical interactions between them [39, 40].

A major source of complexity in tribochemical reactions resides in the fact the tribological interface is buried, hence not directly observable by the experiments. Therefore, the reaction mechanisms must often be inferred a posteriori. After performing the tribological tests, the surfaces are then characterized to identify their morphology and the deposited chemical species, often by means of optical microscopy, vibrational spectroscopies and other spectroscopic techniques such as XPS and AES. However, this approach can be sometimes questionable, because it is necessary to separate the two bodies before the analysis. In this way, the worn surfaces immediately interact for a certain time with other molecules present in the liquid lubricant or in the environment. Cleaning procedures can also influence the surface chemistry when the residual liquid lubricant is removed. Therefore it is quite hard to judge whether the surface chemistry identified post-mortem can be really representative of that during the lubricated contact.

On one hand, innovative experimental techniques aim at providing new insights on the boundary lubrication regime and the mechanism of activation of the tribochemical reactions. In gas-phase lubrication (GPL), the lubricant molecules in the vapor phase are put directly at the tribological contact, avoiding the interaction with the liquid lubricant and simplifying the tribochemical problem. Methods of characterization usually coupled to GPL are Raman and infrared spectroscopy [41, 42], AES and XPS [43], sometimes even carried out in situ. GPL allowed to shed light on the tribochemistry of volatile molecules such as tetrachloromethane [44], trimethylphosphite [45, 46] and other S- and P- based additives [47, 48], alcohols and thiols [49, 50], water and hydrogen [51]. On the other hand, computer simulations emerged in recent years as particularly handy tools to describe reaction mechanisms at the atomistic level, as they allow to monitor the chemical modifications occurring at the buried interface without the technical limitations imposed by the experiments. A brief description of the state of the art in the computational methods applied to tribochemistry will be given in the next Section.

1.3 Computational approaches to unravel tribochemical reactions

Tribological events involve mechanical, physical and chemical phenomena at different scales. While mechanical deformations, fractures, wear are better described by considering the mesoscale (between nano- and micrometers), describing how chemical bonds form and break requires an accurate description of the nanoscale. Computational tools offer the possibility to simulate most of these phenomena in controlled

conditions, without the technical limitations which are unavoidable in experiments. The computational methods employed to investigate the nanoscale are of particular interest for this thesis work.

Molecular dynamics (MD) simulations emerged in the last decades as a valid tool to model the tribological buried interface and its transformations in real time. In MD, the forces between the atoms of the system are calculated at each time step and it is possible to obtain the trajectory of these atoms by numerically solving an equation of motion. In classical MD the forces are calculated as the gradient of potentials describing the atom-atom interactions, commonly referred to as *force fields*, which are parametrized empirically. Classical force fields cannot accurately describe bond formation and breaking, because they are built to represent structures at equilibrium. Reactive force fields, such as the reactive empirical bond-order (REBO) method [52–55], its extension by Stuart et al. (AIREBO) [56] and ReaxFF [57], were developed to overcome this limitation, yet they were not designed to describe systems under confinement and mechanical stresses. Therefore, this type of force fields may not be particularly accurate to simulate the reactivity in tribological systems, where the electronic structure can be heavily destabilized by the mechanical stresses.

First principles or *ab initio* simulations, based on the laws of quantum mechanics, are the appropriate tool to describe the electronic structure of the species in such complex environments, at the cost of computational power. Density functional theory (DFT) is a remarkably efficient compromise between the desired accuracy and the computational resources. Any system containing N electrons needs to be described by a wave function with $3N$ variables in quantum mechanics, hence simulating extended systems is a formidable task. The key quantity in DFT is the electronic density, which only relies on 3 variables regardless of the number N of electrons in the system, providing an evident simplification to the many-body problem. DFT was developed in 1964 by Pierre Hohenberg and Walter Kohn, who proposed two fundamental theorems: the total energy of the system is a unique functional of the electronic density of the ground state and such a functional is minimized by the correct ground state density [58]. One year later, Walter Kohn and Lu Jeu Sham proposed that each interacting system can be described by a single-particle effective potential of a non-interacting system with the same ground state density [59]. In the Kohn-Sham formalism, the problem of finding an analytical expression for the energy functional is shifted to only one of its contributions, the exchange-correlation functional, for which many approximation have been proposed during the years.

DFT can be used to carry out static or dynamic calculations. In both cases external forces and velocities may be applied to some of the atoms of the simulation cell, allowing to reproduce the effect of mechanical stresses. Typical static calculations allow to perform geometry optimizations, driven by an energy minimization algorithm, the evaluation of electronic [60–65], vibrational [66–68] and mechanical properties [69–73] and can even provide insight on reaction paths and energy barriers [74–78], while dynamic calculations allow to monitor the time evolution of tribological systems, the trajectory of the atoms and the effect of temperature [79–81]. The dynamic calculations in which the forces on the atoms are calculated by a quantum mechanical engine are called ab-initio molecular dynamics (AIMD) simulations, and our group has been pioneer in the use of AIMD to describe tribochemical reactions [79, 82–84]. Two approaches are possible for the AIMD in the framework of DFT:

- In the Car-Parrinello (CP) method [85], the electronic configuration is optimized only at the initial step and the electronic degrees of freedom are then propagated as fictitious dynamic variables, leading to a system of coupled equations of motion for both ions and electrons. In this way, it is possible to avoid the minimization of the electronic structure at each step of the dynamic simulation. In order to maintain the electrons in the ground state, the fictitious electronic mass must be chosen small enough to avoid undesired energy transfer from the ionic to the electronic degrees of freedom. However, the simulation time steps in CP are smaller (of the order of 0.1 fs) than the ones of the Born-Oppenheimer approach, thus requiring more steps to obtain equivalent simulation times. This method was proven

successful to describe the effect of water in the lubrication of diamond [80], carbon-coatings [83] and MoS_2 [79].

- In the Born-Oppenheimer (BO) method [86], the ionic degrees of freedom are propagated using the Hellmann-Feynman forces calculated at each simulation step, making this approach more computationally expensive than the CP method. However, typical simulation time steps are of the order of 1 fs, i.e. larger than in the CP approach, yet still smaller than the period of the quickest ionic vibrations. This method was successfully used to describe the formation of iron phosphide from organophosphorus additives [84] and the tribochemical conversion of methane to graphene [40].

To reduce the computational effort associated to fully ab-initio MD, hybrid schemes can be adopted. In the quantum mechanics/molecular mechanics (QM/MM) approach [87, 88] the simulation system is divided in two different regions: the quantum region, where energies and forces are calculated at the quantum level, and the classical region, where only force fields are employed to evaluate energy and forces. This allows to focus the computational power on the portion of the system where the chemical reactions occur and where the high accuracy is needed, without spending unnecessary resources on the portion of the system where the details of the electronic structure are not needed. The total energy of the whole system can be obtained in different ways [89]. In the additive scheme, one would need to compute separately the total energy of the quantum and the classical subsystems and their interaction:

$$E_{add} = E^{I}_{QM} + E^{II}_{MM} + E_{QM/MM} \tag{1.4}$$

where E^{I}_{QM}, E^{II}_{MM} and $E_{QM/MM}$ are the total energies of the chemically active region (region I) calculated at the quantum-mechanical level, the total energy of the classical system (region II) calculated by force fields, and the interaction between the two regions. An alternative is the subtractive scheme:

$$E_{sub} = E^{I+II}_{MM} - E^{I}_{MM} + E^{I}_{QM} \tag{1.5}$$

where E^{I+II}_{MM} and E^{I}_{MM} correspond to the total energies of the whole system and of the chemically active region calculated classically.

The QM/MM approach, which has been recently demonstrated by our group as a very promising tool for tribochemistry [90, 91], can be considered one of the most successful implementations of the multiscale modelling paradigm, i.e. the simultaneous description of phenomena at different scales [92].

1.4 Materials to reduce friction

A wide variety of solutions are available to reduce friction, based on different physico-chemical mechanisms. In liquid lubrication, one possible approach is to optimise the rheology of the lubricant, which often requires to reduce the lubricant viscosity to the lowest possible value to maintain the system in the hydrodynamic or mixed lubrication regimes. Another possibility is to add small quantities of extreme pressure and friction modifier additives to the liquid lubricant in order to reduce friction in the boundary and mixed lubrication regimes. Friction modifier additives will be described in Section 1.4.1. However, lubrication can be realized even in absence of a liquid medium. Section 1.4.2 briefly describes solid lubricants, which operate in dry conditions.

1.4.1 Friction modifier additives

A first class of friction modifier additives operate by modifying the properties of the lubricant oil without undergoing chemical reactions. In fact, organic friction modifiers (OFM), amphiphilic surfactant molecules containing a polar head group and an alkyl tail, can self-assemble into close-packed monolayers, with the possibility to sustain high loads thanks to the cumulative Van der Waals forces between the alkyl chains [93]. Examples belonging to this class are free fatty acids derived from fats and vegetable oils [94], amides and esters [95, 96].

A second class of additives are small molecules containing elements such as phosphorus and sulfur that can be released on the surface after a tribochemical reaction. Organo-phosphorus and organo-sulfur additives are particularly effective in the boundary lubrication regime. They initially adsorb on the surfaces, then the extreme conditions of the tribological contact destabilize their chemical structure. The elements or the molecular fragments released on the surface can form films that prevent the welding of opposing asperities [84]. Zinc dialkyldithiophosphate (ZnDTP or ZDDP), containing both sulfur and phosphorus are probably the most successful lubricant additives ever invented [97]. At the tribological interface they can quickly form 50-200 nm thick films of glassy zinc phosphate/polyphosphate material which ensures protection from wear by acting as a barrier. ZDDPs can also decompose peroxides by acting as anti-oxidants and favor the formation of iron sulfides, which are less abrasive than wear particles composed by iron oxides [98].

Organo-molybdenum friction modifiers belong to this group of additives because they undergo tribochemical reactions leading to the formation of molybdenum disulfide (MoS_2). MoS_2 is known as a successful solid lubricant since the first half of the twentieth century, and molybdenum-containing compounds were introduced at the end of the 50's to overcome the problem of keeping MoS_2 in liquid lubricants [99, 100]. Two of the most studied organo-molybdenum friction modifiers are molybdenum dialkyldithiophosphate (MoDTP), molybdenum analogue of ZDDP, and molybdenum dialkyldithiocarbamate (MoDTC). MoDTP and MoDTC are actually classes of similar compounds which differ by the length of the lateral alkyl chains, the position and the relative ratio of oxygen and sulfur atoms in the chemical structures and the number of molybdenum atoms constituting the core metallic unit, even though the majority of the Mo-containing friction modifiers consists of dimeric structures. Yamamoto and Gondo in the 80's examined by XPS the films generated when MoDTP and MoDTC are added to the lubricant and they confirmed that the friction reduction was due to the formation of MoS_2 [3]. However, the mechanism of formation of the beneficial MoS_2 tribolayer, which is of particular interest for this thesis, remained unclear for a long time, despite its wide use in commercial products in automotive [101, 102]. In the following chapters several properties of MoDTC will be described: Chapter 2 will focus on the properties of the isolated complexes and the role of oxygen in these compounds, Chapters 3 and 4 will deal with the dissociation mechanism on clean and oxidized iron surfaces, respectively, and Chapter 5 is the first systematic study on the properties of mononuclear MoDTC, an alternative form of the additive present in lubricant mixtures.

Other two groups of friction modifiers are functionalized polymers and nanoparticles. The former are commonly employed as viscosity modifiers, yet their friction reduction performances were studied since the 60's [103, 104]. These polymers adsorb onto the sliding surfaces and form thick layers, up to tens of nanometers, that increase the viscosity of the lubricant close to the surfaces and are especially convenient in less severe, mixed lubrication regimes [93]. A notable example of such polymers are polymethacrylates [105, 106]. On the other hand, nanoparticles have recently emerged as possible alternatives to the friction modifiers described above. Carbon-based materials such as graphitic-like structures and fullerenes, metallic and inorganic structures may constitute the nanoparticles used to reduce friction, with sizes ranging from 1 to 500 nm, which allows them to remain dispersed in the lubricant without being stopped by common

oil filters. These nanoparticles often undergo mechanical transformations that lead to the formation of protective tribofilms [107]. Figure 1.2 includes a few examples of friction modifier additives from the different classes.

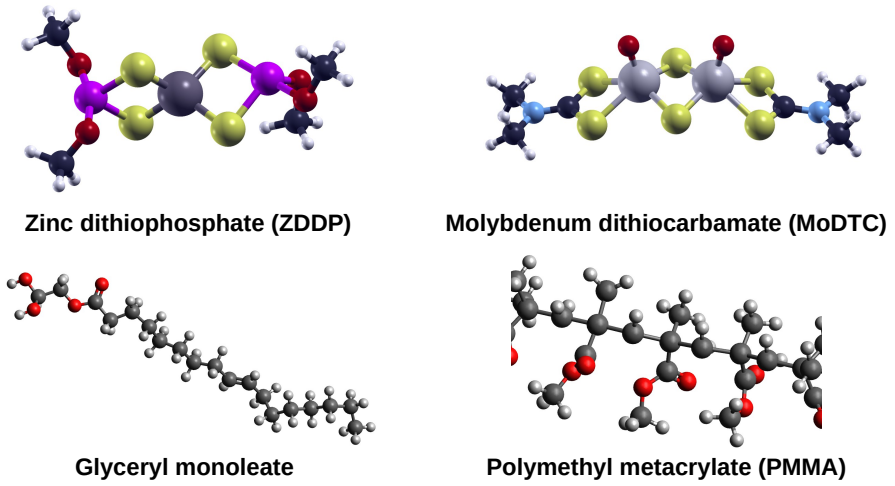


Figure 1.2: Examples of commonly employed friction modifier additives. Glyceryl monoleate belongs to the class of organic friction modifiers.

1.4.2 Solid lubricants

Coatings are another way of controlling friction and protecting surfaces in sliding motion in the absence of a liquid lubricant. Solid lubricating coatings are very efficient for industrial applications due to their exceptional chemical inertness, high mechanical strength and hardness, and excellent friction reduction and wear resistance properties. A few examples of these materials are shown in Figure 1.3

Polytetrafluoroethylene (PTFE), polyimide (PI), polyetheretherketone (PEEK), polyphenilene sulfide (PS) and polyoxomethylene (POM) are among the polymeric materials employed for solid lubrication. These polymers can be often found in multi-component materials to enhance their mechanical and physical properties, as in the case of PTFE/PEEK composites [108]. Furthermore, polymers in tribology are studied also for the phenomenon of triboelectricity, i.e. the generation of charge separation due to rubbing, with a particular interest for PTFE [109, 110].

MoS_2, the success of which was already introduced in the previous Section, and WS_2 are among the most representative transition metals dichalcogenides (TMDs), layered materials which belong to a second class of solid lubricants. Their mechanism of function relies on weak interlayer forces that offer very small resistance to sliding, with friction coefficients around 0.05 or lower. However, TMDs fail in the presence of humidity or oxygen, because of the formation of metallic oxides that make the generated tribofilms patchy and less durable [111, 112].

Carbon-based materials are among the most successful solid lubricants because carbon can take different forms such as graphene, diamond-like carbon (DLC) and (ultra)nanocrystalline diamond depending on their chemical structure, leading to a wide variety of physical and mechanical properties [113]. Graphite is

a versatile and well-known solid lubricant because it is composed of graphene layers that can easily slide on one another, as they are held together by weak Van der Waals forces. Graphene layers are two-dimensional hexagonal lattices of sp^2-hybridized carbon atoms. The high strength, chemical stability and easy shear capability make graphene an extremely valuable lubricant for nano- and macroscale applications.

DLC coatings are amorphous films of carbon with different sp^2-C/sp^3-C ratios and degrees of hydrogenation, leading to a wide variety of materials with different mechanical properties, as shown in the ternary phase diagram in Figure 1.4. DLC coatings can be divided in two major groups based on their hydrogen content: non-hydrogenated DLC coatings that include amorphous (a-C) and tetragonal (ta-C) DLC coatings with a negligible hydrogen content, and hydrogenated DLC coatings that include amorphous (a-C:H) and tetragonal (ta-C:H) DLC coatings containing a substantial amount of hydrogen. DLC coatings are nowadays being used in various fields of industry, for example, automotive, aerospace, electronics, optics, as well as for medical equipment.

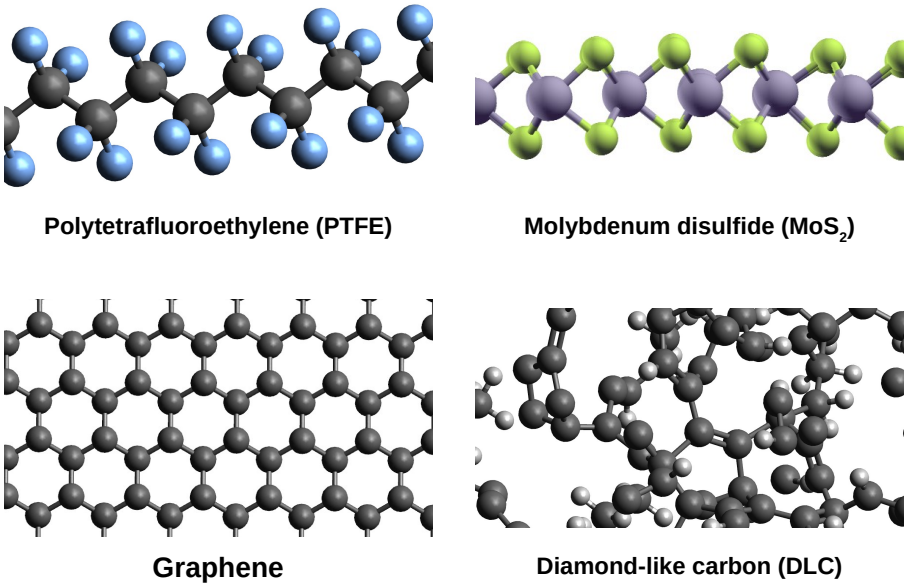


Figure 1.3: Examples of commonly employed solid lubricants.

Carbon-based materials present different tribological behaviors depending on the chemical species present in the environment. In particular, water can react with the tribological materials due to normal load and shear stress, and further influence friction and wear performances. Graphene is known to perform better in presence of humidity [114], and this phenomenon can be explained by the dissociative chemisorption of water, as well as hydrogen and oxygen, on the edges of graphene. This mechanism was confirmed both by experimental and computational investigations [28, 91, 115–117]. Water plays different roles in the lubrication of DLCs. Hydrogenated coatings perform better in dry or inert gas environments [118]. When the counter surface is a-C:H film as well, the rubbed surfaces are rich in single and double bonds between carbon and oxygen, in addition to C–C and C–H bonds. With other materials, such as metals and ceramics, transfer layers containing C and O can be found in the rubbed area. Generally, tribochemical reactions take place between the carbon films and water, resulting in O- and OH-terminated surfaces and leading to high

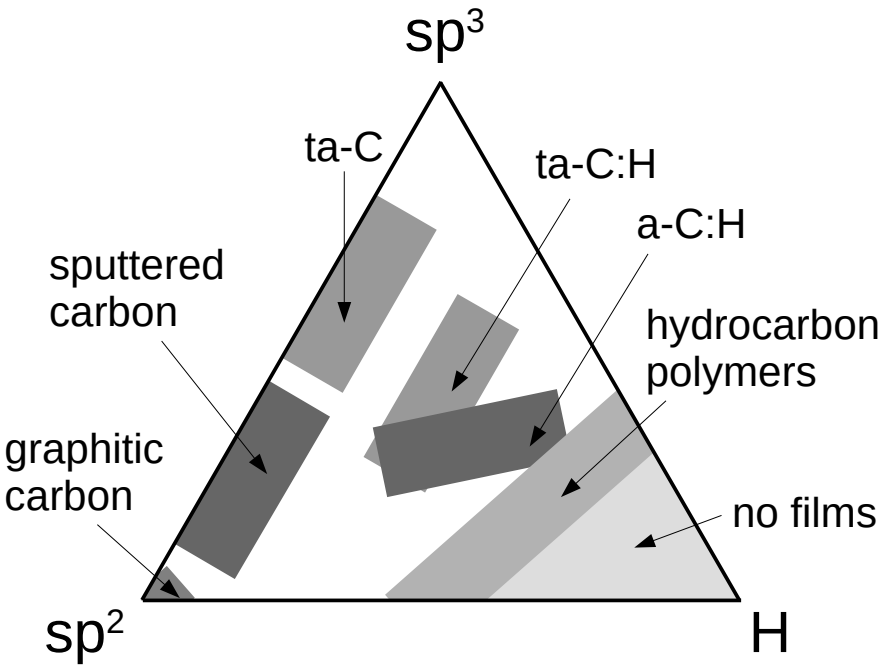


Figure 1.4: Ternary phase diagram of DLC materials.

friction coefficients [119]. Unlike a-C:H, humidity has a positive effect on the friction and wear of a-C films. In this case, the mechanism is very similar to that of graphene. Water molecules can in fact dissociate and passivate the layers of the material uncovered by rubbing, thus reducing the adhesion between the sliding surfaces [117].

One limitation of these systems is that they tend to wear out eventually due to their finite thickness and volumes. Therefore, high friction and wear may occur again, eventually. A smart way to overcome this difficulty is the design of lubricating materials able to self-replenish. The possibility to form graphitic films on top of surfaces by the action of mechanical stresses on the hydrocarbons at the interface is a remarkable achievement, and recent studies showed that these hydrocarbons could be olefins coming from the lubricant oil or even small gaseous molecules, such as methane, introduced in the tribological environment [38, 40].

Chapter 2

Characterization of Molybdenum Dithiocarbamates by First-Principles Calculations

2.1 Introduction

Molybdenum dithiocarbamates (MoDTC) are a class of widely employed lubricant additives for automotive applications. In tribological conditions, MoDTC is known to form MoS_2, a transition metal dichalcogenide able to reduce friction under boundary lubrication regime. While the remarkable performance of MoS_2 in reducing friction is well established, the process through which MoDTC forms MoS_2 is not clear at present. A remarkable source of complexity is given by the wide variety of compounds with different amounts of O atoms occupying different positions in the molecule that can be present simultaneously in the samples. Oxidation has been shown to influence the friction reduction performance of the MoDTC additive [120–122]. Therefore, De Feo *et al.* investigated the degradation of MoDTC due to atmospheric oxygen by employing high-performance liquid cromatography, vibrational spectroscopy and mass spectrometry [123]. They extended the dissociation mechanism of MoDTC proposed by Grossiord *et al.*, who suggested that MoDTC undergoes an homolytic breaking of the bonds between ligand sulfur atoms and molybdenum atoms as the starting point of the reaction [101]. De Feo *et al.* suggested that MoDTC undergoes two isomerization processes alternated with two oxidation processes before the bond breaking. Within this mechanism, MoDTC becomes richer in oxygen atoms which substitute sulfur atoms in ligand position. Khaemba *et al.* proposed a different mechanism, suggesting that each carbamate unit dissociates from the central $Mo_2O_2S_6$ unit through the breaking of the two C-S bonds [102]. However, the role of oxygen in MoDTC played in the dissociation of the molecule has not been clarified yet.

While literature concerning the tribological performance of MoDTC is wide, the data regarding the properties of the individual complexes are insufficient in order to distinguish them in real samples and make assumptions on their reactivity. In this work, we provide an *ab initio* characterization of MoDTC, fully based on density functional theory (DFT) calculations, by taking into account electronic and vibrational properties, the isomerization and oxidation processes. We present the optimized molecular geometry and the dissociation energy of MoDTC in three different dissociative paths. All the isomers obtained by exchanging oxygen and sulfur atoms in the standard structure of the molecule are considered along with more oxidized complexes. Partial charges on the molybdenum atoms are calculated, in order to identify in which conditions molybdenum atoms are reduced from the +5 oxidation state to +4, as in MoS_2. The role of the lateral alkyl chain of the carbamate units is studied and a comparison of the vibrational spectra of the different considered complexes is presented lastly. Our aim is to identify key features in isolated MoDTC complexes to ease the experimental characterization of real samples. Furthermore, the systematic analysis of several MoDTC isomers and substituted complexes allows to obtain a better understanding of

Reproduced with permission from **S. Peeters**, P. Restuccia, S. Loehlé, B. Thiebaut, M. C. Righi, J. Phys. Chem. A 2019, 123, 32, 7007-7015. Copyright 2019 American Chemical Society.

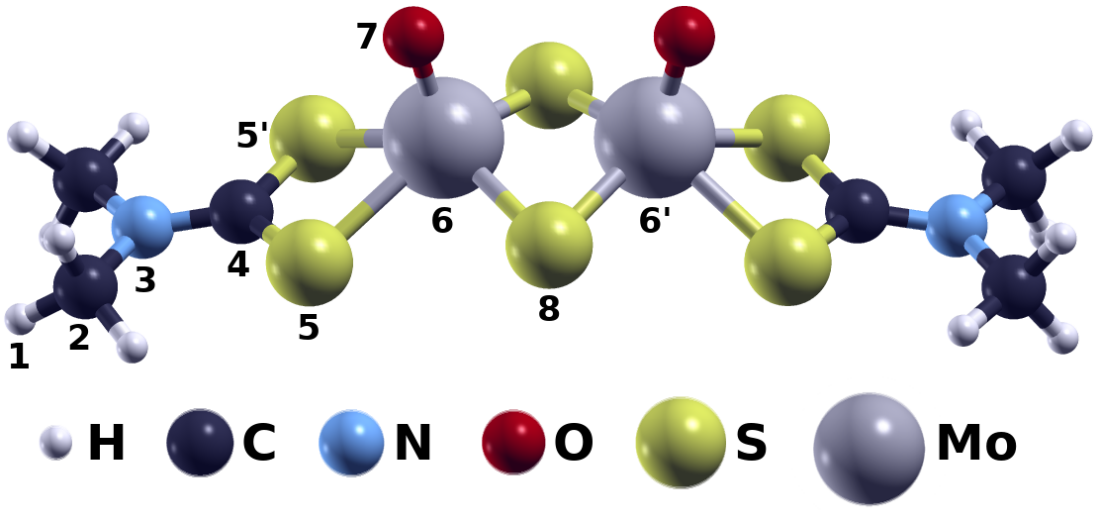


Figure 2.1: Chemical structure of the standard MoDTC complex.

the role of oxygen in the tribochemical decomposition of MoDTC, which is the first step in the formation of the MoS_2 tribolayer.

2.2 Methods

In commercially available formulations, MoDTC is commonly found in its dimeric form, although structures with one or three Mo atoms have also been described in literature [124]. In this work we only focus on the dimers and we consider the dimeric MoDTC complex, of C_{2v} symmetry, presented in Figure 2.1 as starting point of our investigation. The central unit of the complex is composed by two Mo atoms bridged by two S atoms. Each Mo atom is bound to an O atom by a double bond. We refer to the position of the O atoms in this complex as the terminal position, according to the notation employed by Khaemba *et al.* [102]. The coordination is completed by two bidentate dithiocarbamate (DTC) units, one for each Mo atom, providing a single bond to the metal as a whole. The DTC units were terminated with methyl groups, but longer alkyl chains were also considered to mimic those present in commercial lubricants [121, 123, 125, 126]. The oxidation number of each Mo atom in the complex is +5. In the following, we will refer to this structure as standard MoDTC (sMoDTC). All the eight isomers of the sMoDTC complex, obtained by exchanging the position of the two oxygen and six sulfur atoms, were also considered, along with twelve oxidized configurations and an oxygen-free complex.

The properties of all the MoDTC complexes were calculated by means of DFT, using the Perdew-Burke-Ernzerhof (PBE) [127] approximation to describe the exchange correlation functional. The calculations were in general performed using periodic supercells and the pseudopotential/plane-waves computational scheme implemented in the Quantum ESPRESSO package [128, 129]. As the next step of our investigation will require the simulation of extended systems to describe the interaction of MoDTC with metallic substrates, such computational scheme was chosen to ensure consistency of the results throughout the whole study. The plane-wave expansion of the electronic wave function (charge density) was truncated using a 40 Ry (320

Ry) cutoff for the kinetic energy, as the pseudopotential employed in this work were ultrasoft. The value of 40 Ry for the kinetic energy cutoff of the wave functions was chosen after a convergence test in which the energy difference between sMoDTC and one of its isomers is converged under a threshold of 2 meV, as explained in detail in Appendix A. A cubic super-cell with an edge of 60 bohr units was used to avoid interaction of the molecule with its periodic replicas. Integrations were carried out at the gamma point. The chemical structures were generated using the computer program Avogadro 1.2.0 [130, 131] and then optimized without any symmetry constraints. The process of geometry optimization was stopped when the total energy and the forces converged under thresholds of $1 \cdot 10^{-4}$ Ry and $1 \cdot 10^{-3}$ Ry/bohr, respectively.

Since the calculation of vibrational intensities is not possible for systems containing metallic atoms within Quantum ESPRESSO, the vibrational spectra were calculated by means of the density functional theory, employing the PBE approximation and the def2-TZVP basis set [132, 133], as implemented in the Gaussian 09 [134] computer program. No periodic boundary conditions were employed for these calculations. We performed an additional geometry optimization on the complexes before the frequency analysis and employed the Molekel 5.4 and GaussSum 3.0 software to analyze, post-process and plot the data [135, 136]. For the geometry optimization the average (root mean square) force converged under a threshold of $2 \cdot 10^{-5}$ Ry/bohr with an average displacement on the potential energy surface below $8 \cdot 10^{-5}$ Ry. An ultra-fine grid was chosen to carry out the integrations. No imaginary frequency was found in the analyses. For the calculation of the Raman spectra, a wave length of 785 nm was chosen for the incident photon. The simulated temperature of the spectra was 300 K and a full width at half maximum of 10 cm^{-1} was employed to broaden the peaks.

2.3 Results and discussion

2.3.1 The standard MoDTC complex

Despite the relevance of MoDTC in tribology, no structural data of this compound has ever been reported to the best of our knowledge. The bond lengths and angles of the optimized molecular structure shown in Figure 2.1 are reported in Table 2.1.

The angles between N and C atoms and the lengths of the N-C(4) bonds in MoDTC evidence a sp^2-like structure for the N atoms. The values are, in fact, compatible with a one-and-a-half N-C bond [137], consistent with an electronic delocalization involving N, C(4), S(5,5') and Mo atoms.

In order to test the validity of the calculated geometry of MoDTC, a comparison between experimental and calculated bond lengths and angles of two similar Mo-based dimeric complexes bridged by sulfur [138, 139] is included in Appendix A. Such comparison reveals that the bonds in the optimized structure are on average 1.4% longer than the experimental data, while bond angles range from -2.1 to 1.6% with respect to the experimental values.

Figure 2.2 shows the highest occupied molecular orbital (HOMO) and the lowest unoccupied molecular orbital (LUMO), respectively. Sulfur and molybdenum atoms mostly contribute to the formation of the HOMO. Considering the LUMO, we expect the Mo atoms to host additional electrons in case of reduction, due to the larger spatial extent of the probability density around these atoms. The energies of the HOMO and the LUMO are estimated to be -1.41 and 1.31 eV with respect to the Fermi level, providing an approximate HOMO-LUMO gap of 2.72 eV. This value for the HOMO-LUMO gap was confirmed by analyzing the density of states of sMoDTC, shown in Figure 2.3. Due to the lack of experimental UV/Vis spectra of MoDTC in literature, direct comparison of the calculated HOMO-LUMO gap with the experimental value is impossible. However, Mo atoms undergo reduction from +5, as in MoDTC, to +4, as

Table 2.1: Lengths and angles of selected bonds. The numbers in brackets follow the numbering proposed in Figure 2.1.

Bond	Length (Å)	Angle	Size (°)
H(1)-C(2)	1.10	C(2)-N(3)-C(2')	116
C(2)-N(3)	1.46	C(2)-N(3)-C(4)	122
N(3)-C(4)	1.34	N(3)-C(4)-S(5)	124
C(4)-S(5)	1.72	S(5)-C(4)-S(5')	113
S(5)-Mo(6)	2.49	C(4)-S(5)-Mo(6)	87
Mo(6)-O(7)	1.70	S(5)-Mo(6)-O(7)	104
Mo(6)-S(8)	2.34	Mo(6)-S(8)-Mo(6')	74
Mo(6)-Mo(6')	2.82	O(7)-Mo(6)-Mo(6')	103

in MoS_2, during the tribochemical reaction. Therefore, an estimation of the HOMO-LUMO gap is still useful to better characterize the molecule and its electronic properties.

2.3.2 Fragmentation of sMoDTC

The first step of the tribochemical process leading to MoS_2 is molecular fragmentation. In tribological conditions, the fragments are stabilized by the presence of the metallic surface. Calculating the fragmentation energy of isolated MoDTC complexes is nevertheless useful to characterize, at least qualitatively, the strength of molecular bonds independently on the nature of the substrate and to identify the effects of oxidation on molecular stability and the dissociation paths.

We refer to the homolytic breaking of the S-Mo bonds (5,5'-6) proposed by Grossiord *et al.*, as *Cut 1*. The fragmentation pattern proposed by Khaemba *et al.*, with the break of the C-S bonds (4-5,5'), is referred as *Cut 3* in the following. *Cut 2* is the intermediate pattern we considered, for sake of comparison, where one C-S bond (4-5) and one S-Mo bond (5'-6) are broken. A schematic representation of the three dissociation patterns is shown in Figure 2.4. In order to verify which is the most favourable dissociation pattern of isolated sMoDTC, we evaluated the energy difference between the complex and its fragments in the following way:

$$\Delta E_{\text{frag}} = E_{\text{sMoDTC}} - E_{\text{frag1}} - E_{\text{frag2}} \tag{2.1}$$

where E_{sMoDTC} is the total energy of sMoDTC, E_{frag1} and E_{frag2} are the total energies of the two complementary fragments resulting from the three possible dissociation patterns, namely *Cut 1*, *Cut 2* and *Cut 3*. When calculating the total energies of the fragments, their geometry was kept constant to avoid rearrangements that could influence the resulting energy values. No additional atoms were attached to the atoms with a broken bond. Therefore, spin-polarization for the electrons was taken into account in order not to restrict the possible electronic configuration to a closed-shell. Table 2.2 reports the calculated total and absolute magnetization of the fragments at the end of the self-consistent cycle. These two quantities correspond to the integral of the magnetization and the integral of the absolute value of the magnetization in the cell, respectively. Therefore, they can be associated to the number of unpaired electrons in the system: while for the fragments on the left of Figure 2.4 the number of unpaired electrons is close to one for each *Cut*, meaning that the spin multiplicity of the electronic state is approximately a doublet, for the fragments on the right this is true only for *Cuts 1* and *2*. For *Cut 3* the description of the electronic state is

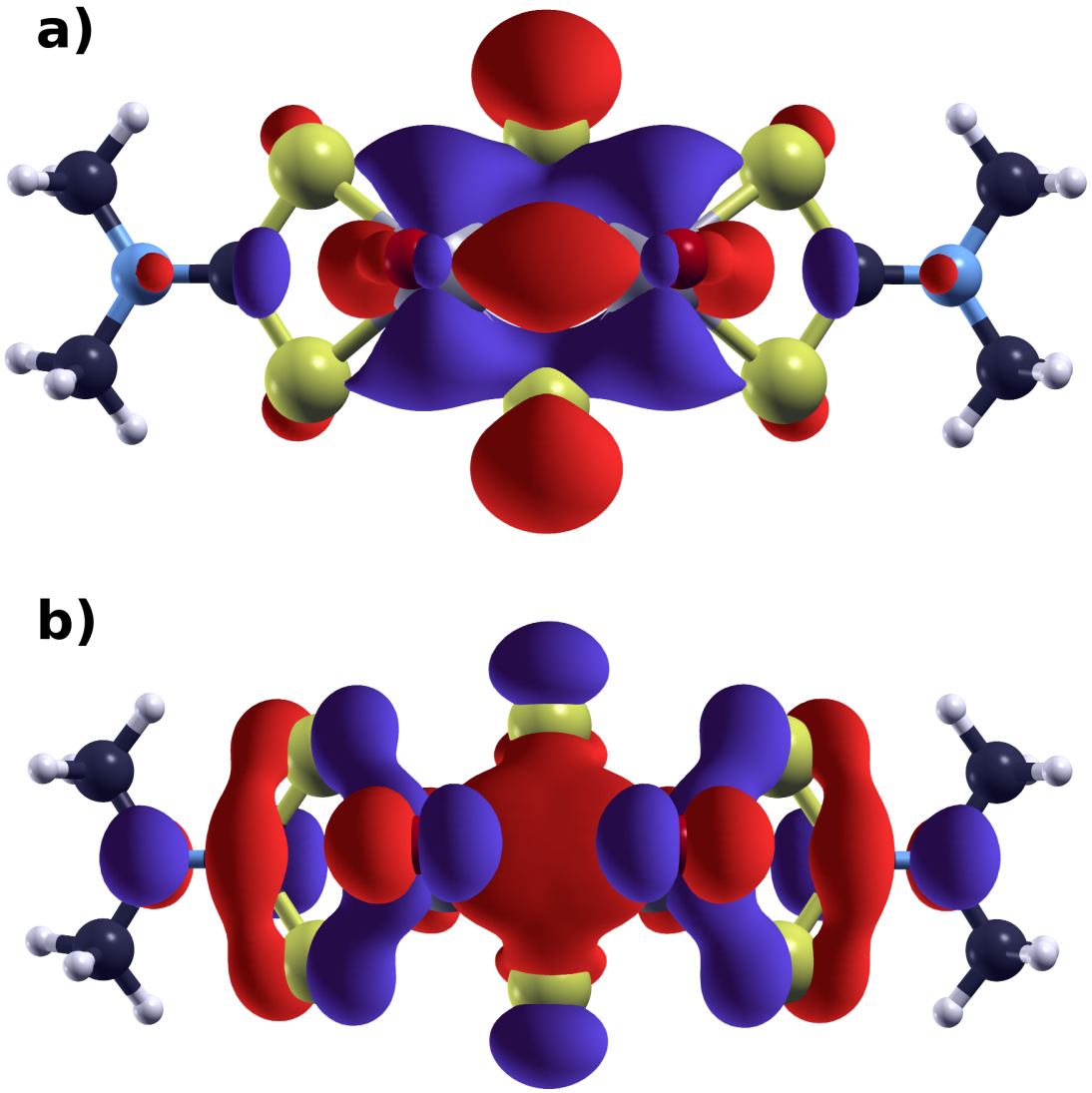


Figure 2.2: Top views of a) HOMO and b) LUMO of sMoDTC. Blue and red colors of the isosurfaces correspond to the positive and negative sign of the wave function, respectively.

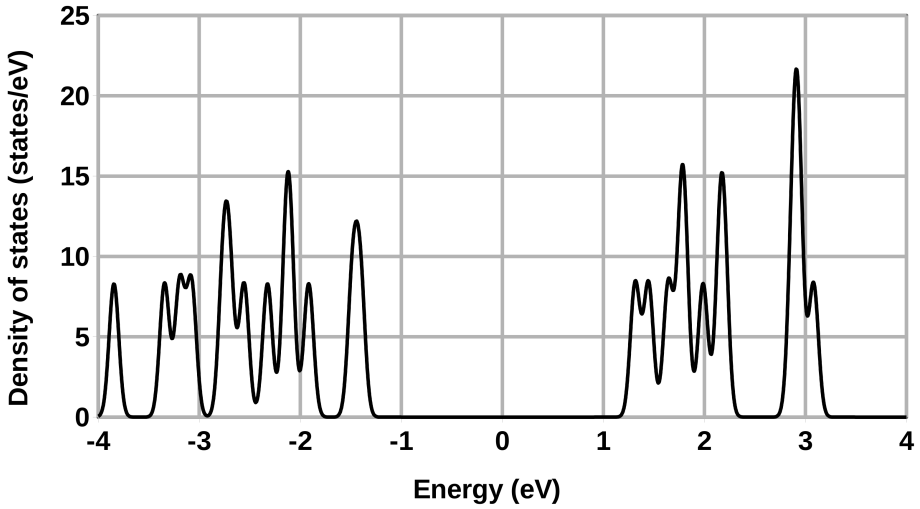


Figure 2.3: Density of states of sMoDTC.

more complex, as it may result in a combination of different electronic structures. Non-integer values of the absolute magnetization may indicate a spin contamination of the electronic structures of these fragments.

The energy differences calculated with this approach are: -4.12, -4.61 and -6.72 eV for *Cut 1*, *Cut 2* and *Cut 3*, respectively, indicating that the first cut is the most favourable for isolated sMoDTC, as less energy is required to separate the two fragments of the complex from each other. This result is in agreement with the mechanism proposed by Grossiord and other authors [101, 123, 140, 141]. Although the calculated fragmentation energies clearly indicate that the most favourable fragmentation path is *Cut 1* for the isolated compound, we expect that a metallic surface may provide a stabilization which can be different for the different fragments, thus modifying the picture provided by this calculation.

Table 2.2: Total and absolute magnetization, expressed in Bohr magnetons per cell, of the fragments of sMoDTC depicted in Figure 2.4.

	Total magnetization		Absolute magnetization	
	Left fragment	Right fragment	Left fragment	Right fragment
Cut 1	0.99	1.00	1.11	1.10
Cut 2	1.00	0.99	1.11	1.15
Cut 3	1.00	0.65	1.15	1.42

2.3.3 Isomers and oxidized molecules

In order to understand which is the most favourable position of the oxygen atoms in the MoDTC complex, we calculated the total energy of all the possible isomers of sMoDTC where the positions of O and S atoms are exchanged, as represented in Figure 2.5.

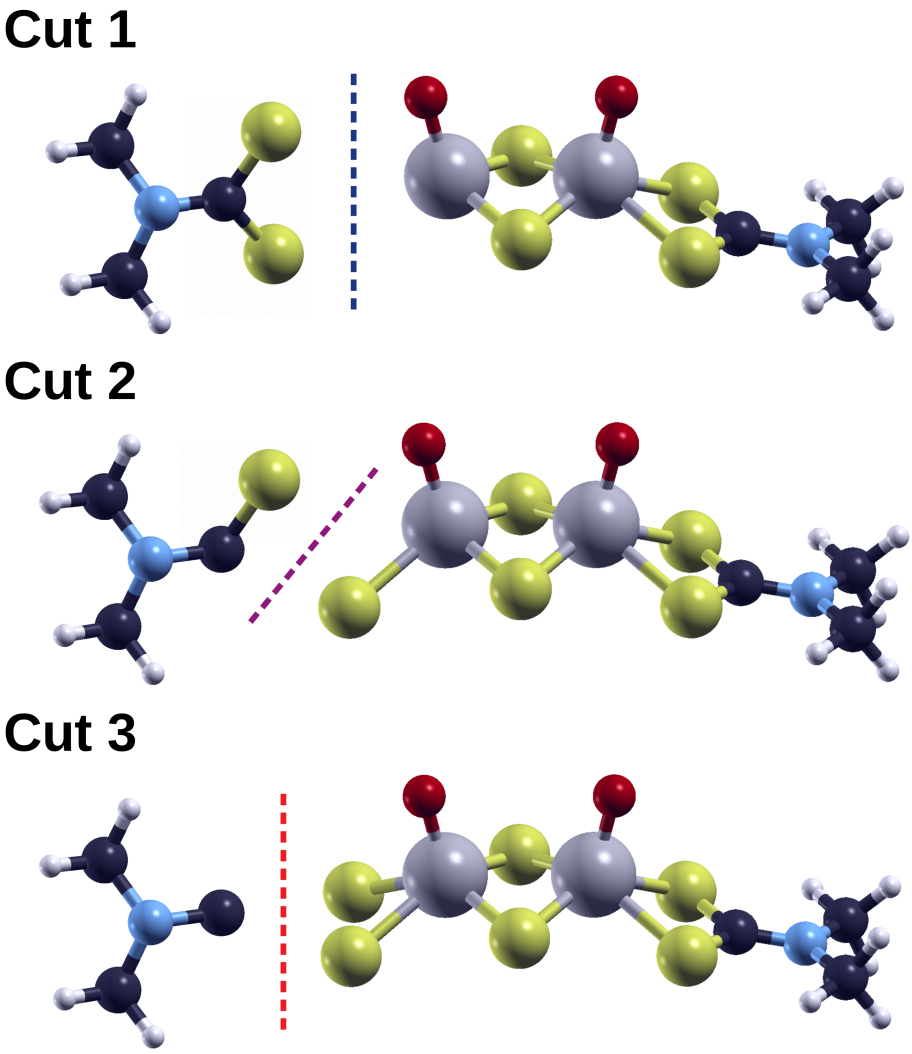


Figure 2.4: Schematic representation of the three dissociation patterns of MoDTC considered in this work.

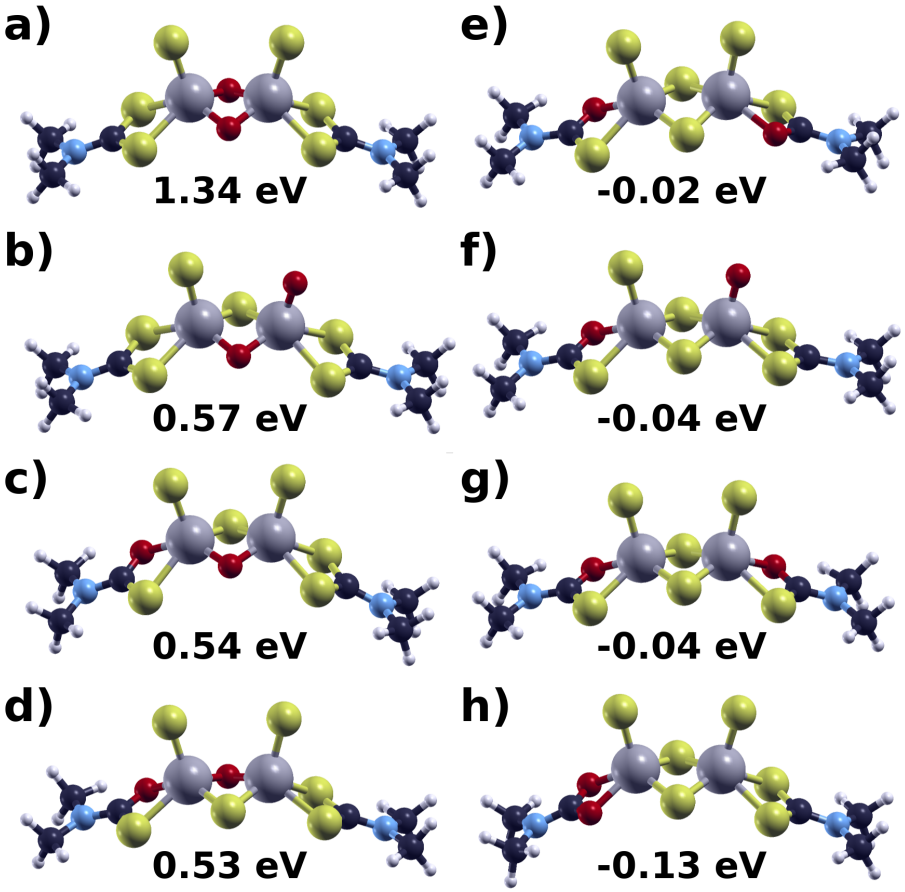


Figure 2.5: Chemical structures of the eight isomers studied in this work. For each isomer, the total energy difference from sMoDTC is reported in eV. Negative values correspond to structures that are more stable than sMoDTC.

For each isomer in Figure 2.5, the total energy difference with respect to sMoDTC is also reported. From these differences it emerges that the bridging position between the Mo atoms is unfavourable for O atoms, most likely because of their strained geometry (panels a-d). The Mo(6)-S(8)-Mo(6') angle is, in fact, equal to 74°, which is a small angle for O atoms and could cause strong repulsion between the two electron pairs shared with Mo atoms. The most favourable position for O atoms in MoDTC is the ligand position, between the C atom of the carbamate unit and a Mo atom (panels e-h). The stabilization effect of the external O atom is increased when two of these atoms are on the same carbamate unit (h). Despite the high stabilization provided by the two O atoms in ligand position on the same carbamate unit, the probability for Isomer *h* to be present in high concentration in real samples depends on the probability for the oxygen atom in terminal position to replace a sulfur atom in δ position, which may require multiple-step reactions of high energy barriers. Nevertheless, the choice of the computational parameters can influence the ordering in terms of total energy of the chemical structures, as shown by a comparison between the results obtained with Quantum ESPRESSO and Gaussian in Appendix A. Some discrepancies can be observed by comparing the energy ordering of the structures obtained with the different codes. Still, the overall picture does not change dramatically, as the ligand position in MoDTC is confirmed from experimental evidence to be the destination of additional oxygen atoms coming from the environment [123]. In Appendix A it is shown that the source of the discrepancies can be found in a strong interaction between the S(5)-S(5') bond and the adjacent N(3)-C(4) bond by employing the PBE functional in Gaussian. The B3LYP functional in Gaussian [142–145] provides an energy ordering in agreement with the one proposed by Quantum ESPRESSO, while being less accurate than PBE for the simulation of the vibrational spectra.

We also studied the oxidation of MoDTC by investigating twelve complexes resulting from the substitution of one or two S atoms with O atoms. The chemical structures of the considered complexes resulting from the S-O substitutions are represented in Figure 2.6. Since it is not possible to compare directly the total energies of molecular structures with different atoms, we calculated the reaction energy of a virtual substitution process mediated by an iron surface:

$$\mathrm{sMoDTC} + x\,\mathrm{O_{ads}} \rightarrow \mathrm{Mo_2S_{6-x}O_{2+x}DTC} + x\,\mathrm{S_{ads}} \tag{2.2}$$

where sMoDTC is the structure presented in Figure 2.1, $\mathrm{Mo_2S_{6-x}O_{2+x}DTC}$ is the complex with $x = 1, 2$ additional oxygen atoms obtained from substitution, O_{ads} and S_{ads} are individual O and S atoms adsorbed on Fe(110), which is the most stable iron surface. We will refer to the generic complex $\mathrm{Mo_2S_{6-x}O_{2+x}DTC}$ as MoDTC* in the following equations. The reaction energy of the substitution in Equation 2.2 is:

$$\Delta E = E_{\mathrm{MoDTC^*}} - E_{\mathrm{sMoDTC}} + E_{\mathrm{S}} - E_{\mathrm{O}} + E_{\mathrm{ads,S}} - E_{\mathrm{ads,O}} \tag{2.3}$$

where $E_{\mathrm{MoDTC^*}}$ and E_{sMoDTC} are the total energies of MoDTC* and sMoDTC, E_{S} and E_{O} are the total energies of isolated S and O atoms, and $E_{\mathrm{ads,S}} = 6.33$ eV and $E_{\mathrm{ads,O}} = 6.44$ eV are the adsorption energies of S and O in the fourfold sites of the (110) iron surface, which are the most stable adsorption sites for both the elements [146]. It is worth to note that, in tribological conditions, different surfaces of iron can be exposed and defects can be formed on the surfaces. However, for the purpose of this study, only the (110) iron surface is considered, because it is the most frequently occurring among all the iron surfaces, being the most stable one. Also, the other surfaces and defects are expected to influence the values of $E_{\mathrm{ads,S}}$ and $E_{\mathrm{ads,O}}$ in a similar way. Therefore, the ordering of the substituted compounds in terms of relative stability with respect to sMoDTC is not expected to change substantially by considering other iron surfaces. The reaction energies obtained from Equation 2.3 are reported in Figure 2.6 below each complex. The comparison between the results obtained with Quantum ESPRESSO and Gaussian is included in Appendix A also for the substituted complexes.

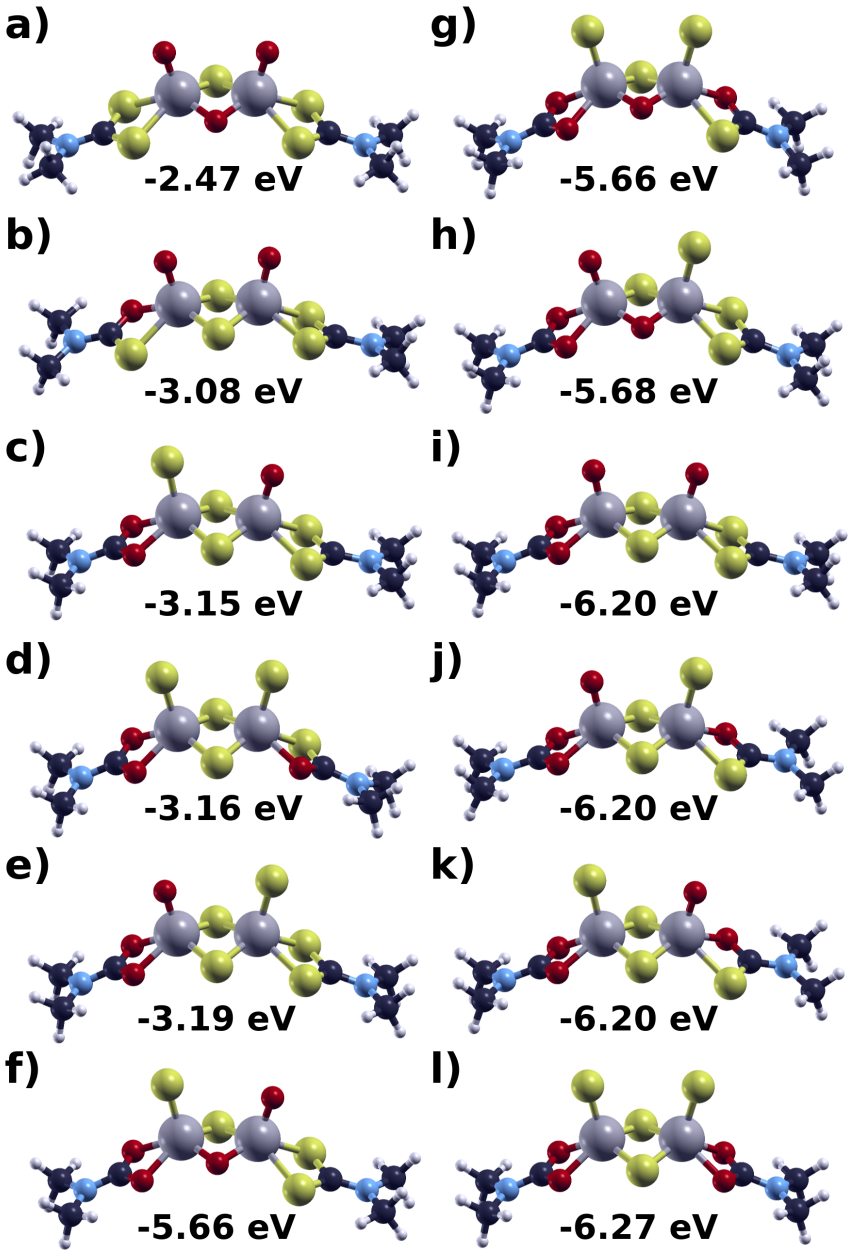


Figure 2.6: Chemical structures of the oxidized MoDTC complexes studied in this work. Panels a-e (f-l) represent isomers containing three (four) O atoms. For each structure, the substitution reaction energy is reported as calculated in Equation 2.3.

We have calculated the total energy, after geometry optimization, of an oxygen-free complex with a molecular structure similar to sMoDTC where the two O atoms are replaced by S atoms. This oxygen-free complex (OfMoDTC) is less stable than sMoDTC of about 6.01 eV. This result is consistent with the reaction energies presented in Figure 2.6, where a single replacement of an S atom by an O atom is shown to stabilize the molecular structure by 3 eV.

The energy gain ΔE calculated in Equation 2.3, however, implies that the S substitution by O is mediated by iron. In order to verify that the oxidation process of sMoDTC is favoured also in other cases, we built the stability diagram showed in Figure 2.7, where the chemical potential of sulfur, μ_S, is allowed to vary within a range defined from the chemical potential of an S atom adsorbed on iron to the chemical potential of an isolated S atom in vacuum. The chemical potential of oxygen, μ_O, is considered equal to half of the total energy of an O_2 molecule, assuming that residual O atoms recombine in molecular oxygen. The considered oxidation reactions are:

$$\text{sMoDTC} + \text{O}_2 \rightarrow \text{Substitution } b + \text{O} + \text{S} \tag{2.4}$$

$$\text{sMoDTC} + \text{O}_2 \rightarrow \text{Substitution } i + 2\text{S}. \tag{2.5}$$

Substitution b and i in Equations 2.4 and 2.5 refer to the corresponding complexes in Figure 2.6, which originate upon substitution of one or two S atoms by O atoms in sMoDTC. These two complexes turned out to be the most stable configurations for a single (b) and double (i) replacement of S atoms with O atoms on iron. The energies corresponding to these reactions are:

$$\Delta E = E_{\text{Sub}\,b} + \mu_{\text{S}} + \mu_{\text{O}} - E_{\text{sMoDTC}} - E_{\text{O}_2} \tag{2.6}$$

$$\Delta E = E_{\text{Sub}\,i} + 2\mu_{\text{S}} - E_{\text{sMoDTC}} - E_{\text{O}_2} \tag{2.7}$$

where E_{sMoDTC}, $E_{\text{Sub}\,b}$, $E_{\text{Sub}\,i}$ and E_{O_2} are the total energies of the corresponding chemical species after geometry optimization. By varying μ_S it is possible to compare the stability of sMoDTC, Substitution b and Substitution i by considering different destinations for the S atoms involved in the oxidation reaction. The study of the stability of a system as a function of the chemical potential of reactants or products is a commonly employed approach in surface physics to compare the adsorption energy of different species [147–149]. To the best of our knowledge, it is used in the present work for the first time to study the stability of different chemical structures that undergo oxidation. We consider the total energy of S as the chemical potential, since calculations at the level of theory employed in this work do not take into account temperature, hence the molar Gibbs free energy is equivalent to the molar internal energy. Oxidation is favoured for the most part of the considered range as the reaction energies are negative. In particular, Substitution i is more stable than Substitution b in a wide range of chemical potentials, including the chemical potential of S in MoS_2 (purple dashed line). The chemical potential of S in MoS_2 is approximated as:

$$\mu_S(MoS_2) = E_{MoS_2} - E_{vMoS_2} \tag{2.8}$$

where E_{MoS_2} is the total energy of a 5x4 supercell containing a single monolayer of MoS_2 (120 atoms in total), while E_{vMoS_2} is a similar supercell with a single vacancy of a sulfur atom in the MoS_2 monolayer. The dimensions of the supercell ($22.1 \times 15.9 \times 35.0$ Å^3) were tested to ensure sufficient isolation of the vacancy of the sulfur atom.

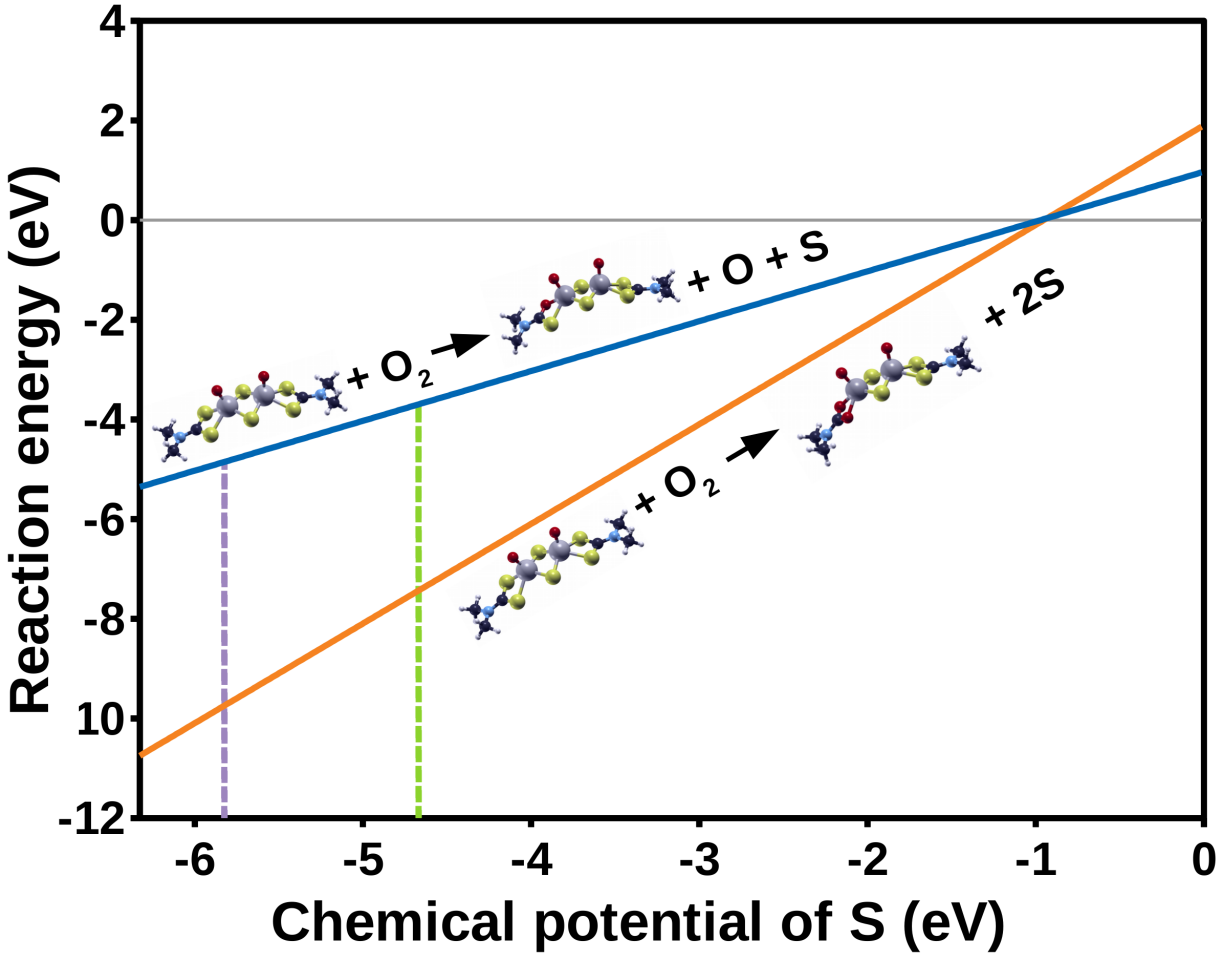


Figure 2.7: Stability diagram for the oxidation reactions. The blue and orange solid lines correspond to the single and the double oxidation reactions, respectively. The left and right limits of the diagram correspond to the chemical potentials of an S atom adsorbed on iron and of an isolated S atom in vacuum, respectively. The purple and green dashed vertical lines identify the chemical potential of S in MoS_2 and in S_8, respectively.

Table 2.3: Partial charges on Mo atoms. As calculated in Equation 2.9, the charges are obtained by comparison with the values of sMoDTC reported in the text. The structures in the table are represented in Figures 2.5 and 2.6.

Structure	Partial charges (e)	
	Mo 1	Mo 2
Substitution j	-0.21	0.19
Substitution e	-0.21	0.29
Substitution a	-0.16	-0.16
Substitution f	-0.11	-0.13
Isomer a	-0.03	-0.04
Substitution l	0.08	0.08
Substitution d	0.08	0.19
Isomer h	0.09	0.29
Isomer f	0.18	0.01

2.3.4 Partial charges on Mo atoms

It has been reported in the past that dinuclear Mo complexes bridged by S atoms can easily undergo reduction [150]. The same may apply to MoDTC complexes in tribological conditions, in which the molybdenum atoms could reach the oxidation number of +4, as in MoS_2, from the oxidation number of +5 [30]. This reduction of molybdenum atoms from +5 to +4 may aid the dissociation process by lowering the corresponding energy barrier. Therefore, it can be useful to verify whether the oxidation state of the molybdenum atoms in some of the structures presented here is similar to the oxidation state of Mo in MoS_2. A way to computationally estimate the oxidation states is based on charge analysis. We calculated partial charges $\Delta\rho$ on the Mo atoms of a selected group of complexes by performing the Bader charge analysis, as implemented in a computer program by the group of Henkelman [151–154]. The resulting absolute charge ρ of both Mo atoms in sMoDTC is -12.32 e, where e is the absolute value of the electronic charge. In Table 2.3 we report the calculated partial charge for the two Mo atoms in nine different MoDTC complexes considering the Mo partial charge in sMoDTC as reference:

$$\Delta\rho = \rho_{\text{Complex}} - \rho_{\text{sMoDTC}} \tag{2.9}$$

The trend of the partial charges can be explained by considering the electronegativity of the Mo-neighbouring atoms in these structures. In general, additional O atoms induce a slight charge depletion on the neighbouring Mo atom and a slight charge accumulation on the other Mo atom in the molecule. We can approximate to +5 the oxidation number of the Mo atoms in sMoDTC and perform a proportion on the partial charges to find the oxidation number of the Mo atoms in the other structures. By following this strategy, a reduction can be only assigned to the second Mo atom of Substitution e and Isomer h, since their oxidation numbers are around +4. As shown in Appendix A, the Löwdin approach implemented in Quantum ESPRESSO does not provide reliable values of absolute charges but only of their trends. A subsequent step of the investigation, not discussed in this work, is the simulation of the dissociation of such structures in tribological conditions. Therefore, the analysis presented in this section can be viewed as an initial step towards a stronger connection between the electronic and the tribological properties of MoDTC.

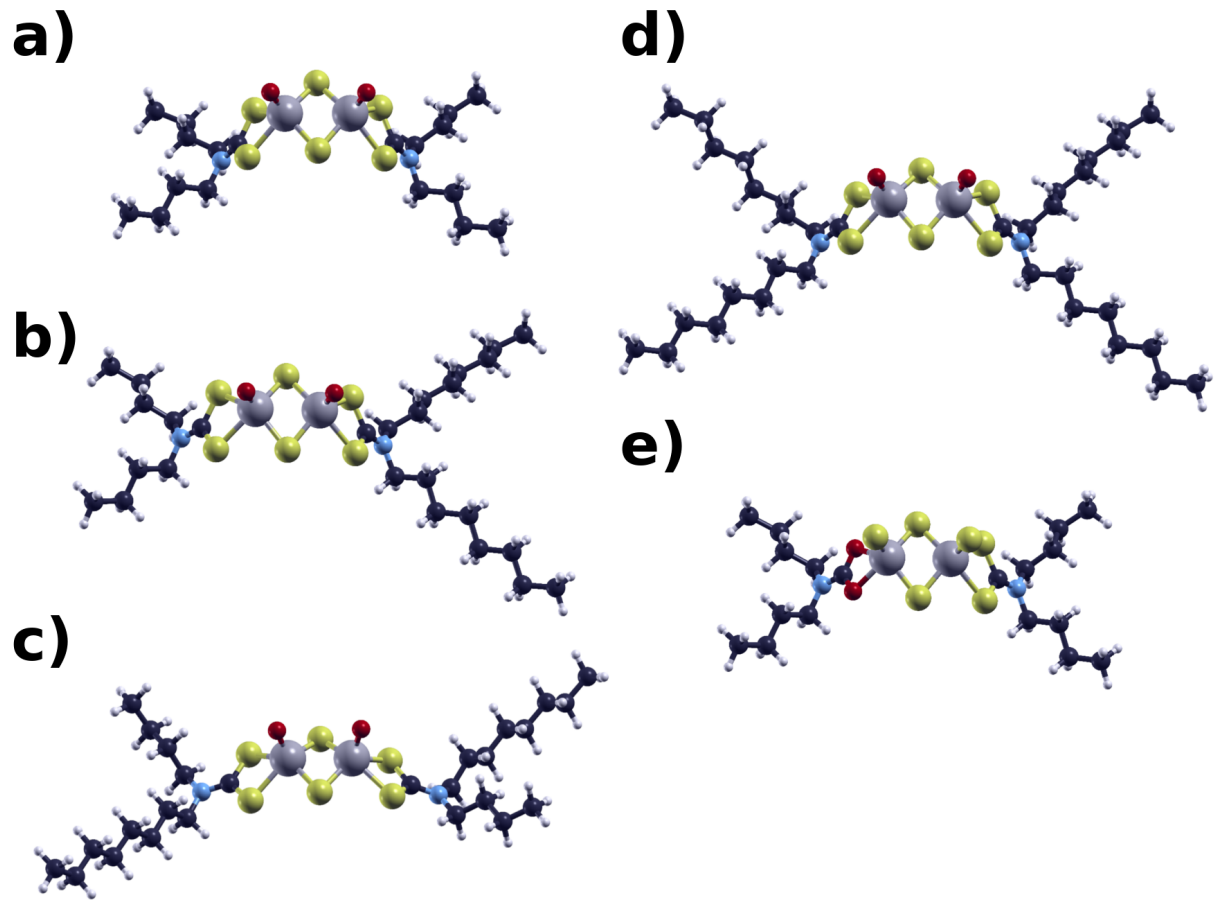


Figure 2.8: Chemical structures of the five MoDTC complexes with longer alkyl chains in the carbamate units.

2.3.5 Role of the carbon chain

Longer carbon chains are usually present in the commercially available complexes. In order to understand whether MoDTC terminating with methyl groups are a good approximation of the commercial compounds, we considered five more MoDTC complexes with *n*-butyl and *n*-octyl lateral chains. The chemical structure of these complexes is shown in Figure 2.8.

Complexes *a*-*d* are based on sMoDTC, while Complex *e* is based on Isomer *h*. Complexes *a* and *e* present four equivalent *n*-butyl chains in their carbamate units. Complex *d* presents four equivalent *n*-octyl chains. Both Complexes *b* and *c* present two *n*-butyl and two *n*-octyl chains. In Complex *b* the chains of the same lengths are on the same carbamate unit, while in Complex *c* both carbamate units contain chains of different lengths. The fragment analysis of Complexes *a*, *b*, *d* and *e* confirms that the most favourable cut is *Cut 1*, as in the case of sMoDTC. The fragment analysis was carried out in the same way as explained previously. The dissociation energy of Complex *a* is the lowest among the considered complexes, as it is

3.99 eV, compared with 4.08, 4.15, 4.05 and 4.64 eV for Complexes b on the butyl side, b on the octyl side, d and e, respectively. All these dissociation energies are comparable and generally lower than the dissociation energy of sMoDTC, indicating that the longer alkyl chains in the carbamate unit stabilize the fragments and facilitate the dissociation. This is especially true for Complex e, where the two oxygen atoms occupy the ligand position. The energy difference between Complex e and Complex a is -0.337 eV, while the energy difference between the corresponding structures with methyl groups, Isomer h and sMoDTC, is -0.133 eV. The stabilization due to the oxygen atoms in ligand position is higher in complexes with longer alkyl chains. As in the previous cases, we expect the fragments generated by the dissociation of these complexes to be heavily stabilized by the presence of the metallic surface.

After molecular dissociation, longer alkyl chains can be dissolved in the lubricant oil and, in case they are radicals, may react with other chemical species, possibly influencing the tribochemical transformation of other MoDTC molecules.

2.3.6 Simulation of vibrational spectra

Vibrational spectroscopy is a technique commonly employed to detect lubricant additives in real samples and to follow tribochemical reactions *in-* and *ex-situ*. MoDTC is generally a mixture of different compounds with variable S/O ratio in real samples. Identifying diagnostic features in the vibrational spectra of individual isolated compounds could help the characterization of the chemical species active in the tribological processes. Therefore, we complete our investigation on isolated MoDTC complexes by presenting simulated vibrational spectra of MoDTC.

Simulated IR and Raman spectra of sMoDTC are compared with experimental data provided by Total Marketing and Services and from Khaemba *et al.* in Figure 2.9(a). The peak assignment of the spectra of sMoDTC is presented in Table 2.4 and is in general agreement with the experimental observations [102, 138, 139]. The vibration of carbon and hydrogen atoms in the methyl groups of sMoDTC correspond to the peaks around 3000 cm^{-1} in both the IR and Raman spectra. This is a constant feature in the spectra of all the structures we considered. The region between 500 and 1600 cm^{-1} is mainly populated by peaks relative to vibrations in the carbamate units, while peaks below 500 cm^{-1} are mostly relative to the central metallic unit. The simulations overestimate the frequency of the peaks around 3000 cm^{-1} and are not able to fully describe some features around 1300 cm^{-1} and 700 cm^{-1}. On the contrary, the Mo-O peak at around 1000 cm^{-1} and especially the C-N peak at around 1500 cm^{-1} are well described. While the simulated system contains an isolated complex, the real samples most probably contain a mixture of different structures. We believe the contribution of the different structures and their mutual interaction in the real sample to be the cause of the discrepancies in the intensity and, to some extent, in the frequency of the peaks. Also, MoDTC is often found commercially in a mixture with base oil. Therefore, we studied with Quantum ESPRESSO the interaction of sMoDTC with 1-hexene, as a simple approximation of a non-polar solvent, and the effect of 1-hexene on the vibrational spectra of sMoDTC with the polarizable continuum model (PCM) implemented in Gaussian 09 [155, 156]. This study is presented in the following Section.

The simulated spectra of the different complexes considered in this work present many similarities among each other. The comparison of the IR spectra of sMoDTC and Isomer h is presented in Figure 2.9(b), while the comparison of the Raman spectra of these two complexes is presented in Figure 2.9(c). The comparison is shown in the range of 200-1600 cm^{-1}, since the peaks around 3000 cm^{-1} appear to be almost identical for the two complexes. The main feature emerging from the spectra of Isomer h is the splitting of several peaks, due to the broken symmetry of the chemical structure. Generally, vibrations involving atoms on the carbamate unit with oxygen atoms are found at higher frequencies than the same vibrations in carbamate units with sulfur atoms, in agreement with the decrease of the reduced mass when exchanging

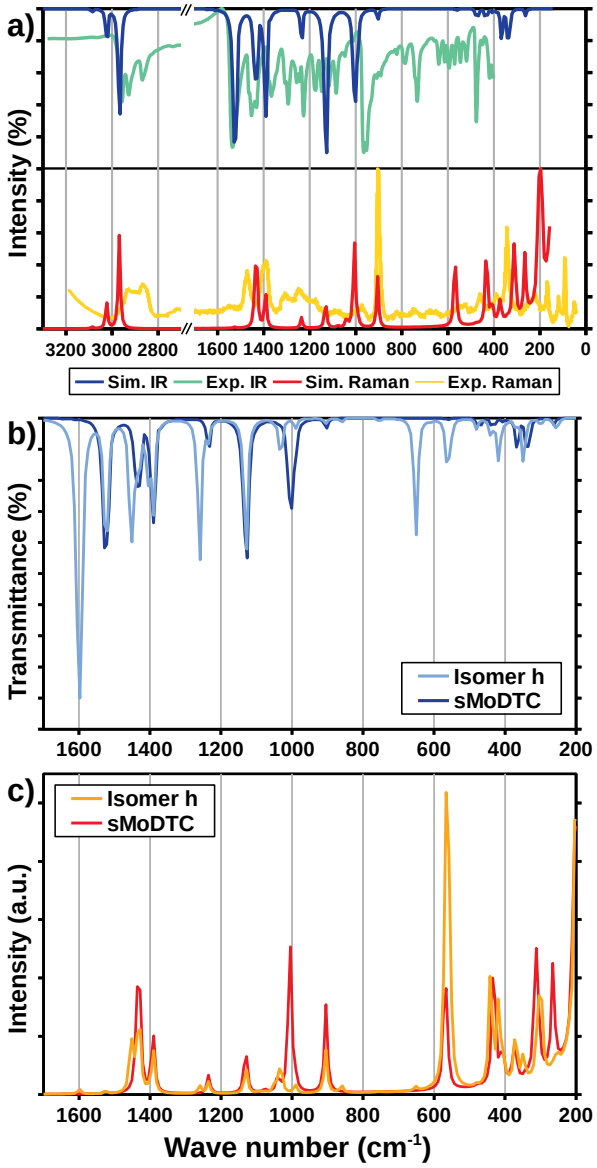


Figure 2.9: Vibrational spectra of MoDTC complexes: a) Simulated IR (blue) and Raman (red) spectra of sMoDTC, experimental IR (turquoise) and Raman (yellow) spectra of MoDTC. The y axis reports the percentage of transmittance (absorbance) for the IR (Raman) spectra. The details concerning the experimental IR spectrum are included in Appendix A, while the experimental Raman spectrum is reproduced from Ref. [102]. b) IR spectra of sMoDTC and Isomer *h*. c) Raman spectra of sMoDTC and Isomer *h*. No horizontal shift was performed on the spectra.

Table 2.4: Peak assignment of the spectra presented in Figure 2.9(a), in decreasing order of wave number (expressed in cm^{-1}). The symbols ν, δ, ρ, ω, τ indicate stretching, bending, rocking, wagging and twisting, respectively. Subscripts *brg* and *lig* indicate bridging and ligand positions.

Wave number	Vibration	Wave number	Vibration
3084	ν C-H	562	ν C-S, δ C-N
3021	ν C-H	469	ν Mo-S_{brg}
2966	ν C-H	424	ν Mo-S_{brg}
1520	ν N-C, δ H-C-H	401	δ S-Mo-S
1427	ν N-C, δ H-C-H	332	ν Mo-S_{lig}
1387	ω CH_3, ν N-C	307	ν Mo-Mo
1230	ν C-N	300	ν C-S, ν Mo-S_{lig}
1126	ν C-N, ν C-S	259	ω N-C
1125	ν C-N, ν C-S	257	δ S_{brg}-Mo-O
1123	ν C-N, ν C-S	255	δ S_{lig}-Mo-O
1071	τ C-N, δ H-C-H	200	δ S_{lig}-Mo-O
1034	ν C-N, ν C-S	194	δ S_{lig}-Mo-O
1000	ν Mo-O	184	δ S_{lig}-Mo-S_{brg}
987	ν C-S, δ C-N-C	130	δ Mo-Mo-S_{lig}
898	ν C-S, ν C-N	123	ν Mo-Mo

sulfur with oxygen.

By considering the differences between the vibrational spectra of sMoDTC and Isomer *h*, it is possible to distinguish these two structures. However, the comparison with experiments is not always easy since in oil mixtures many MoDTC structures can be present at the same time and the interaction of several molecules among each other and the presence of a metallic surface may influence the vibrational modes. Qualitative differences among the simulated spectra can still be noticed and it is reasonable to expect such differences also in the spectra of pure compounds in the gas phase.

2.3.7 Effect of the solvent on the molecular structure

A wide variety of oils can be used to solubilize MoDTC, depending on their physico-chemical properties and their formulations. In this section, we estimate the role of solvent on MoDTC by considering 1-hexene as a simple approximation for a non-polar solvent. Firstly, we performed different calculations with QE to investigate the interaction of 1-hexene and sMoDTC by varying their relative distance. Secondly, we simulated the vibrational spectra of sMoDTC by employing the polarizable continuum model (PCM) [155, 156] implemented in Gaussian 09 to simulate the effect of 1-hexene. A comparison between simulated spectra with and without employing the PCM is included at the end of this section.

Interaction of sMoDTC with 1-hexene

We calculated the interaction energy between two molecules of 1-hexene and sMoDTC in the following way:

$$E_{int} = E_{tot} - E_{sMoDTC} - E_{2C_6H_{12}} \tag{2.10}$$

where E_{tot}, E_{sMoDTC} and $E_{2C_6H_{12}}$ are the total energies of the system composed by sMoDTC and the two hexene molecules, of sMoDTC alone and of the two hexenes molecules alone, respectively. We calculated such interaction energies for three different configurations, where sMoDTC was in the center of a cell whose x edge was occupied by two equally-spaced 1-hexene molecules. While the x dimension was kept at 40 bohr for all the considered systems, both y and z dimensions were 40, 30 and 20 bohr for Systems 1, 2 and 3, respectively. For these calculations, Grimme's DF3 correction was taken into account to better describe the long-range interactions [157], as implemented in QE. The three systems are shown in Figure 2.10.

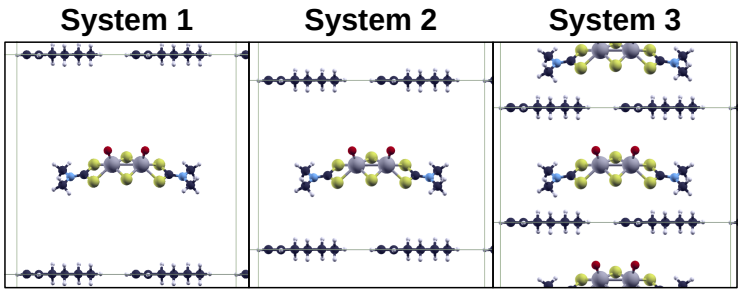


Figure 2.10: XZ view of the three systems.

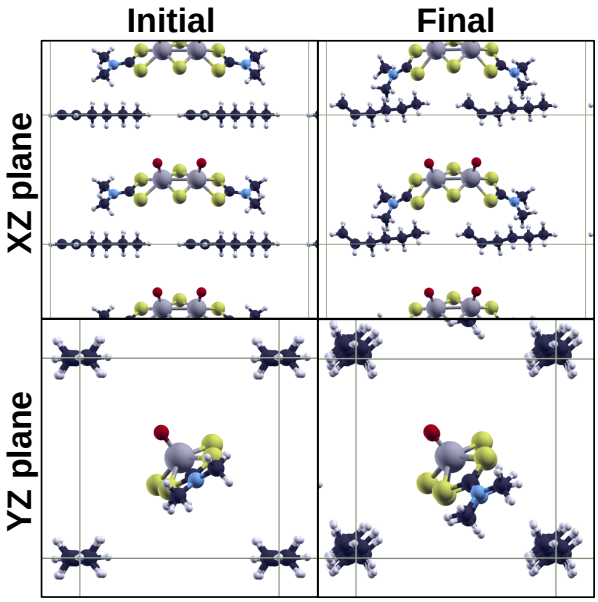


Figure 2.11: XZ (top) and YZ (bottom) views of System 3 before (left) and after (right) the geometry optimization.

The interaction energies turned out to be -3.1, -16.4 and -208.1 meV in Systems 1, 2 and 3 respectively. The only significant interaction energy is in the case of System 3, as demonstrated by performing a geometry

Table 2.5: Comparison of lengths and angles of selected bonds of sMoDTC calculated with Quantum ESPRESSO. The numbers in brackets follow the numbering proposed in Figure 1 of the main text. The values of l_0, l_1, l_2 and l_3 correspond to the bond lengths, expressed in Å, in the isolated case and in Systems 1, 2 and 3, respectively, while α_0, α_1, α_2 and α_3 are the bond angles, expressed in °, in the corresponding systems.

Bond	l_0	l_1	l_2	l_3
H(1)-C(2)	1.099	1.100	1.100	1.100
C(2)-N(3)	1.458	1.457	1.457	1.461
N(3)-C(4)	1.338	1.338	1.338	1.337
C(4)-S(5)	1.723	1.723	1.723	1.716
S(5)-Mo(6)	2.493	2.489	2.488	2.516
Mo(6)-O(7)	1.702	1.702	1.703	1.705
Mo(6)-S(8)	2.337	2.337	2.338	2.329
Mo(6)-Mo(6')	2.818	2.809	2.813	2.841
Angle	α_0	α_1	α_2	α_3
C(2)-N(3)-C(2')	116.2	116.2	116.3	117.3
C(2)-N(3)-C(4)	122.4	122.4	122.4	120.2
N(3)-C(4)-S(5)	124.0	124.0	124.0	122.5
S(5)-C(4)-S(5')	112.9	113.0	113.0	113.3
C(4)-S(5)-Mo(6)	87.2	87.0	87.0	87.9
S(5)-Mo(6)-O(7)	104.4	104.8	104.4	103.5
Mo(6)-S(8)-Mo(6')	74.2	73.9	74.0	75.1
O(7)-Mo(6)-Mo(6')	103.4	103.4	104.2	107.5

optimization of the three systems. While no relevant change in the geometry occurs for Systems 1 and 2 (not shown), System 3 undergoes a modification in the atomic positions after the optimization, as shown in Figure 2.11.

The interaction between the methyl groups of sMoDTC and the hexene molecules is attractive, causing the complex to bend towards the alkenes and vice versa. Table 2.5 contains selected bond lengths and angles of sMoDTC after geometry optimization in the isolated case and in the three systems presented in this section. While the optimized geometry of sMoDTC in Systems 1 and 2 does not differ significantly from the one of the isolated molecule, some structural modifications can be observed for the complex in System 3, especially for the central unit (Mo-Mo, Mo-S) and its proximity (C-S).

Effect of the solvent on the spectra

In order to verify whether a non-polar solvent can modify the vibrational spectra of sMoDTC, we optimized the geometry of sMoDTC employing the PCM implemented in Gaussian 09 and compared its structural data as well as its spectra to the results obtained without considering the solvent. For the PCM calculations, 1-hexene was chosen as the solvent. Table 2.6 summarizes the comparison concerning the structural data of sMoDTC, as previously done for QE. The differences in bond lengths and angles are smaller compared to the ones seen with QE involving isolated sMoDTC and System 3.

In Figure 2.12, the comparison between vibrational spectra obtained with and without considering the

solvent is shown. While mostly the intensity of the peaks is affected by the presence of 1-hexene, some minor modifications of the peaks can also be observed, especially for the Mo=O peak around 1000 cm^{-1}, where the shoulder on the right becomes a small peak in the IR spectrum with the PCM.

The presence of 1-hexene, simulated at least qualitatively with the two approaches shown in this section, appears not to modify substantially the picture obtained by the calculations of isolated molecules. Exploring different configurations and solvents may change the picture more significantly, however an extensive investigation of this aspect lies beyond the purpose of this work.

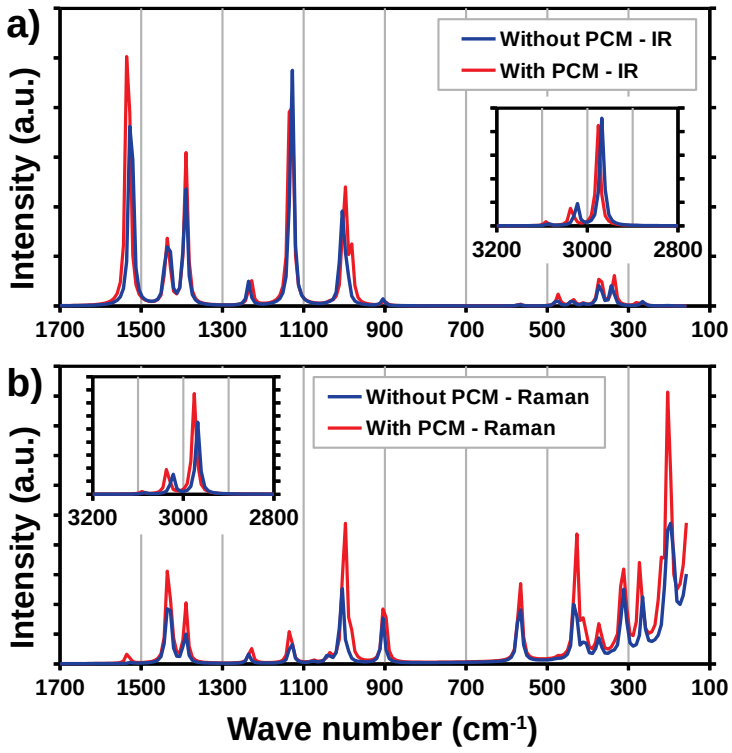


Figure 2.12: a) IR and b) Raman spectra of sMoDTC calculated with (red) and without (blue) the PCM. The region of the C-H vibrations is shown in the insets. No shift nor scaling were performed on the spectra.

2.4 Conclusions

In this work we have presented a DFT study aiming at a comprehensive characterization of MoDTC complexes, which includes the analysis of the structural, electronic and vibrational properties. Isomerization, oxidation and dissociation have also considered along with the effects of hydrocarbon chain length. Our results on the molecular structure, namely bond lengths and angles, are in agreement with the few existing data in literature. We have demonstrated that the most energetically favourable decomposition path for isolated MoDTC complexes, here referred to as *Cut 1*, involves the breaking of the Mo-S (Mo-O) bonds connecting the metal atoms to the S (O) atoms attached to the carbamate group. The relative stability of

Table 2.6: Comparison of lengths and angles of selected bonds of sMoDTC calculated with Gaussian, with and without employing the PCM to simulate the effect of the solvent. The numbers in brackets follow the numbering proposed in Figure 1 of the main text. The bond lengths are expressed in Å, while the bond angles are expressed in °.

Bond	Without PCM	With PCM
H(1)-C(2)	1.101	1.100
C(2)-N(3)	1.457	1.459
N(3)-C(4)	1.340	1.334
C(4)-S(5)	1.726	1.730
S(5)-Mo(6)	2.494	2.488
Mo(6)-O(7)	1.682	1.685
Mo(6)-S(8)	2.330	2.333
Mo(6)-Mo(6')	2.826	2.828
Angle	**Without PCM**	**With PCM**
C(2)-N(3)-C(2')	115.5	115.3
C(2)-N(3)-C(4)	122.3	122.4
N(3)-C(4)-S(5)	123.7	124.0
S(5)-C(4)-S(5')	112.5	112.1
C(4)-S(5)-Mo(6)	88.2	88.4
S(5)-Mo(6)-O(7)	105.1	105.2
Mo(6)-S(8)-Mo(6')	74.7	74.6
O(7)-Mo(6)-Mo(6')	105.4	105.2

all the considered isomers indicates that the most favourable position for O atoms is the ligand position. We also predict that oxidation is a favoured process both for isolated molecules and molecules adsorbed on an iron surface. The analysis of the partial charge on Mo atoms suggests that the iron surface is needed in order to reach the +4 oxidation number observed in MoS_2. Alkyl groups longer than methyl groups in the carbamate units can stabilize the fragments obtained by the dissociation, therefore easing the dissociation process. Concerning simulated vibrational spectra, the peak assignment is in agreement with the ones observed in experimental studies and most features in the spectra match with those obtained from experimental results from real samples. We highlighted features in the spectra that can help to identify the oxidation and the isomerization of the molecule. As a further step in the understanding on the functionality of MoDTC as a lubricant, we will investigate the impact of the metal substrate on the above described analysis, with the aim of clarifying the dissociation mechanism of MoDTC in tribological conditions.

Chapter 3

Tribochemical Reactions of MoDTC Lubricant Additives with Iron by Quantum Mechanics/Molecular Mechanics Simulations

3.1 Introduction

In the pursuit of more sustainable solutions to the environmental challenges, friction modifiers play a fundamental role in attempting to minimize energy losses. Organo-molybdenum compounds are among the most successful friction modifiers in boundary lubrication regime, where the asperity contact at the steel/steel interface generates extreme tribological conditions [93, 158]. The success of molybdenum dithiocarbamates (MoDTC) additives in reducing friction in automotive applications is, in fact, well established. It is known that the beneficial effect of this class of organo-molybdenum compounds resides in the possibility to generate layers of molybdenum disulfide (MoS_2) in tribological conditions [3]. Recent works regarding MoDTC complexes have demonstrated their capability to reduce friction also at metal/diamond-like-carbon and metal/rubber contacts [159–161] and promising applications have been described in combination with textured metallic surfaces [162] and nanoparticles [163, 164]. While a wide experimental research has been carried out to describe the chemical and tribological behavior of MoDTC in engine oils and its interaction with ZnDTP [30, 120, 165, 166], little attention has been paid to the fundamental steps of the tribochemical reaction that forms the beneficial MoS_2 tribolayers. The first elementary step of this reaction is the dissociation of the molecule into two separated fragments. Grossiord et al. characterized the formation of the MoS_2 layers by means of analytical tribology and proposed a mechanism for the dissociation of MoDTC [101]. They suggested that these compounds undergo a homolytic breaking between the sulfur atoms of the dithiocarbamate (DTC) units and the molybdenum atoms. Khaemba et al., on the contrary, proposed that the bond rupture occurs between the carbon and sulfur atoms of the DTC, leaving the S atoms attached to molybdenum [102]. The actual mechanism of the dissociation of MoDTC is still debated to this day. In a previous study, our simulations attempted to quantify the strength of the bonds broken at the early stages of the reaction. We found that for isolated complexes the most favorable way of cutting the molecule in two fragments is between S and Mo atoms, in agreement with Grossiord's proposition [167]. However, the presence of a metallic substrate may modify this picture, because the stabilization effect provided by the iron atoms can vary among the different fragments obtained in the dissociation. Onodera et al. investigated the interaction between one of the possible structures of MoDTC and a (001) iron surface by means of a hybrid quantum chemical / classical molecular dynamics approach based on the tight-binding approximation [141]. They observed the elongation of the bond between Mo and the O atoms in ligand position, i.e. between the C atom of the DTC and molybdenum, according to the notation of Khaemba [102], and they identified the role of iron as a catalyst in the dissociation of MoDTC. However,

Reproduced with permission from **S. Peeters**, P. Restuccia, S. Loehlé, B. Thiebaut, M. C. Righi, J. Phys. Chem. C 2020, 124, 25, 13688–13694. Copyright 2020 American Chemical Society.

this bond stretching was observed in a few hundreds of femtoseconds, which is a short time interval in order to draw conclusions on the fundamental steps of the molecular decomposition, as we show in detail in the following paragraphs.

In this work we investigated the dissociation of MoDTC by considering three dimeric structures, in which the position of O atoms and the ratio between S and O atoms varies. In a previous study, our simulations showed that the ligand position, between C and Mo atoms, is the most favorable position for the O atoms and we found that the oxidation of the complexes is generally favorable. [167] These results were in agreement with the experimental observations of De Feo et al. [123], who demonstrated that MoDTC structures become spontaneously rich in oxygen, which eventually occupies the ligand position, in addition to the terminal position, i.e. on top of Mo, due to a multi-step reaction. Therefore, it is worth to compare complexes with different position and ratio between S and O atoms to better understand the role of oxygen in the dissociation process of MoDTC.

Here, the interaction of these complexes with a metallic substrate was investigated first by performing dynamic simulations following a Quantum Mechanics / Molecular Mechanics (QM/MM) approach [87, 88] based on the density functional theory (DFT). Such computational scheme allows an accurate description of the chemical reactions while maintaining the calculations computationally affordable. The region in which the chemical reactions take place is treated at the quantum mechanical level by explicitly taking into account the electrons of the reacting chemical species. The electronic structure of the atoms far away from the interface can be neglected, as they do not take part in any chemical reaction. However, the presence of these atoms is necessary to absorb part of the atomic displacements and oscillations generated by the reactions at the interface. Therefore, they are assigned to the classical region, as they are treated by means of classical mechanics. Our recent studies showed that the QM/MM approach can be very promising applied to tribochemistry, as it properly describes the chemical reactions occurring at the sliding interface with a significant speedup with respect to simulations where all the atoms are treated at the quantum level. Here we extend the field of application of the QM/MM approach to investigate the mechanism of function of lubricant additives, which is rather challenging because of the complexity of the systems and the processes involved. [90, 91]

After describing the tribological behavior of the three MoDTC complexes under the effect of load and shear motion of the interface by means of the QM/MM approach, we carried out additional static simulations to confirm and quantify the results obtained from the dynamic simulations. We calculated the adsorption energy of the complexes and their dissociation energy on the clean iron surface. We considered iron, which is different from steel, as it can be an appropriate model for the native metallic surfaces exposed during scratching [168]. Our aim is to clarify the dissociation mechanism of MoDTC, describe quantitatively the interaction of these complexes with an iron surface and understand its catalytic effect, in order to shed some new light on the tribochemical reactivity of organo-molybdenum friction modifiers.

3.2 Methods and systems

In this work we considered the three MoDTC complexes shown in Figure 3.1, which will be referred to as standard MoDTC (sMoDTC), Isomer H and Substitution L, by following the nomenclature adopted in our previous publication, where these complexes were extensively described [167]. The metallic substrate was simulated by considering iron slabs, with the molecules interacting with the (110) surface, as it is the most stable surface for iron [146].

The QM/MM calculations contained two sMoDTC (Simulation A) or two Substitution L (Simulation B) complexes per $7 \times 3\sqrt{2}$ simulation cell, intercalated between (110) iron slabs, each composed by eight

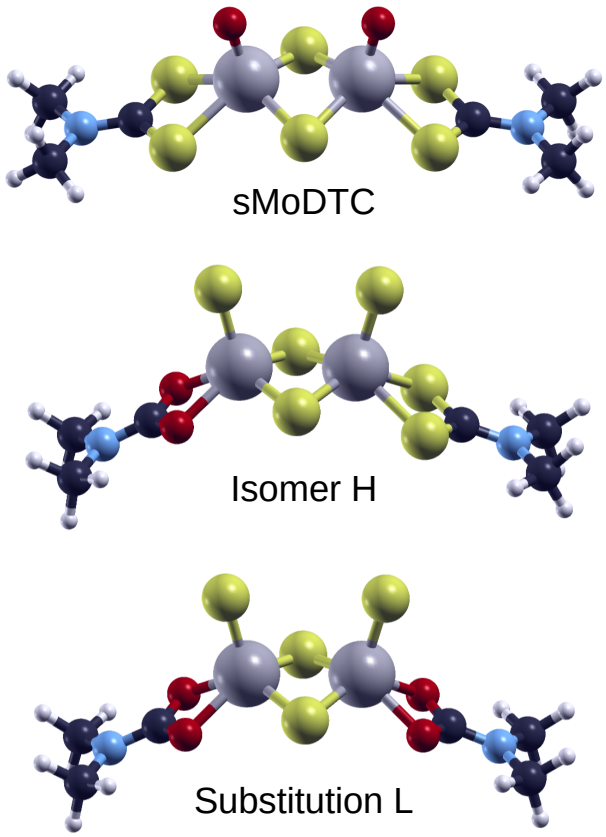


Figure 3.1: Chemical structures of sMoDTC, Isomer H and Substitution L. White, black, light-blue, red, yellow and grey atoms correspond to H, C, N, O, S and Mo atoms, respectively.

atomic layers. The two molecules and two iron layers, one for the top and one for the bottom iron slabs, belonged to the quantum region, while the classical region was composed by the remaining fourteen iron layers, seven for each iron slab. Figure 3.2 shows a schematic representation of the QM/MM system, which was prepared by following a procedure explained in the Supplementary Information. Inside the chemically reactive region, the interactions among the atoms were treated at the DFT level. In this region, the electronic structure of the atoms was optimized at each step of the simulation by the Quantum ESPRESSO package [128], effectively making this computational approach a Born-Oppenheimer molecular dynamics technique [86]. The interactions among the atoms in the classical region and at the border between the quantum and the classical regions were described by the embedded-atom method [169, 170], with the overall dynamics handled by the LAMMPS suite [171]. The total energy of the system E_{tot} was obtained through a subtractive scheme [89]:

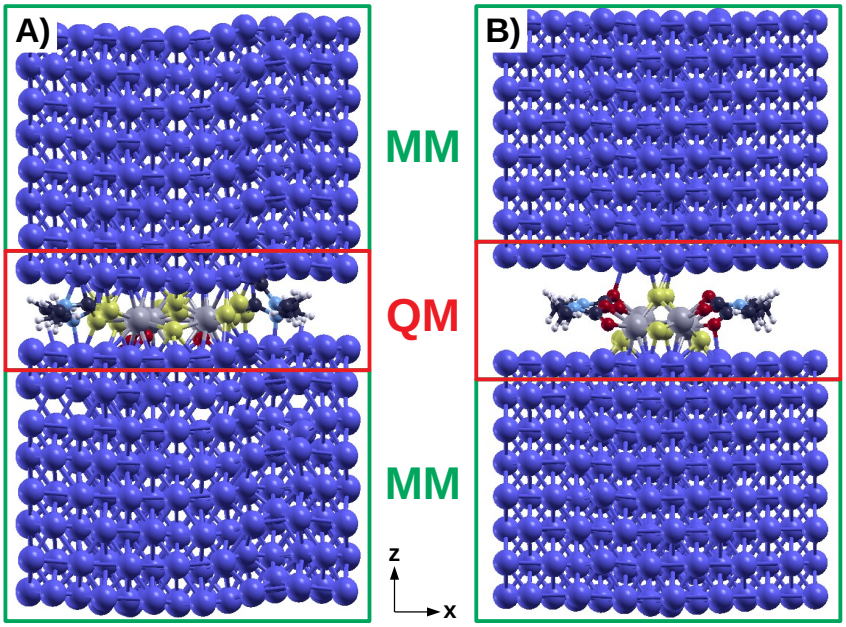


Figure 3.2: Schematic representation of the partitioning between classical (MM, green) and quantum (QM, red) regions in the QM/MM simulations. Lateral views of the initial configurations for A) sMoDTC and B) Substitution L. The initial configurations of the QM/MM simulation are obtained by structural relaxation under an uniaxial compressive stress of half the magnitude as the one applied during the QM/MM simulation (see Supplementary Information). The blue coloring identifies iron atoms.

$$E_{tot} = E_{\mathrm{tot,MM}} - E_{\mathrm{crr,MM}} + E_{\mathrm{crr,QM}} \tag{3.1}$$

where $E_{\mathrm{tot,MM}}$ is the energy of the whole system computed classically and $E_{\mathrm{crr,MM}}$ and $E_{\mathrm{crr,QM}}$ are the energies of the chemically reactive region, computed classically and at the DFT level, respectively. By following this scheme, the forces of the whole system are first computed by means of classical force fields. Then, the forces of the chemically reactive region are calculated at the quantum level and substituted within

the same region. In this way, it is possible to maintain an easy implementation, which does not require any further assumption to couple the quantum and the classical regions, as the forces at the boundary are provided by the force fields. In the simulations, a thermalization process, lasted one picosecond, allowed the nuclei to globally reach 300 K thanks to a Nosé-Hoover thermostat with a damping parameter of 33.3 fs. An initial ensemble of velocities for all the nuclei was generated from a Gaussian distribution with a standard deviation scaled to produce a temperature of 300 K. After 1 ps of simulation, the temperature of the quantum region was left to evolve freely, while the classical atoms continued to be thermostatted, absorbing the heat generated at the interface. This approach can be considered as an intermediate scheme between a *base* and a *full thermostatting* [172]. A lateral motion of the iron slabs along the x axis was introduced to simulate the sliding of the two surfaces. A velocity kick of 300 m/s in two opposite directions for the top and bottom slabs was provided to the outermost iron layers at each picosecond of the simulation, in order to counteract the interfacial friction. This value for the sliding velocity was chosen to accelerate the reaction rates in order to observe the desired chemical events in a reasonable simulation time. The outermost iron layers also experienced vertical forces that impose a load of 4 GPa to the system for the whole duration of the simulation. Such value for the load is quite large compared to the usual experimental conditions. However, the ideal surface considered in the calculations is meant to represent a nanoasperity contact, where the contact pressures can reach values way above the parameters imposed in the experimental setups [79, 82, 91]. Furthermore, the chosen value for the load is still much lower than the Young's modulus of iron, ensuring no failure of the material in these conditions. The timestep of the simulation was 1 fs and periodic boundary conditions in all the directions were employed for the supercells, as the current implementation of the QM/MM scheme requires the same simulation cell and periodicity conditions for the quantum and classical subsystems. A cell height of approximately 48 Å allowed to obtain a separation of about 15 Å between the vertical periodic replicas of the whole QM/MM system.

All the DFT calculations in this work were carried out by employing the Perdew-Burke-Ernzerhof (PBE) [127] approximation for the exchange-correlation functional. The pseudopotential/plane wave approach was adopted. Ultrasoft pseudopotentials were employed and the plane wave expansion of the electronic wave function (charge density) was truncated using a 30 Ry (240 Ry) cutoff for the kinetic energy. The value of 30 Ry for the kinetic energy cutoff of the wave functions was chosen to obtain an accurate description of the iron bulk, as shown in a previous work from our group [146], while the energy difference between two isolated MoDTC structures was at convergence below the threshold of 1 meV per atom, as explained in Appendix B. Spin polarization was taken into account. We added a Gaussian smearing of 0.02 Rydberg to better describe the occupation of the electronic states of the metal around the Fermi energy. Integrations were performed at the gamma point in the case of the QM/MM simulations, while the sampling of the Brillouin zone was performed by using a 1x3x1 grid in the case of the static calculations. For adsorption and dissociation energy calculations, $8 \times 2\sqrt{2}$ simulation cells and 4-layer iron slabs were used. All the geometry optimizations were stopped when the total energy and the forces converged under the thresholds of $1 \cdot 10^{-4}$ Ry and $1 \cdot 10^{-3}$ Ry/bohr, respectively.

3.3 Results and Discussion

3.3.1 QM/MM simulations

Snapshots of the QM/MM simulations are shown in Figure 3.3, in a top view representation of the interface, with the iron atoms hidden for clarity. Both sMoDTC and Substitution L are represented. Panels A and B are directly comparable with Panels D and E, as they correspond to the configurations assumed by the

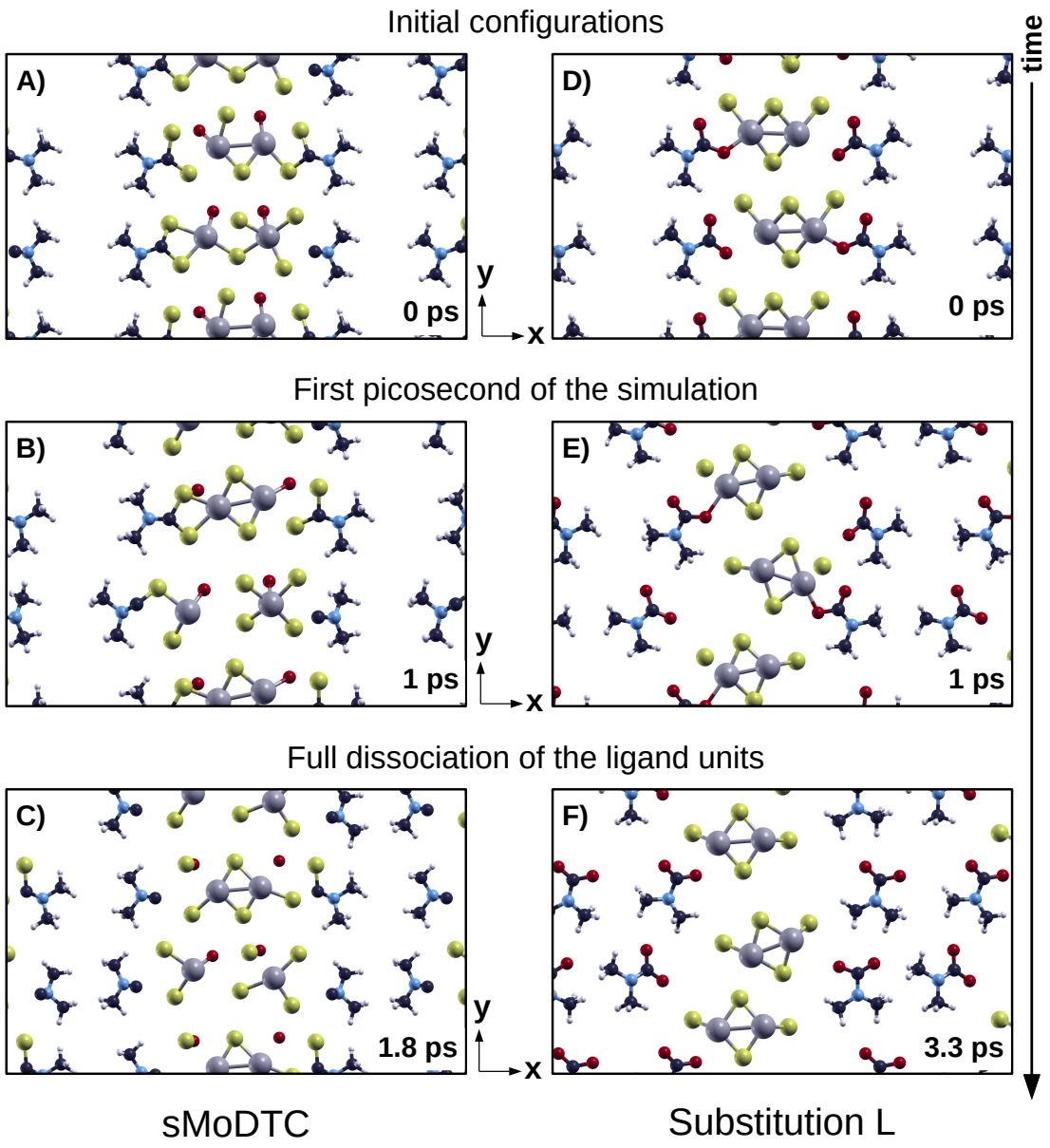


Figure 3.3: Top views of the QM/MM simulations, where the sliding motion of the iron slabs occurs along the x direction. Iron atoms are transparent in the pictures. A) and D) initial configurations, B) and E) configurations after 1 ps, C) and F) configurations after 1.8 ps and 3.3 ps for sMoDTC and Substitution L, respectively.

two structures at the beginning of the simulation and after one picosecond. Panels C and F show the instant in which full dissociation of the two compounds was achieved. Initially, Substitution L appeared to experience a quicker dissociation than sMoDTC, as two carbamate units were already separated from the central unit after one picosecond. However, full dissociation of the DTC units was achieved more quickly for sMoDTC (1.8 ps) rather than Substitution L (3.3 ps). Only after that time the DTC units stayed permanently separated from the central unit. While in the case of sMoDTC the ligand units lost most of the S atoms, leaving $(CH_3)_2NC$- units stabilized by the presence of iron atoms, entire carbamate units were observed in the case of Substitution L. Central units after full dissociation of Substitution L were intact, free of oxygen, and with the proper stoichiometry to form MoS_2 (Panel F), while for sMoDTC these units were too rich in S and O atoms, and the two molybdenum atoms could also be separated far apart (Panel C). This is an indication that the presence of oxygen atoms in ligand position of MoDTC can be beneficial to obtain central units which are ideal to assemble into crystalline MoS_2.

3.3.2 Adsorption and dissociation on iron

In order to verify and quantify the results of the QM/MM simulations, we calculated the adsorption and fragmentation energies of sMoDTC, Isomer H and Substitution L on iron. First, the complexes were put close to the surface, with the terminal atoms pointing to the iron atoms. The result of the geometry optimizations, visible in Panels A, B and C of Figure 3.4, showed that the position of oxygen in the molecule plays a role in the chemisorption process. The sMoDTC molecule, with oxygen atoms in terminal position, is not able to fully lie on the surface, as three sulfur atoms on one side of the central unit remain distant from the iron surface. For the other two complexes there is no such hindrance, and five (for the isomer) and four (for the substitution) sulfur atoms reach the surface. In particular, two sulfur atoms of Substitution L detach from the central unit attempting to occupy the hollow sites of the iron surface. This phenomenon is reflected upon the adsorption energies E_{ads}, calculated as:

$$E_{ads} = E_{\text{tot}} - E_{\text{mol}} - E_{\text{iron}} \tag{3.2}$$

where E_{tot}, E_{mol} and E_{iron} are the total energies of the system composed by the molecule and the iron slab at the end of the optimization process, of the molecule alone, and of the iron slab alone, respectively. The adsorption energies turned out to be -4.33, -7.84 and -7.17 eV, for sMoDTC, Isomer H and Substitution L, respectively. All the calculated values of the adsorption energies are compatible with chemisorption, with the isomer and the substitutional molecule achieving the highest energy gain upon adsorption.

In order to verify which is the most probable dissociation pattern for sMoDTC, Isomer H and Substitution L on iron, we calculated the total energies, after geometry optimization, of their fragments adsorbed on iron, in the same supercell employed for the adsorption calculations. We considered fifteen different fragments, visible in Figure 3.4, to take into account two steps of the fragmentation, i.e. the dissociation of the first and then the second DTC unit. We considered two possible ways of dissociating the complexes, by following the same nomenclature employed in our previous work: Cut 1, in which both O or S atoms in ligand position remain on the ligand after the dissociation, and Cut 3, in which the O or S atoms remain attached to Mo. Cut 2, which is not considered here, is the intermediate situation in which one of the two atoms in ligand position remains with the ligand unit, while the other atom remains attached to the Mo atom.

Due to the asymmetry of Isomer H, there are two possibilities to perform the two dissociative steps: first the carbamate unit and then the dithiocarbamate unit are detached (O→S), or vice versa (S→O). We calculated the dissociation energy as the difference between the total energies of the fragments adsorbed on iron and the entire molecule adsorbed on iron, as explained more extensively in the Supplementary Information. We summarize the results of this analysis in Table 3.1.

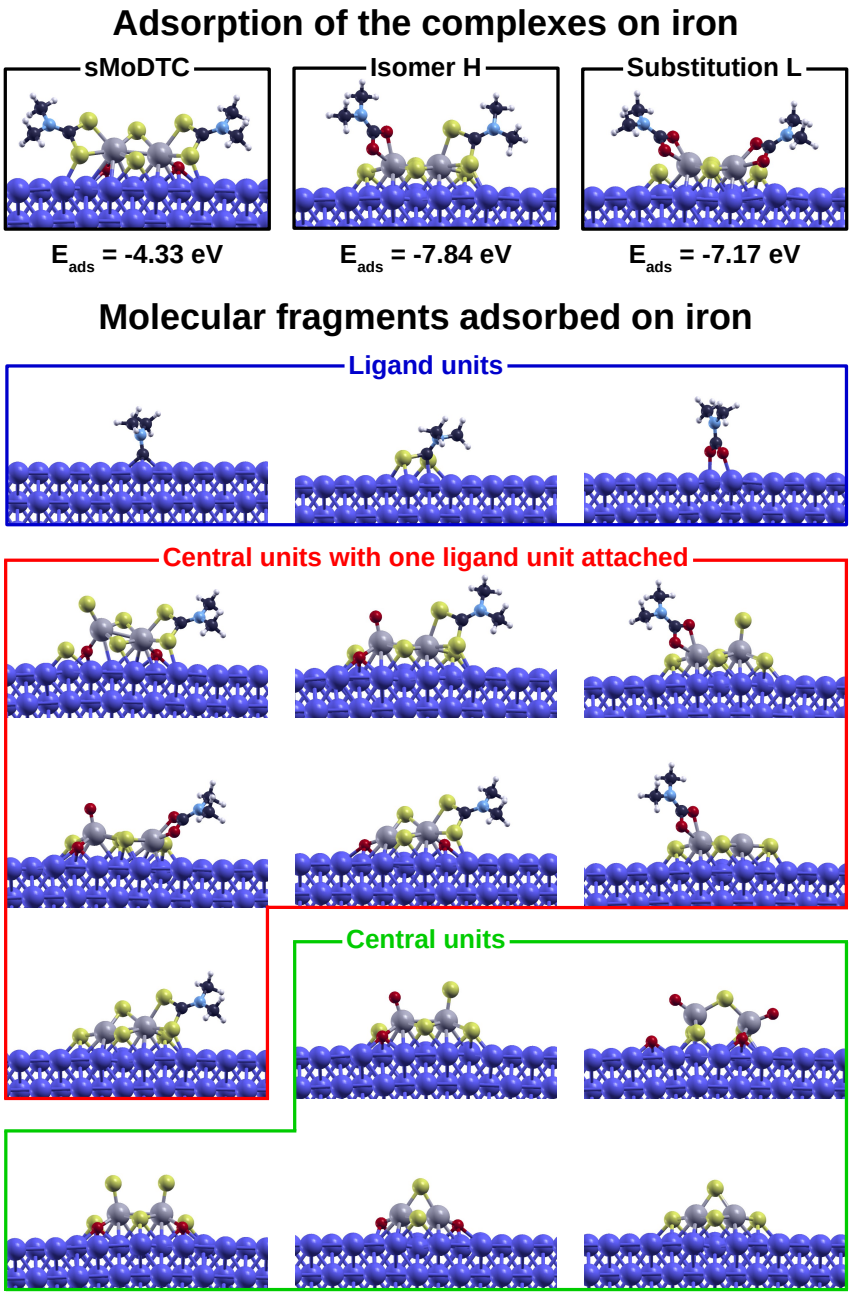


Figure 3.4: Optimized geometries of the three complexes, with their corresponding adsorption energies, and their fragments adsorbed on iron.

Table 3.1: Fragmentation energies of the three complexes on iron. The reaction energies to detach the first fragment and then the second one are reported for each of the two dissociative patterns considered. For Isomer H, the symbol (O→S) means that first the carbamate unit and then the dithiocarbamate unit are detached, while for (S→O) the opposite pattern is considered. Energies are in eV.

	Cut 1		Cut 3	
Complex	First step	Second step	First step	Second step
sMoDTC	-1.61	-0.79	-1.68	-3.04
Isomer H (O→S)	0.58	-1.09	-0.18	-1.74
Isomer H (S→O)	-0.74	0.23	-1.74	-0.18
Substitution L	-0.29	0.56	0.13	0.08

For sMoDTC, both Cut 1 and Cut 3 are favorable on the iron surface, with Cut 3 appearing to be the most favorable fragmentation pattern. In fact, while the first step of the dissociation is energetically very similar for Cut 1 and Cut 3, the products obtained from Cut 3 are much more stable than the ones of Cut 1, after the second step. This is in contrast with the situation of an isolated complex, for which Cut 1 is the most favorable dissociative pattern [167]. The iron surface plays a key role in stabilizing the products of the dissociation and favors a fragmentation mechanism that would be the least favorable for the isolated compound. Therefore, we expect to observe the C atom of the dithiocarbamate unit, which is usually attached to S atoms, directly chemisorbed on the iron surface. The two S atoms belonging to the ligand position should remain close to the Mo atom, when the central unit is adsorbed on iron.

The most favorable fragmentation appears to be Cut 3 for Isomer H as well. In particular, when the first unit to detach is a carbamate unit, Cut 3 is just barely favorable in the first step, while the second step is about ten times more favorable than the first one. When the dithiocarbamate unit is detached first by following the pattern of Cut 3, the energy values are simply reversed in order with respect to the previous case. For Cut 1 the situation appears to be more complex. The dissociation of a $(CH_3)_2NC$ unit, leaving two oxygen atoms attached to the Mo atom, is not favorable, while the subsequent step is favorable. When the dithiocarbamate unit is detached first, the energy values are slightly different from the latter case, due to the different interactions arising between the atoms of the central units with dangling bonds and the metallic substrate.

Cut 1 is the most favorable way of detaching the first carbamate unit of Substitution L, in contrast with sMoDTC and Isomer H. It is preferable, however, to detach the second carbamate unit with Cut 3, as the energy cost is lower. This reveals that oxygen atoms in MoDTC can play an important role in governing the dissociation process of the (dithio)carbamate units. The presence of O atoms in ligand position makes Cut 1 more favorable than Cut 3 for the dissociation of the first carbamate unit of Substitution L on iron. As expected, the metallic substrate has a deep impact on the stabilization of the resulting fragments. While the most favorable fragmentation of isolated sMoDTC is Cut 1, the same complex on iron most likely undergoes dissociation by following Cut 3. These results fully support the predictions offered by the dynamic simulations and suggest that the two proposed mechanisms for the dissociation of MoDTC are both valid, as the most probable fragmentation pattern varies by changing the ratio between S and O atoms in ligand position. The mechanism proposed by Grossiord is in fact most likely to occur when O atoms are in ligand position, while the mechanism proposed by Khaemba is most probable when S atoms are in ligand position.

3.3.3 Discussion

The QM/MM calculations showed that the dissociation of MoDTC complexes can be completed in the first picoseconds of the simulation. Such kinetics undoubtedly depends on the tribological conditions of the system, as the rate of the chemical reactions is strongly influenced, for instance, by temperature and the applied load. Sufficient simulation time must be considered, though, to capture the whole dissociation process and draw conclusions on the possible products of the tribochemical reactions. Onodera et al. observed a Mo-O bond elongation in 100 fs of a tight-binding-based hybrid quantum chemical / classical molecular dynamics simulation [141]. However, we confirmed that the Mo-O stretching vibration is found at 1000 cm^{-1} in the vibrational spectrum [167], corresponding to a period of around 33 fs. This means that the Mo-O bond vibrates only a few times in such a short timescale, even in tribological conditions. Therefore, our simulation time seems to be more adequate to describe the bond breaking between ligand and central units of MoDTC. Furthermore, the hybrid approach employed by Onodera and coworkers relies on the calculation of the properties of the quantum region by means of a tight-binding technique, which in turns requires several parameters. Such parameters are determined by DFT calculations. The advantage of our approach is the direct computation of all the chemical properties of the tribological system at the DFT level without further parametrization.

Our QM/MM simulations provided reliable results even by using one layer per iron slab in the quantum region, which is a rather severe approximation. This choice was also made by Onodera et al. in their study, and we additionally estimated the extent of such approximation on the adsorption of sMoDTC. It turns out that by adsorbing sMoDTC on top of an iron bilayer, with the bottom layer fixed, an additional sulfur atom in the bridging position of the complex adsorbs on the surface, while the geometry of the rest of the system remains almost identical. The adsorption of sMoDTC on an iron trilayer, with the bottom layer fixed, leads to a molecular geometry identical to the case of the bilayer, with an adsorption energy which is 1 eV higher, hence less favorable, in the case of the trilayer. With less iron layers, the surfaces become more reactive, hence stickier. However, we reasonably believe that the trajectories obtained by the QM/MM simulations are qualitatively consistent with the predictions offered by the static calculations and no spurious products were generated due to approximation of the iron slab to a combination of a single quantum and seven classical atomic layers. In fact, all the reactants and the products of dissociation can bind with an increased adsorption energy to the stickier iron surface, and the resulting trajectory is simply accelerated with respect to the case of a thicker iron slab.

Our QM/MM simulations revealed the important role of oxygen in governing the dissociation mechanism of MoDTC. De Barros Bouchet and coworkers described the decrease in the lubricating performance due to the oxidation of MoDTC, which has an impact on the number, the shape and the composition of the MoS_2 sheets [121]. They found that the presence of ZnDTP allows MoDTC to maintain sufficient friction reduction properties even when 50% of the additive are degraded by oxidation, because of the possibility to replenish the S atoms needed to build MoS_2. Our simulations support those findings, as Substitution L, which is a slightly oxidized MoDTC compound, appears to be a better candidate in producing small units of molybdenum disulfide with the proper stoichiometry. Some authors pointed out that the presence of oxygen atoms in MoS_2 sheets is unavoidable in the synthetic process and by mere exposure to ambient conditions [173, 174]. The lubricant properties of pristine MoS_2, however, is unrivalled with respect to layers of MoS_2 containing also oxygen. Therefore, we believe that controlled oxidation of MoDTC structures may also have a beneficial effect in the formation of MoS_2, especially when the O atoms are in ligand position.

This study demonstrates the merits of ab-initio calculations and, particularly, the QM/MM approach in tribochemistry to identify efficient lubricant additives. The insights provided by these simulations can be valuable in order to predict new solutions for the general problem of friction reduction.

3.4 Conclusions

In this work, we presented the application of a recently-developed QM/MM technique to the dissociation of MoDTC, which is a problem of key relevance in understanding the mechanism of function of Mo-based lubricant additives. The QM/MM simulations demonstrated that the dissociation mechanism of MoDTC depends on the level of oxidation of the complex, as compounds with oxygen atoms in ligand position tend to generate central units with the same chemical composition and stoichiometry of MoS_2. Static calculations based on DFT confirmed the predictions of the dynamic calculations, as the different dissociation mechanisms reflected the fragmentation energies calculated for the MoDTC compounds, and revealed that such mechanism strongly depends on the presence of the metallic substrate. A further step of the analysis, which will be described in a forthcoming article, is to consider also passivated metallic surfaces and the effect of oxygen in the substrate, in order to better describe the first tribochemical events, when the native surface is yet to be reached. The interaction of different MoDTC structures is also an important aspect to evaluate, because the adsorbed fragments of these compounds need to cluster in order to build the MoS_2 tribolayer. An attempt to tackle this complicated issue is presented in Appendix C as a preliminary study.

The QM/MM approach was proven to be extremely valuable for tribochemistry, as it provided the necessary insight to clarify the debated dissociation mechanism of MoDTC. Such an approach appears to be very promising for the design of new materials to reduce friction, where the chemistry of the species active in a tribological environment must be accurately taken into account.

Chapter 4

The Run-In Period of MoDTC Lubricant Additives: The Effect of Surface Oxidation by QM/MM Simulations and Tribological Experiments

4.1 Introduction

Friction reduction is a challenge of fundamental importance for energy saving in the automotive industry. The functionality of currently employed friction modifiers still needs to be completely understood in order to design more sustainable lubricant additives with improved performances. Molybdenum dithiocarbamates (MoDTCs) are a class of widely employed additives for engine oil capable of reducing friction at the steel on steel contact, due to the formation of layers of molybdenum disulfide (MoS_2) [3], which is a well-known solid lubricant. MoDTC complexes, in tribological conditions, undergo molecular dissociation and the originated fragments can recombine to form the slippery tribolayers. The dissociation mechanism of MoDTC is debated, as two different patterns were proposed for the first steps of the reactions, based on experimental observations [101, 102]. Recently, we showed that different dissociation mechanisms are expected for different isomers that can be distinguished by the position of sulfur and oxygen atoms in the complexes [175]. Another relevant aspect in the tribochemistry of MoDTC complexes is the role played by oxygen. De Feo et al. described the quick oxidation of MoDTC-containing samples when heated at 160°C [123]. The chemical transformations occurring during the oxidative degradation impact the dissociation mechanism of MoDTC and its lubricating properties due to the different morphology and composition of the generated MoS_2 films [173]. Several studies showed that the presence of zinc dithiophosphates (ZnDTP), common anti-wear additives, is beneficial to achieve low friction coefficients [30, 120, 165, 166]. Moreover, interactions between the additives and the substrates play a fundamental role in determining the efficiency of the lubrication [176]. When MoDTC is added to the lubricant oil during steel on steel contacts, low friction can be achieved after a run-in period, the duration of which can be influenced by additive-substrate interactions [101, 102]. During scratching, the passivating layers of the metallic surfaces can be removed and the native metal can be exposed [168], increasing the rate of the tribochemical reactions. In fact, a few authors suggested that this mechanism could initiate the tribochemistry of MoDTC [177, 178]. However, Khaemba observed that the formation of MoS_2 occurs even in presence of oxidized surfaces [179]. Here, we combine theoretical and experimental investigations to elucidate the debated effect of oxygen as a passivating element on iron surfaces in the dissociation of MoDTC. In particular, we compare density functional theory (DFT) and quantum mechanics/molecular mechanics (QM/MM) [87, 88] simulations, carried out to describe the adsorption of MoDTC on the clean and oxygen-passivated surfaces, with tribological tests performed on mirror polished and passivated steel discs. The QM/MM approach was in fact shown to be particularly convenient to study such complex reactivity [175], as it allows to accurately treat the electronic properties of the chemically active species while keeping the computation reasonably affordable [90, 91]. The comparison between the ab-initio calculations and the tribological tests aims at a better understanding of the role of

oxygen as a passivating agent in the tribochemistry of MoDTC and, in particular, in the run-in period.

4.2 Methods and Systems

4.2.1 Experimental Techniques

We verified whether an increase in the amount of oxygen on the surface of a metallic substrate can influence the tribological behavior of MoDTC. Mirror polished discs made of AISI 52100 hardened steel were chosen because of their higher surface homogeneity, with a surface roughness of 0.05 μm, which limits the run-in period, avoiding undesired wear and allowing to focus primarily on the tribochemical activation of MoDTC. All the steel discs were initially cleaned with heptane. The surface of the reference discs consisted of bare steel, while a group of discs was heated in air at 170°C for 7 hours on a temperature-controlled hot plate to promote the exchange of oxygen with the environment. The surface and the lateral profile of the reference and the oxidized discs was analyzed by a FEI Quanta FEG 250 scanning electron microscope coupled to an Oxford X-Max 80 SDD energy-dispersive X-ray spectroscope (SEM-EDX) in approximately 6 mbar of vacuum with a beam of 20 kV and working distance of 1 cm. After the surface analysis, tribological tests were carried out by using an Anton Paar MCR302 rheometer with a T-PID/44 tribology assemply (three balls on disk tribology measurement cell). Each run lasted for 20 minutes, with an exponentially increasing rotation speed from 4.7 mm/s to 377 mm/s over 750 s, an operational temperature of 110°C and a contact pressure of 700 MPa. The lubricant consisted of a mixture of MoDTC complexes, Adeka Sakuralube 525, in a group III mineral oil, Yubase 4, with a resulting concentration in molybdenum of about 500 ppm, and was deposited directly on the disc immediately before the run.

4.2.2 Computational Approach

In order to verify the results obtained by the tribological tests, we investigated the interaction of the two MoDTC complexes, shown in Figure 4.1, with iron. They correspond to the standard MoDTC (sMoDTC) structure and the most stable isomer, named Isomer H in our previous work [167], where the oxygen atoms are moved from the terminal position, on top of molybdenum atoms, to the ligand position, between carbon and molybdenum atoms. We considered the (110) surface of iron, which is the most favorable one for this metal [146]. Periodic supercells were employed for all the calculations. In the adsorption calculations, supercells with a $8 \times 2\sqrt{2}$ in-plane size were used, containing a four-layer-thick iron slab and a single MoDTC molecule adsorbed on it. In these calculations, surfaces passivated by both oxygen and sulfur were considered with a coverage of 0.25 monolayers, with the oxygen and sulfur atoms occupying the most stable adsorption sites, namely the threefold and the long bridge sites of the Fe(110) surface, respectively. [180, 181].

In the QM/MM simulations, two MoDTC complexes were put in $6 \times 3\sqrt{2}$ supercells and the top and bottom iron slabs were composed by eight atomic layers each. Both clean and oxygen-passivated surfaces were considered in the dynamic simulations. The two molecules at the interface and the two uppermost iron layers of the bottom slab, with the adsorbed oxygen when present, were part of the chemically reactive region (I region), treated at the DFT level by the Quantum ESPRESSO suite [128]. The remaining six iron layers of the bottom slab and the top iron slab (II region) were treated classically, by using the embedded-atom model [169, 170], with the LAMMPS software [171] driving the whole dynamics. A scheme of the QM/MM simulation setup is shown in Figure 4.2. The atoms of the chemically reactive region were repelled by the top slab as they experienced a purely repulsive Lennard-Jones potential. With this potential, the top slab merely acted as a non-interactive wall on the complexes. The geometry of all the iron layers

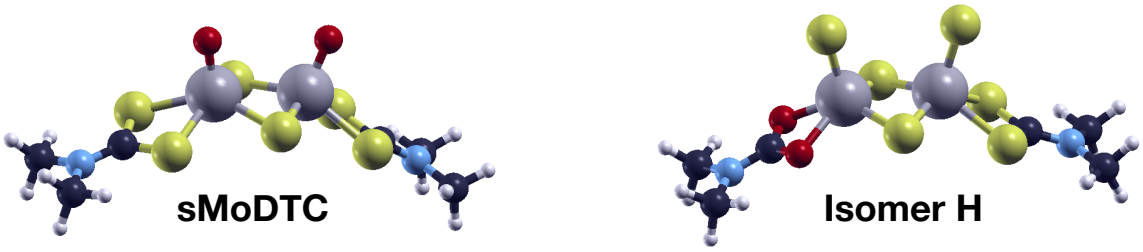


Figure 4.1: Chemical structures of the two complexes considered for the ab initio simulations, namely sMoDTC and Isomer H. The white, black, light blue, red, yellow and grey coloring of the atoms correspond to hydrogen, carbon, nitrogen, oxygen, sulfur and molybdenum atoms, respectively.

of the bottom slab, except for the uppermost one, was kept frozen during the dynamic simulation. As described in a previous publication from our group,[175] the coupling between the two subsystems was realized by employing a subtractive scheme [89]:

$$E_{tot} = E^{\mathrm{I+II}}_{\mathrm{MM}} - E^{\mathrm{I}}_{\mathrm{MM}} + E^{\mathrm{I}}_{\mathrm{QM}} \tag{4.1}$$

where E_{tot} is the total energy of the whole QM/MM system, $E^{\mathrm{I+II}}_{\mathrm{MM}}$ is the total energy of the whole system computed with the classical force fields, while $E^{\mathrm{I}}_{\mathrm{MM}}$ and $E^{\mathrm{I}}_{\mathrm{QM}}$ are the total energies of the reactive region, computed classically and at the quantum level, respectively. An initial thermalization process, lasted one picosecond, allowed the system to globally reach 300 K by employing a Nosé-Hoover thermostat with a damping parameter of 33.3 fs. An ensemble of velocities for all the atoms, except for the frozen ones, was generated from a Gaussian distribution with a standard deviation scaled to produce the temperature of 300 K. After the thermalization process, the temperature of the chemically reactive region was left free to evolve and, in order to simulate the sliding of the surfaces, a shear motion of the top iron slab was applied, with velocity kicks of 600 m/s applied at each picosecond on the external layer of the top slab. The timestep of the simulation was 1 fs. The two complexes at the interface experienced a load of 4 GPa applied on the external layer of the top slab for the whole simulation.

The Perdew-Burke-Ernzerhof (PBE) [127] approximation was chosen for the exchange-correlation functional in the DFT calculations. Ultrasoft pseudopotentials were employed and plane waves were used as a basis set for the wave functions. The expansion of the plane waves (charge density) was truncated using a 30 Ry (240 Ry) cutoff for the kinetic energy. The choice for the value of 30 Ry was justified in previous works [146]. Spin polarization was taken into account to allow the spin multiplicity to vary in all the chemical species. We added a Gaussian smearing of 0.02 Rydberg to ease the convergence of the calculations. The evaluation of the charge density was performed at the gamma point in the case of the QM/MM simulations, while in the case of the static calculations a 1x3x1 Monkhorst-Pack grid was employed. The geometry optimizations were stopped when the total energy and the forces converged under the thresholds of $1 \cdot 10^{-4}$ Ry and $1 \cdot 10^{-3}$ Ry/bohr, respectively.

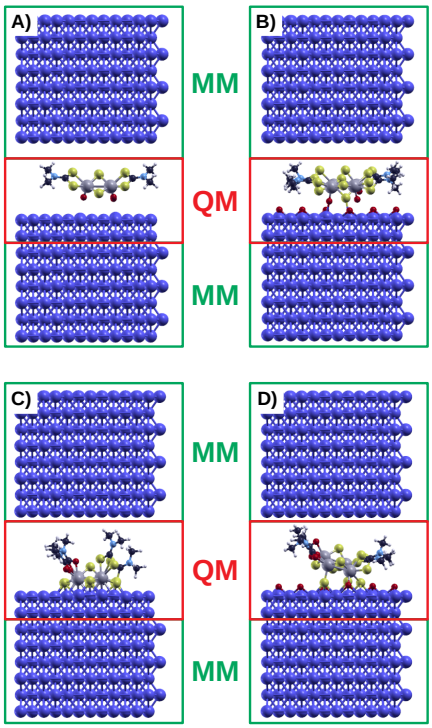


Figure 4.2: Lateral views of the QM/MM systems, with a schematic representation of the partitioning. Initial configurations for sMoDTC and Isomer H on clean (A, C) and passivated (B, D) surfaces, respectively. The blue coloring of the atoms identifies iron atoms.

4.3 Results and Discussion

4.3.1 Characterization and Tribological Tests on the Oxidized Surfaces

Figure 4.3 reports the results of the surface analysis of the bare and the oxidized surfaces employed in the tribological tests. The two different surfaces can be distinguished both with and without microscopy. To the naked eye, the oxidized disc presents a darker color, as shown in the top panels of Figure 4.3, while maintaining the capability to reflect light. The lateral profile of these surfaces reveals that in both the bare and the oxidized surfaces the oxygen concentration is higher in the proximity of the surface, as shown in the bottom panels. However, in the case of the oxidized disc, the amount of oxygen in the bulk decreases quickly with respect to the surface. Since the two discs were originally identical, this result suggests that the increase of the surface concentration of oxygen was effectively achieved. Quantitative analysis of the EDX spectrum reveals, in fact, that the mass percentage of oxygen on the surface becomes three times higher with respect to the reference disc, as expected by the preparation protocol. The uneven distribution of oxygen on the oxidized surface can be attributed to several issues. This preparation protocol was demonstrated to increase the surface concentration of oxygen of the disc, yet the homogeneity of the oxygen distribution cannot be completely controlled. Furthermore, the cut of the steel disc, required to

capture the lateral profiles, might influence the distribution of oxygen. Even though the cutting procedure was equivalent in the two samples, slightly different physico-chemical properties of the surfaces might have led to the generation of different local stresses and temperatures, and consequently a different oxygen distribution on the steel surface.

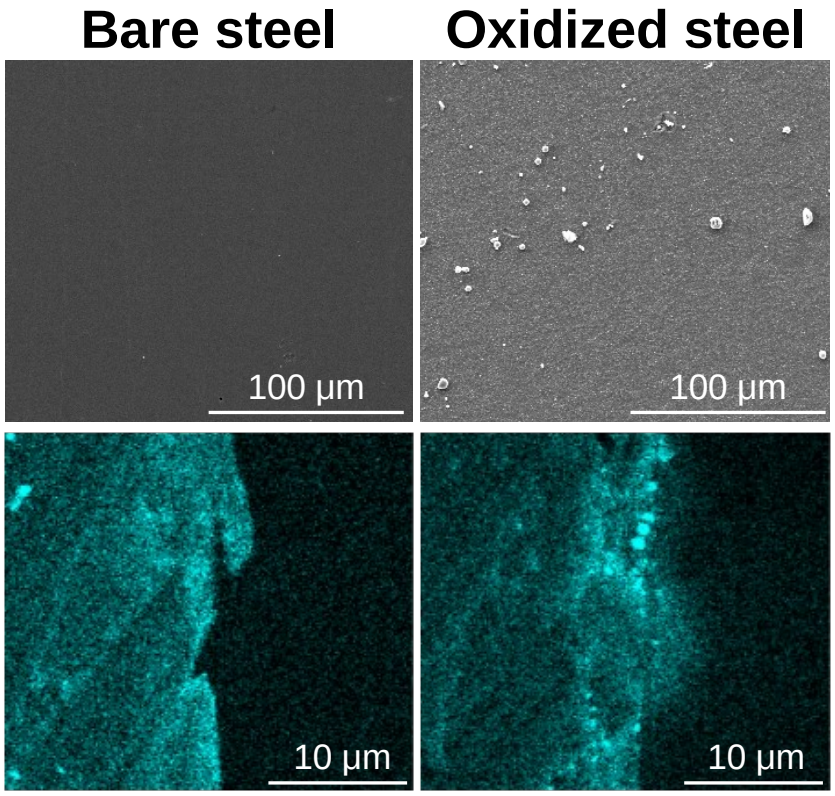


Figure 4.3: Surface analysis of the reference and oxidized steel discs. Top: SEM images of the bare (left) and oxidized (right) surfaces. Bottom: lateral profile of the bare (left) and oxidized (right) surfaces, respectively. The light blue coloring identifies the intensity of the oxygen Kα1 peak.

The tribological tests carried out on these surfaces, shown in Figure 4.4, reveal that the surface oxidation leads to high friction during the run-in period compared to the reference disc. After the first 180 seconds of the run, at approximately 250 rotations, the activation of the MoDTC additives occurs and friction drops to values comparable to the ones of the reference disc, as a sufficient amount of MoS_2 is generated to maintain low friction. Furthermore, the friction coefficient of the oxidized surface becomes even slightly lower than the reference at the end of the run. The high friction in the early stages of the run might be associated to the removal of oxidized material which is not able to fully interact with the MoDTC compounds. After reaching more reactive layers below the oxidized surface, the substrate behaves as it was not oxidized by thermal treatment, and the energy excess due to the initial catastrophic events may contribute to an enhanced reactivity of the MoDTC complexes, leading to an even lower friction coefficient. Furthermore, oxygen in excess could cause a substitution reaction in MoDTC. We have recently discovered that MoDTC

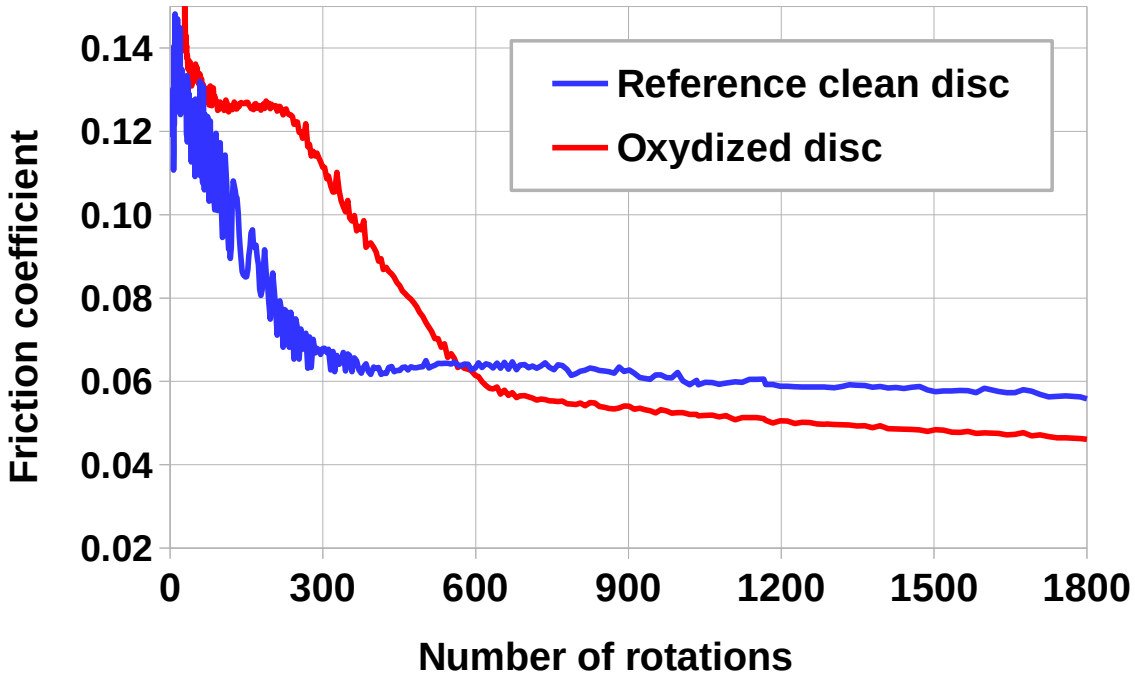


Figure 4.4: Tribological tests of the oxidized and the clean mirror discs under lubrication of S525.

structures rich in oxygen host more preferably the additional O atoms in ligand position, in agreement with experimental observations [123, 167]. Among the many molecular fragments originated by the tribochemical decomposition of the MoDTC structures, clusters containing only Mo and S atoms can be formed from the MoDTC complexes that contain oxygen in ligand position. These molecular clusters are useful precursors for MoS_2 because they present the correct stoichiometry to build the beneficial tribofilm [175]. In order to elucidate this mechanism, we designed the static and dynamic ab-initio simulations presented in the following section.

4.3.2 Molecular Adsorption and Dissociation in Static Conditions

The interaction of the MoDTC compounds with the bare metallic substrate favors their molecular dissociation. Initially, MoDTC must adsorb onto the metallic surface for the dissociation to occur, and passivating agents such as oxygen and sulfur may hinder the adsorption of the additives on iron. To verify this hypothesis, we positioned the sMoDTC molecule on the clean and oxidized surfaces and optimized all the degrees of freedom. Indeed, we observed that oxygen on the iron surface limit the adsorption of sMoDTC, as shown in Figure 4.5. Only the oxygen atoms in terminal position of sMoDTC, pointing in the direction of the surface, are bound to the substrate. All the other atoms are repelled. This behavior is reflected on the adsorption energies E_{ads}, calculated as:

$$E_{ads} = E_{\text{tot}} - E_{\text{mol}} + E_{\text{sub}} \tag{4.2}$$

where E_{tot}, E_{mol} and E_{sub} are the total energies of the whole system, of the complex alone and of the substrate alone in the same simulation cell, respectively. In fact, the adsorption energies of sMoDTC on the oxidized surface in the particular configurations shown in Figure 4.5 is -1.51 eV, compared to -4.33 eV in the case of a clean iron surface [175].

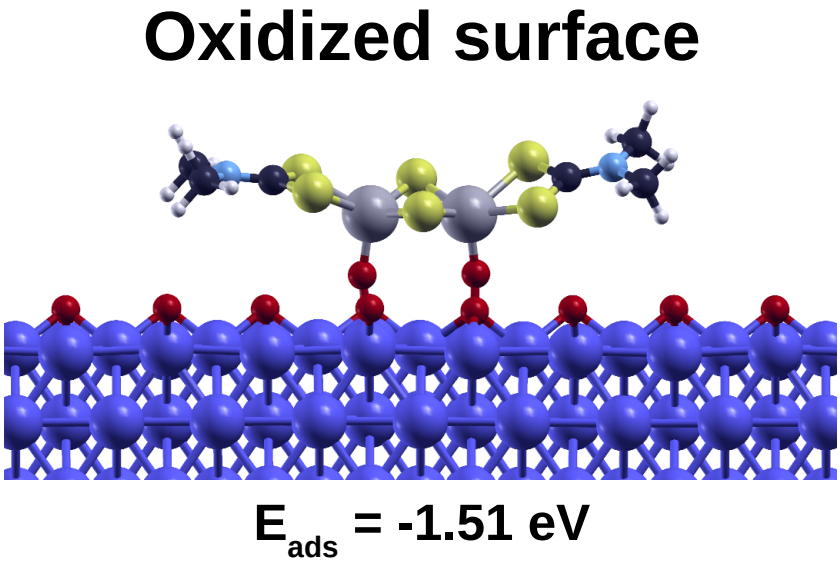


Figure 4.5: Final configuration of the adsorbed sMoDTC complexes on the oxidized surface.

Since the adsorption of MoDTC is limited by the presence of oxygen on the iron surface, the catalytic effect of the substrate in promoting the dissociation of the complexes is decreased as well. Variable-cell calculations in which the molecules withstand a load of 0.5 GPa show that the complexes cannot undergo dissociation when the whole interface is passivated. When only one of the two surfaces is covered, the dissociation of the complexes can occur, due to the interaction of the complexes with the only clean surface, as shown in Figure 4.6. The variable-cell calculations were carried out also considering 2 GPa of load, and the results are equivalent.

4.3.3 Molecular Adsorption and Dissociation in Tribological Conditions

Dynamic simulations offer particularly valuable insights on the mechanism of tribochemical reactions at the atomistic level, because also the sliding motion of the interface can be taken into account, in addition to the applied load. By following the QM/MM approach, it is possible to accurately monitor the formation and the dissociation of chemical bonds in the first picoseconds of the reactions, while maintaining the simulation computationally affordable. For these simulations, a suitable geometry of the systems was chosen to study the effects of the different substrates. The same counter-surface was chosen for all the simulations, in analogy to the experiments. and it was represented simply by a repulsive wall to minimize its chemical

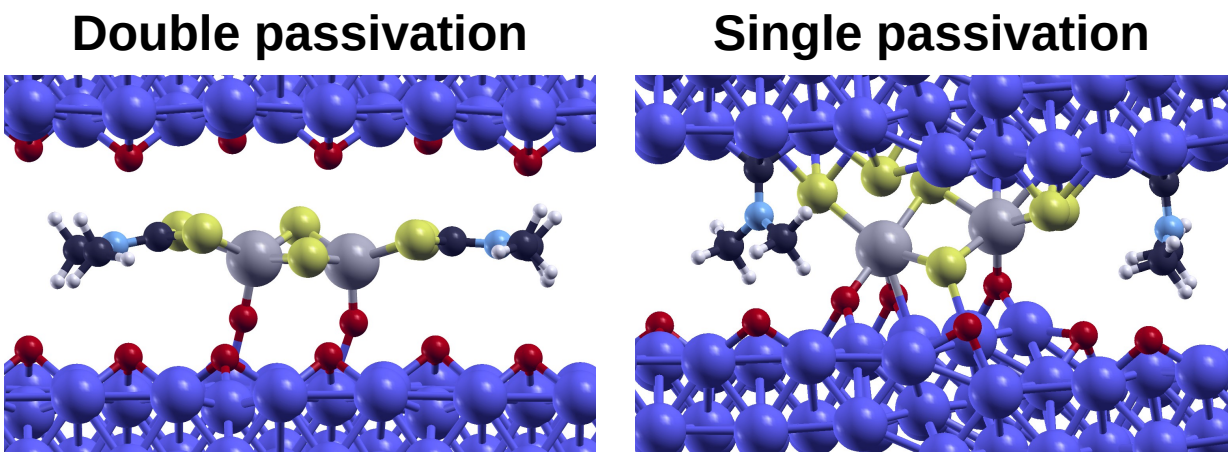


Figure 4.6: Final configurations of the variable-cell calculations with double and single passivating oxygen layers at the iron interface.

effect on the species at the interface. Lateral views of the QM/MM systems at 2 ps of the simulation are shown in Figure 4.7. The complexes are forced to adsorb onto the bottom iron slabs under the effect of load. The dynamic simulations, in agreement with the static calculations, show that the clean surfaces allow the complexes to chemisorb (Panels A, C). Some of the atoms in the ligand position of sMoDTC and Isomer H are close to the surface, where the catalytic effect of the metallic atoms may induce a dissociation according to the pattern shown in our previous work [175]. However, the passivation of iron by oxygen hinders the adsorption of the central units of MoDTC (Panels B, D). In fact, the complexes become flat due to the applied load. The dissociation appears to be less probable in this case, as the metallic substrate cannot efficiently catalyze the chemical reaction. The decreased number of free sites on the surface limits the stabilization effect of the fragments that can be originated upon molecular dissociation.

4.3.4 Discussion

The ab initio calculations showed that an iron surface free of adsorbates is beneficial to chemisorb MoDTC compounds and that the chemisorption of MoDTC is a necessary step in the formation of MoS_2. The dissociation of MoDTC compounds can be activated thermally even in the absence of mechanical stresses. However, shear stress has been demonstrated to promote dissociation at relatively low temperatures [179]. The synergy of the extreme conditions observed during sliding is translated into quick run-in periods, as a sufficient amount of MoS_2 is immediately generated to achieve low friction [177], as observed in the case of the reference clean discs employed in this work. The fact that MoDTC cannot access the catalytic sites of the substrate when the metal is oxidized slows down the production of MoS_2, delaying the typical friction drop. Such mechanism would match the observations by Cousseau et al. [178], who suggest that the removal of the oxidized layers of the substrate, due to the contact of the asperities, is beneficial to promote the transformation of MoDTC into MoS_2.

Khaemba observed that MoS_2 can be formed even when the surface is oxidized [179]. However, the resulting tribolayer is less durable, because it cannot adhere strongly to the substrate. Although our investigation did not focus on the durability of the MoS_2 tribolayers, our simulations can explain these

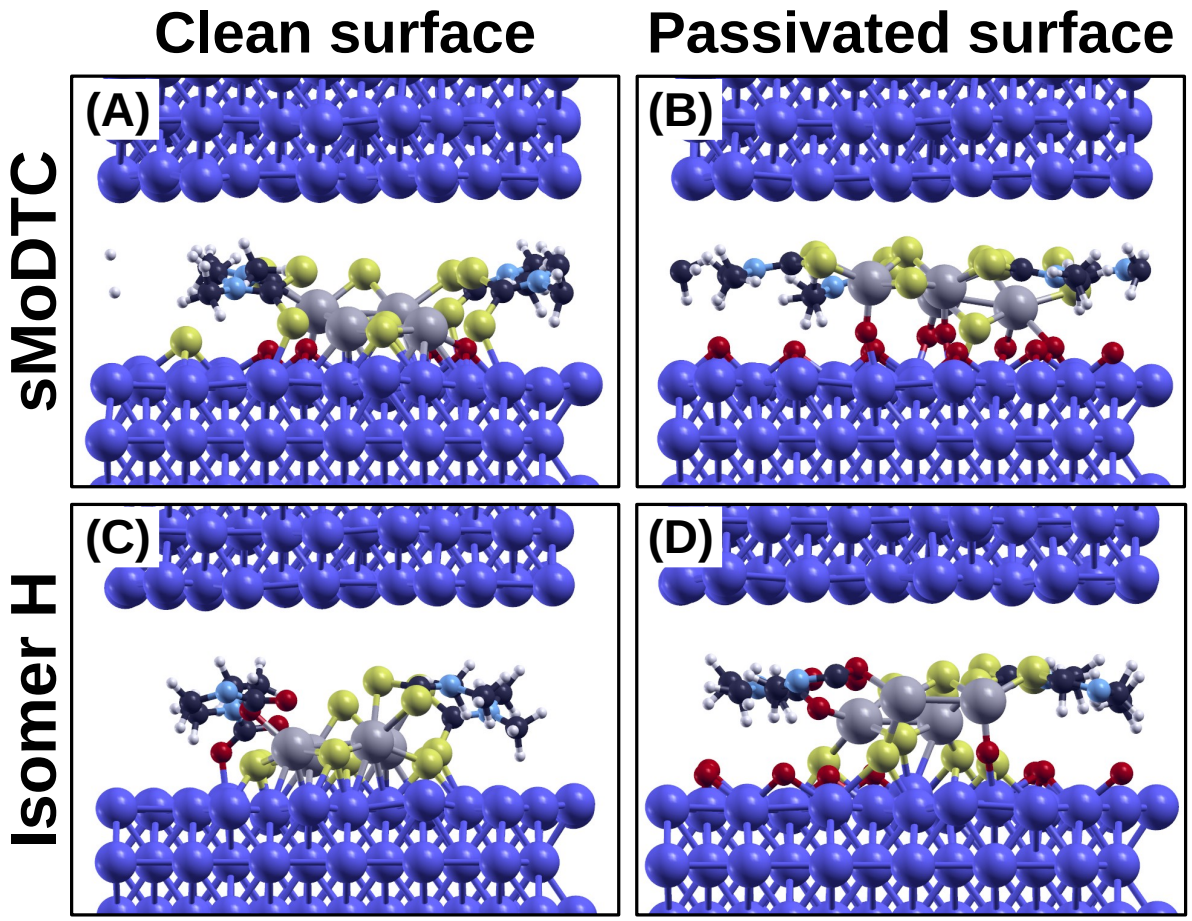


Figure 4.7: Lateral views of the QM/MM systems after 2 ps of the simulation.

experimental observations. The adsorption of the MoDTC structures is limited by the presence of the oxygen atoms in all of our calculations. Low durability of the MoS_2 tribolayer can be expected due to such a limited adsorption of the additives, when the surface is rich in oxygen. Even though the low MoDTC concentrations we considered in the simulation cells do not allow the formation of complete tribolayers, the formation of MoS_2 can be expected in all cases, provided that a sufficient amount of molecules is present at the contact. The MoS_2 layer can be strongly bound to the surface in the case of bare steel, whereas the MoDTC compounds should cluster and recombine while being only weakly adsorbed in the case of the oxidized surface.

4.4 Conclusions

Based on the results obtained by means of tribological experiments and ab-initio simulations, we showed that the oxidation of the metallic surface hinders the tribochemical reactivity of MoDTC lubricant additives both in static and tribological conditions. Direct comparison between the simulations and the real tribological interface is, in general, a formidable task and searching an exact match between the conditions of the two approaches lies beyond the purpose of this work. However, the tribological tests carried out on the mirror polished steel discs and the results offered by the simulations matched. An increased amount of oxygen on the surface of the mirror polished steel discs showcased increased friction in the initial phase of the tribological tests, meaning that the functionality of the MoDTC lubricant additives was inefficient, and resulted in a much longer run-in period. The increased friction in the case of the oxidized surface induced harder tribological conditions on the additives and possibly higher levels of oxidation of MoDTC. We showed in a previous publication that this phenomenon can favor the release of molecular units ready to build MoS_2, leading to an even lower friction coefficient in the end. The static and dynamic (QM/MM) ab initio simulations demonstrated in fact that the presence oxygen as a passivating species limits the possibility of MoDTC to access the catalytic sites of the metal, reducing its capability to dissociate at the beginning of the sliding.

Chapter 5

Experimental and Ab-Initio Characterization of Mononuclear Molybdenum Dithiocarbamates in Lubricant Mixtures

5.1 Introduction

Friction is an unavoidable phenomenon which results in massive economic and environmental costs [2]. The search for innovative solutions in tribology pushes the scientific community to design lubricant additives which are more efficient in reducing friction than the currently employed ones while limiting their negative effects for the environment by decreasing their concentration in the formulations. This difficult task requires a complete understanding of the mechanism of action of the currently employed lubricant additives, which are often involved in very complex reactivity [93, 158].

Molybdenum dithiocarbamates (MoDTCs) are a family of different chemical compounds widely used as friction modifiers in the automotive industry. Organo-moybdenum compounds, in fact, are among the most successful lubricant additives in the boundary lubrication regime, where the asperity contact between steel surfaces generates extreme conditions in the tribological systems [3, 101, 102]. At these contacts, MoDTC breaks down due to the interaction with the substrate and the high local temperatures and pressures. The molecular fragments resulting from the dissociation can be reorganized into molybdenum disulfide (MoS_2), which is a remarkable solid lubricant, under the effect of the mechanical stresses. MoS_2 is a layered material and its mechanism of function consists in weak interlayer forces that offer very small resistance to sliding, offering protection for the metallic surfaces in relative motion [118].

The synergistic interaction of MoDTC structures with ZnDTP, common anti-wear additives, are well established in literature [120, 165, 166]. In fact, MoDTC can easily oxidize when exposed to air. The new oxygen atoms can substitute the sulfur atoms present in the molecules in different positions, especially in the ligand position [123, 167], leading to a wide variety of similar chemical structures. However, oxidation is not the only source of complexity in this family of compounds, as structures with one or three Mo atoms have also been reported [124]. While most of the scientific literature focuses on the dimeric structures of MoDTC, mononuclear structures can also play a role in commercial formulations. These alternative structures of MoDTC could be the result of chemical equilibria inside the mixture and it is highly desirable to better understand the origin and the mechanism of action of these compounds.

In this study we characterized by means of experiments and ab-initio simulations the mononuclear MoDTC compound. First, we collected evidence on the presence of mononuclear MoDTC in a commercial sample, separated in fractions by flash chromatography. The most relevant fractions were then characterized by electronic spectroscopy and mass spectrometry. Tribological experiments were performed to investigate the friction reduction performance of the different fractions compared to the commercial product. To better understand the properties of mononuclear MoDTC, we carried out static density functional theory (DFT) calculations to evaluate geometric and electronic properties of mononuclear MoDTC for the first

Table 5.1: Program for the separation of S525 with flash chromatography. The arrows in the Table indicate the initial and final times and compositions of the eluting solvent. Steps 1 and 4 are isocratic.

Step	Time (min)	%A	%B	%C	%D
1	$0 \rightarrow 10$	100	0	0	0
2	$10 \rightarrow 25$	$100 \rightarrow 0$	$0 \rightarrow 100$	0	0
3	$25 \rightarrow 33$	0	$100 \rightarrow 50$	$0 \rightarrow 50$	0
4	$33 \rightarrow 45$	0	0	0	100

time, estimate the strength of its bonds, study its interaction with metallic substrates and its possible decomposition mechanism on iron. All the results obtained for the mononuclear compounds are compared to the previous observations derived for the binuclear compounds, in an attempt to shed light on the intricate functionality of these lubricant additives.

5.2 Methods

5.2.1 Experimental techniques

MoDTC is commercially available in mixtures where similar chemical structures can be present at the same time. MoDTC molecules may have different alkyl chain lengths, degrees of oxidation, number of Mo atoms [123, 124]. Sakuralube 525 (S525) was chosen for this work because of its industrial relevance. It consists of a mixture of MoDTC structures, dissolved in base oil, with eight- and thirteen-membered lateral chains in their dithiocarbamate units. The separation of S525 was performed by means of flash chromatography. A sample containing 1 g of S525 in 4 mL of cyclohexane was injected on the head of a GRACE Reveleris HP Silica 20 μm cartridge, previously conditioned with cyclohexane. A VWR International LaFlash chromatograph, coupled with a Gilson FC204 fraction collector, was employed for the separation. The eluted species were detected by measuring their ultraviolet (UV) absorption at 254 nm. Table 5.1 summarizes the program of the separation, where the eluting solvents A, B, C and D corresponded to cyclohexane, dichloromethane, ethyl acetate and 2-propanol, respectively. The flow rate was 20 mL/min for the whole duration of the separation. The fractions were collected from minute 10 of the run and each vial contained 25 mL of liquid. For the subsequent characterization, the solvent of the seventh, eighth and ninth collected fractions was evaporated overnight under a flux of nitrogen, as they were the main fractions, with the highest concentration in molybdenum. A portion of the solid obtained was dissolved in isooctane to record electronic spectra on a VARIAN Cary 300 BIO UV/visible spectrophotometer, while the remaining sample was dissolved in mineral Group III oil with a kinematic viscosity of 4 cSt at 100°C. X-ray fluorescence (XRF) and mass spectrometry were also employed to measure the concentrations of molybdenum and sulfur and to identify the most relevant species in the fractions, respectively, as shown in Appendix D.

Tribological tests were carried out on polished AISI 52100 hardened steel discs by employing Fractions 7, 8 and 9 as lubricants, with a molybdenum concentration of 50 ppm. S525 dissolved in Yubase 4, with the same molybdenum concentration, was chosen as a reference lubricant. All the lubricants were deposited directly on the discs immediately before the run. An Anton Paar MCR302 Rheometer equipped with a tribometer assembly (T-PID/44 three balls on disk measurement cell). The rotation speed increased from 4.7 mm/s to 377 mm/s over 750 s, with a total test duration of 20 minutes. The temperature of the system

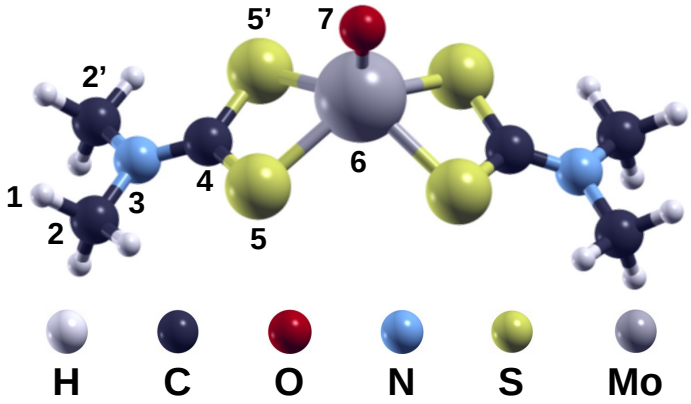


Figure 5.1: Molecular structure of mononuclear MoDTC.

was 110°C and the contact pressure was 700 MPa.

5.2.2 Computational techniques

In the samples containing S525 studied experimentally, mononuclear MoDTC was detected, as explained in the following Section. Therefore, we considered the mononuclear chemical structure shown in Figure 5.1 for our computational study. In this structure, a single Mo atom is coordinated by an oxide and two dithiocarbamate units. We considered methyl groups as lateral chains in the dithiocarbamate units, which are shorter than the ones in the experimental samples, to alleviate the computational cost. Such an approximation was already justified in our previous publication regarding binuclear MoDTC compounds [167]. We characterized the properties of mMoDTC by means of static calculations in the DFT framework implemented in the Quantum ESPRESSO package [128].

The DFT calculations were carried out by following the pseudopotentials/plane waves approach, with periodic boundary conditions applied to the supercells. The Perdew-Burke-Ernzerhof (PBE) functional [127] was adopted to describe electronic exchange and correlation. To evaluate the properties of isolated mMoDTC and its fragmentation energy, we decided to truncate the plane waves expansion by selecting cutoffs of 40 and 320 Ry for the wave functions and for the charge density, respectively, as the pseudopotentials employed in this work were ultrasoft. For all the calculations, the integrations of the charge density were carried out at the gamma point. Spin polarization was taken into account in order to allow the spin multiplicity of the different chemical species to vary. A Gaussian smearing of 0.02 Ry was added to better describe the occupations of the electronic states around the Fermi level. The geometry optimizations were stopped when the total energies and the forces on the atoms converged below the thresholds of 1×10^{-4} Ry and 1×10^{-3} Ry/bohr, respectively.

For part of the calculations on the fragmentation of isolated mMoDTC, the Gaussian 09 software [134] was used. The basis set used for these calculations was def2-TZVP [132, 133] and all the computational parameters were already described in a previous publication [167].

For the isolated chemical structures a cubic supercell with an edge of 60 bohr units was chosen to avoid interactions with the periodic replicas. The Avogadro 1.2.0 software [130, 131] was employed to generate an initial guess for the geometry of the chemical structure, which was then optimized without imposing any symmetry constraint.

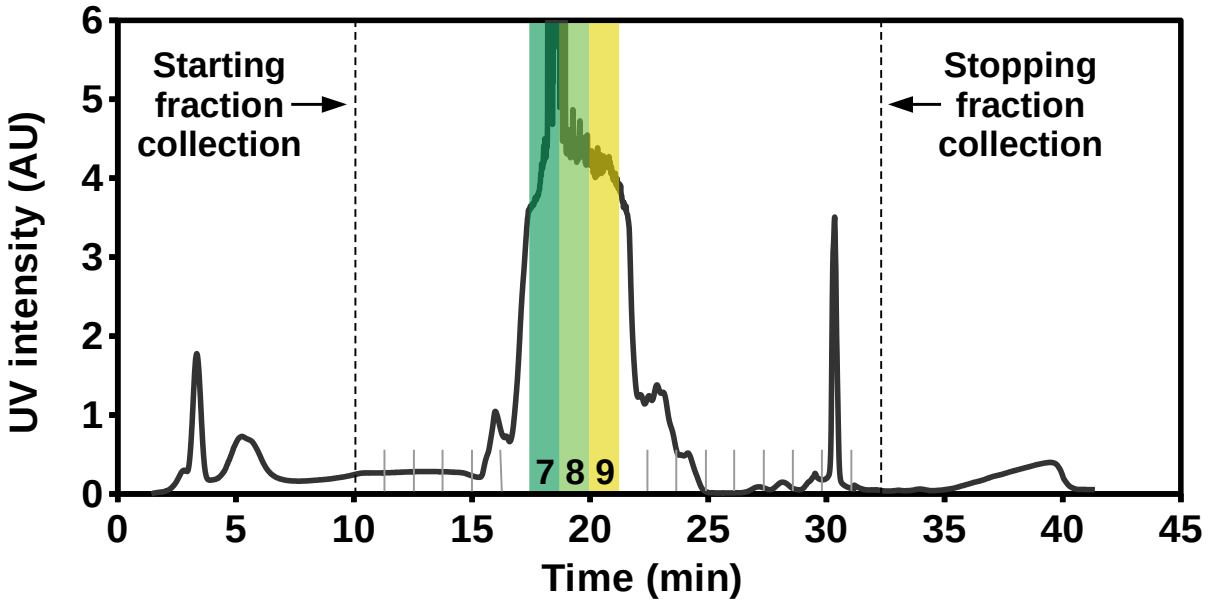


Figure 5.2: Chromatogram of the flash separation of S525. The collected fractions are marked on the bottom of the plot, with Fractions 7, 8 and 9 highlighted with their corresponding color.

To simulate the interactions of the lubricant with a metallic substrate, Fe(110) was considered, as it is the most favorable surface of this metal [146, 182]. For the calculations including the iron slabs, the cutoffs for the kinetic energy of the wave functions and for the charge density were lowered to 30 and 240 Ry, respectively, for the reasons explained in our previous work.[175] Static calculations with mMoDTC and its fragments on the iron slabs were carried out in $8 \times 2\sqrt{2}$ supercells, in the units of the lattice parameter of bulk iron. In this case, the iron slabs were composed by four atomic layers.

5.3 Results

5.3.1 Separation of S525 and characterization of the collected fractions

Figure 5.2 shows the chromatogram of the separation of S525. The products obtained during the run can be grouped in four parts, ordered by increasing polarity, which were eluted in the respective steps of the run:

1. Before 10 minutes: base oil
2. Between 15 and 25 minutes: majority of MoDTC compounds
3. Between 25 and 33 minutes: few polar MoDTC compounds
4. After 35 minutes: degradation products of MoDTC

Infrared (IR) spectra confirmed the absence of MoDTC compounds in the fractions eluted before 10 minutes and their presence in the peaks between 15 and 33 minutes of the run. The IR band belonging to

the diagnostic Mo=O vibration between 900 and 1000 cm^{-1} [102, 167] was detected also in the last fraction after 35 minutes. However, due to the large amount of impurities in the last fraction and the complete lack of MoDTC compounds in the first fractions, we collected only the fractions belonging to the two central groups of peaks, between 10 and 33 minutes, discarding the rest of the elution. The collected fractions contained mixtures of several MoDTC compounds which were difficult to purify with such a protocol, due to their very similar chemistry. Among the fractions collected from the main group between 15 and 25 minutes, we focused our attention on Fractions 7, 8 and 9, as they were the most concentrated ones and they showcased a color transition from green to yellow, as indicated in Figure 5.2. Electronic spectra of these fractions are included in Appendix D.

5.3.2 Characterization and tribological test of the collected fractions

Figure 5.3 shows the mass spectra of Fractions 7, 8 and 9 and a comparison between the theoretical spectrum of mMoDTC and a close-up of the spectrum of Fraction 8.

The MoDTC compounds detected by mass spectrometry are the mononuclear compounds at around 746.3 m/z (green overlay) and the binuclear compounds at around 924-945 m/z (orange overlay). The rest of the highlighted compounds correspond to impurities such as secondary and tertiary amines, alkyl thiourea and, at higher m/z, salts and aggregates of several MoDTC compounds. The bottom panel of Figure 5.3 demonstrates the presence of mononuclear MoDTC in Fractions 7 and 8, as the theoretical spectrum of mMoDTC ($MoOS_4N_2C_{34}H_{68}$) and the corresponding region of Fraction 8 perfectly match.

The ratio between mononuclear and binuclear MoDTC varies among the different collected fractions. The approximate mononuclear/binuclear ratio in Fractions 7, 8 and 9 are 0.26, 0.5 and 0, respectively, meaning that the richest fraction in terms of mononuclear MoDTC is Fraction 8. The separation protocol could be further optimized to obtain even better separations of the different MoDTC compounds. However, flash chromatography allowed us to collect chemically different MoDTC samples already after a single run. These fractions contained mononuclear MoDTC compounds, which can be present as byproducts in the lubricant mixtures based on MoDTC, although they have never been characterized nor compared to the binuclear compounds concerning their tribochemical properties. Mass spectra of Fractions 7, 8 and 9 are shown in Appendix D.

Figure 5.4 shows the results of the tribological tests where Fractions 7, 8 and 9 and a reference mixture of S525 were employed as lubricants. Overall, the best tribological performance was provided by the full mixture of MoDTC structures. In the case of the reference lubricant, in fact, the friction coefficient remains at the lowest levels both before and after the tribochemical activation of the additives to form MoS_2, which occurs around 700 s. Fractions 7 and 9, which contain the least amount of mononuclear structures, provide an initial increase in friction, probably caused by high severity at the contact. However, the two systems are able to eventually reach low friction, with values comparable to the ones observed with S525. Surprisingly, Fraction 8, which contains the highest amount of mononuclear structures, initially follows the same profile as the reference lubricant, although the activation of the friction reduction additives does not occur during the test. It should be noted that a variety of MoDTC structures is present at the same time in all the considered fractions. However, these compounds appear to play a synergistic role when they are combined into S525, as the different structures have specific impacts on the tribological behavior of the lubricant, while their friction reduction performance is limited when the original mixture is fractioned.

To better understand the role of mononuclear MoDTC in lubricant mixtures, compared to binuclear structures, we focused our computational investigation on the mononuclear structure called mMoDTC.

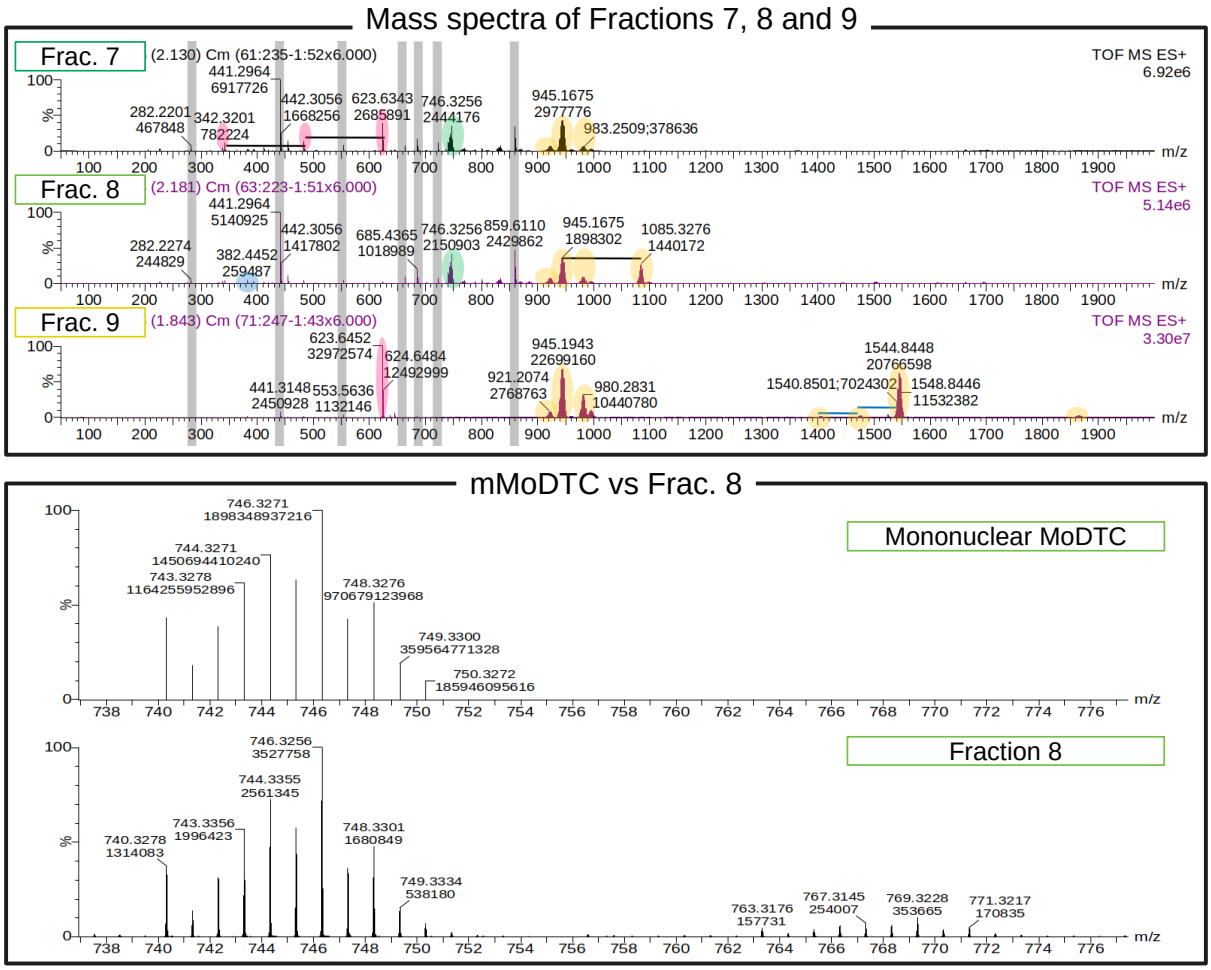


Figure 5.3: Top panel: mass spectra of Fractions 7, 8 and 9. Different families of compound are grouped by color. Bottom panel: comparison between the theoretical spectrum of mononuclear MoDTC and the corresponding region in the spectrum of Fraction 8.

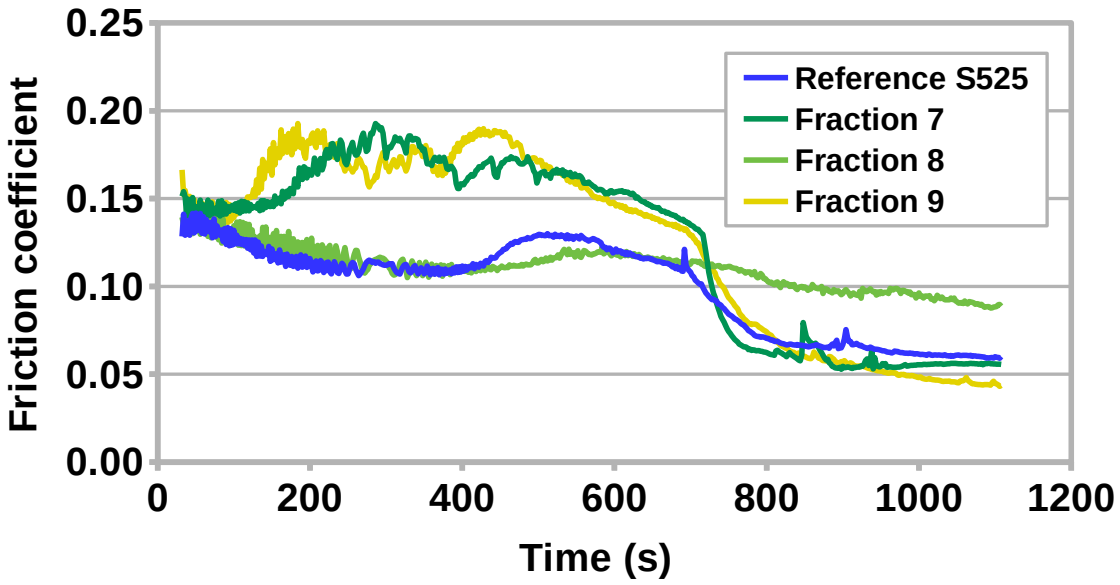


Figure 5.4: Tribological test (bottom) of the considered fractions and the reference mixture.

5.3.3 Calculated molecular properties

The mMoDTC complex is a monopositive cation, as the central Mo atom has an oxidation number of +5 while the electrons involved in the coordination account for only four bonds. Possible counterions are dialkyl dithiocarbamates (DTCs) or their dimers, called bis-DTCs, although complex ionic structures based on MoDTC have not been described yet in the literature. Therefore, we started our computational investigation by calculating the ionization energy E_I of mMoDTC and compared it to the corresponding energy of the dimeric structure of MoDTC, which we called sMoDTC in our previous publications. The calculated values for E_I, simply obtained by subtracting the total energies of the neutral complexes from the structures with one missing electron, turned out to be 5.3 and 6.2 eV for mMoDTC and sMoDTC, respectively, making the mononuclear compounds easier to ionize than the binuclear compounds. However, the calculated absolute values for the ionization energies are merely representative, due to the well-known fundamental gap problem in DFT [183].

In the following, we focused our attention mostly on the cationic form of mMoDTC, although the neutral form, with an oxidation number of +4 on the Mo atom, was also taken into account for comparative purposes. The mMoDTC cation is a radical, as a single non-bonding electron is left on the Mo atom. Such unpaired electron is hosted in a singly-occupied molecular orbital (SOMO), shown in the top-left panel of Figure 5.5, along with the highest fully occupied molecular orbital (SOMO-1) and the lowest unoccupied molecular orbital (LUMO). The SOMO is the result of a combination of atomic orbitals in which three $4d$ orbitals of molybdenum account for more than 70% of the molecular wave function. All the contributions above 5% determining the SOMO-1 come from $3p$ orbitals of the S atoms, while more than 65% of the LUMO is determined by one $2p$ orbital of oxygen and two $4d$ orbitals of molybdenum. The shape of the SOMO, in combination with the spin polarization plot shown in the bottom-left panel of Figure 5.5, reveals

that the unpaired electron, characterized by a negative spin, is mainly localized on the Mo atom. The densities of states (DOSes) of the cationic and the neutral forms of mMoDTC, shown in the top-right panel of Figure 5.5, differ because the missing electron in the cation induces a slight rearrangement of the nuclei, which, in turn, leads to an energy shift and a change in the density of the electronic states. The SOMO-LUMO gap calculated for the cation is approximately 1.42 eV, while for the neutral complex the HOMO-LUMO gap is approximately 1.59 eV, compared to 2.72 eV, as in the case of sMoDTC. To better visualize the asymmetry in the DOSes occupied by electrons with different spin, the DOS of cationic mMoDTC can be decomposed in the contributions of the spin up and down electrons, as shown in the bottom-right panel of Figure 5.5, which demonstrates the increased amount of occupied states for electrons with spin down in proximity of the Fermi energy.

To summarize, the monomer is easier to ionize than the dimer. In tribological conditions, electron transfer among chemical species could occur because of the high energies generated by mechanical stresses acting on the system. When cationic mMoDTC is formed, it can quickly react with other species present in the mixture, because of the radical electron localized on the central metallic unit. The different electronic properties of mMoDTC and its capability to bind to other MoDTC structures can explain the different color of the samples containing the monomer with respect to samples containing only the dimeric structures.

The bond lengths and angles of mMoDTC obtained from geometry optimization turned out to be similar to the corresponding values in sMoDTC, with the discrepancies in the bonds and the angles laying below 2% and 7% in absolute value, respectively. The complete analysis on the structural data is reported in Table 5.2.

Table 5.2: Lengths and angles of selected bonds of cationic and neutral mMoDTC. The numbers in brackets follow the numbering proposed in Figure 5.1

Bond	Length (Å)		Angle	Size (°)	
	cationic	neutral		cationic	neutral
H(1)-C(2)	1.10	1.10	C(2)-N(3)-C(2')	115	116
C(2)-N(3)	1.46	1.46	C(2)-N(3)-C(4)	123	122
N(3)-C(4)	1.32	1.34	N(3)-C(4)-S(5)	123	124
C(4)-S(5)	1.73	1.73	S(5)-C(4)-S(5')	113	111
S(5)-Mo(6)	2.44	2.44	C(4)-S(5)-Mo(6)	87	89
Mo(6)-O(7)	1.69	1.70	S(5)-Mo(6)-O(7)	111	109

5.3.4 Fragmentation of isolated mMoDTC

By following the same computational approach employed in our previous publication [167], we estimated the C-S and S-Mo bond strengths in mMoDTC in order to understand which is the most probable dissociative pattern. We calculated the fragmentation energies ΔE_{frag} in the following way:

$$\Delta E_{\text{frag}} = E_{\text{frag1}} + E_{\text{frag2}} - E_{\text{mMoDTC}} \tag{5.1}$$

where E_{frag1}, E_{frag2} and E_{mMoDTC} are the total energies of the two molecular fragments originated by the dissociation of mMoDTC and the whole complex, respectively. The geometry of the fragments was kept frozen to prevent any spatial rearrangement of the atoms that could influence the energy values. The

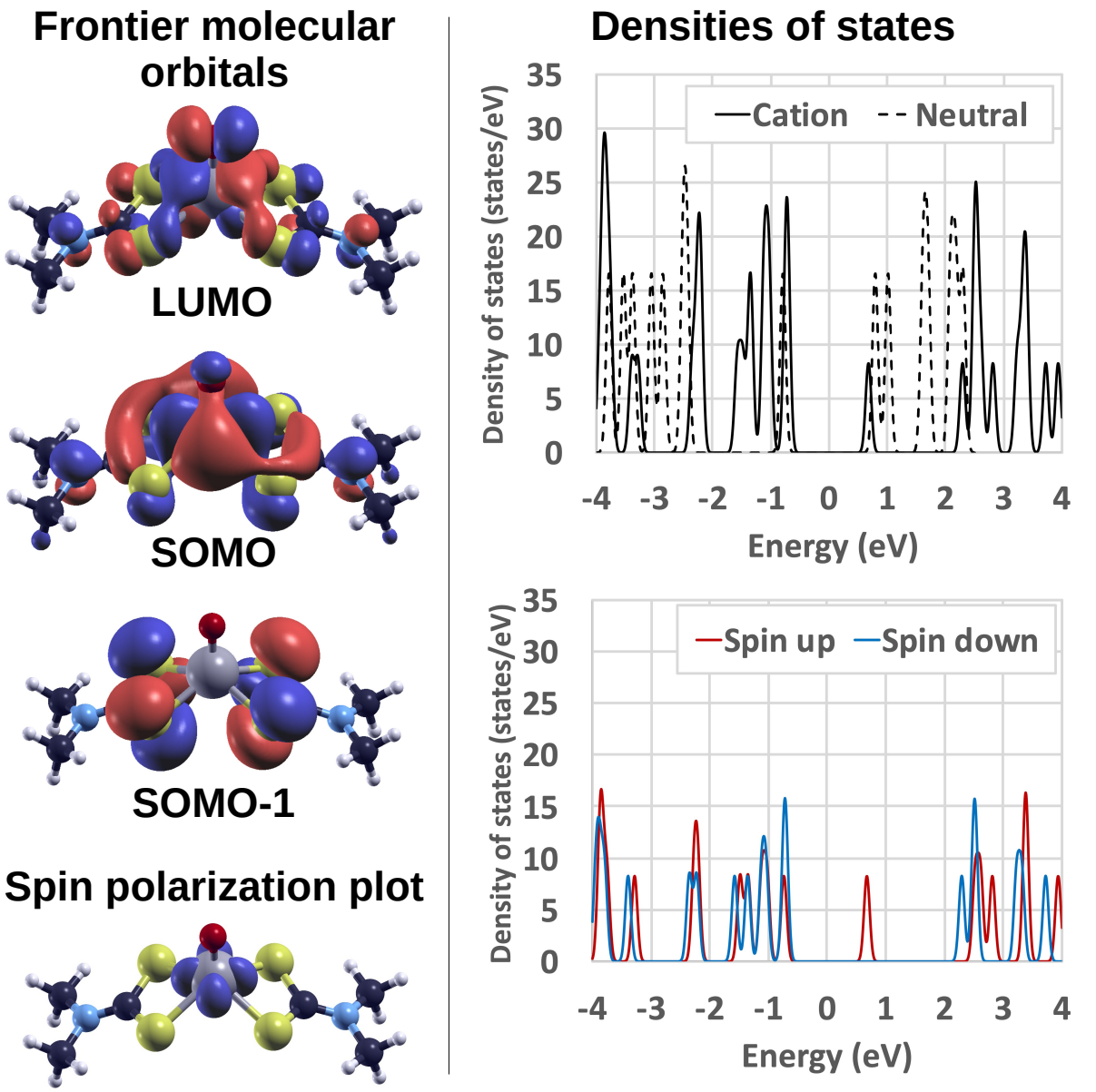


Figure 5.5: Electronic properties of mMoDTC. Top left: frontier molecular orbitals of the mMoDTC cation. The isovalue for all the plotted orbitals is 0.002. The red and blue colors of the isosurfaces represent the positive and negative sign, respectively, of the electronic wave function. Bottom left: spin polarization plot, where the blue coloring of the isosurface around the Mo atom indicates an excess of negative spin. The isovalue for this plot is 0.01. Top right: densities of states (DOSes) for cationic (solid line) and neutral (dashed line) mMoDTC. Bottom right: densities of spin up (red) and spin down (blue) states in cationic mMoDTC. The DOSes were shifted in order to set the Fermi energy to zero in all the plots.

atoms with a broken bond were not passivated by other species and spin polarization was considered to allow the electronic configurations to reach spin multiplicities higher than singlets. We took into account three different ways of dividing the complex: Cut 1 corresponds to the homolytic breaking of the two S-Mo bonds, while Cut 3 to the breaking of the two C-S bonds, proposed in the dissociative mechanisms by Grossiord et al. [101] and by Khaemba et al. [102], respectively. Cut 2 is the intermediate pattern in which one S-Mo bond and one C-S bond are broken. A schematic representation of these fragmentation patterns is presented in Figure 5.6. The electronic configuration of the fragments of the cationic form of mMoDTC was left free to reach the minimum energy state, which corresponds to the lowest spin multiplicity (doublets). The absolute values of fragmentation energies are summarized in Table 5.3. The calculations revealed that the most favorable destination for the positive charge after the dissociation is the central metallic unit. Cut 1 turned out to be the most favorable dissociation pattern, as in the case of the dimeric structure, as it required 0.5 and 2.3 eV less than Cut 2 and Cut 3, respectively. By carrying out the same investigation on the neutral form of mMoDTC, we found out that describing the molecular fragments as doublets was insufficient to estimate the strength of the broken bonds. In fact, Cut 2 appears to be the most favorable fragmentation for the neutral compound. Cut 2 corresponds to an intermediate situation between Cut 1 and Cut 3, and its fragmentation energy should also lie between the energies of the other two patterns. A more appropriate way of estimating the strength of the bonds in mMoDTC would be to consider the fragments as quartets, which better describe the electronic configuration obtained by the homolytic dissociation of the complex. We compared the fragmentation energies of neutral mMoDTC by considering the spin multiplicities of doublets and quartets with different approaches. The first of the three columns for each spin multiplicity in Table 5.4 reports the fragmentation energies calculated by Quantum Espresso by using the PBE [184] approximation, while the second and the third columns report the same values calculated with Gaussian 09 using the PBE and the PBE0 [184] approximations, respectively. While PBE0 in Gaussian is able to reproduce the same trend seen with Quantum Espresso, it turns out that the correct energy trends are recovered when the fragments are considered as quartets. In this case, the most favorable fragmentation is confirmed to be Cut 1, in analogy with the MoDTC dimer.

Table 5.3: Fragmentation energies of isolated mMoDTC and sMoDTC, expressed in eV. In the first and the second column, energy values are reported for the cationic and the neutral forms of mMoDTC, while in the last column the energy values for the binuclear structure sMoDTC are taken from Ref. [167].

	Cationic mMoDTC	Neutral mMoDTC	sMoDTC
Cut 1	4.8	4.8	4.1
Cut 2	5.3	4.0	4.6
Cut 3	7.1	5.5	6.7

5.3.5 Chemisorption and fragmentation on iron

Figure 5.7 shows the optimized configuration for the adsorption of mMoDTC on the clean and passivated Fe(110) surface. These orientations of the complexes on the substrates might not be the absolute minimum configurations, yet they offer a clear qualitative description of the differences in the adsorption on the clean and the passivated surfaces. The passivation of iron is achieved by 0.25 monolayers of oxygen atoms put in the threefold coordination site of the metal, as it is the most favorable configuration for this element

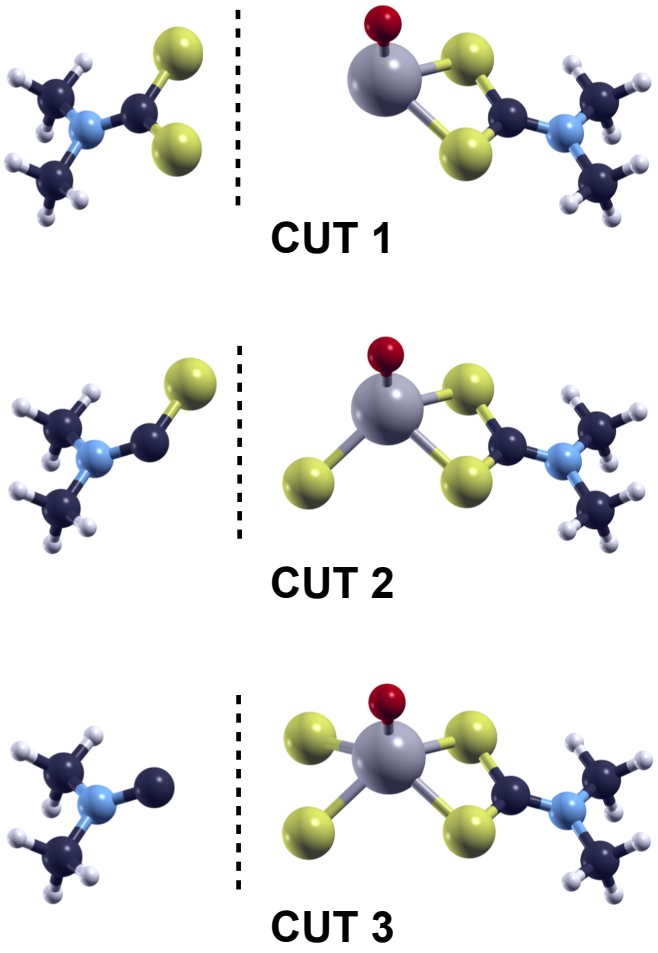


Figure 5.6: Schematic representation of the dissociation patterns of mMoDTC.

Table 5.4: Fragmentation energies of neutral mMoDTC, expressed in eV, calculated with different techniques and compared by different spin multiplicities of the fragments.

	Doublets			Quartets		
	PBE (QE)	PBE (G09)	PBE0 (G09)	PBE (QE)	PBE (G09)	PBE0 (G09)
Cut 1	4.8	5.5	5.5	8.1	8.5	8.5
Cut 2	4.0	4.4	4.0	8.6	8.7	8.8
Cut 3	5.5	6.1	5.6	9.6	9.8	9.7

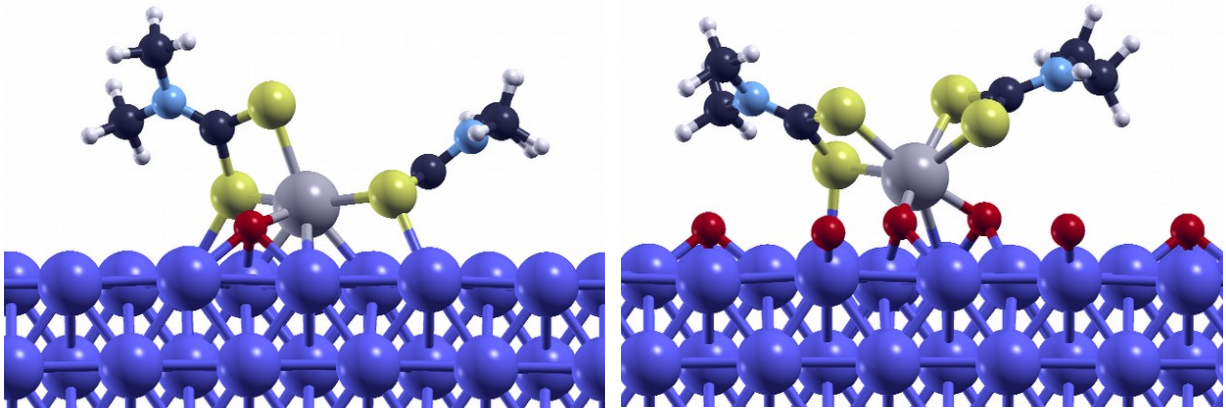


Figure 5.7: Optimized configuration for mMoDTC adsorbed on the clean (left) and oxygen-passivated (right) iron (110) surfaces.

on iron [180]. Both the cationic and the neutral form of mMoDTC are chemically bound to the surface through the central unit. The passivation weakens the chemisorption, as less atoms of the complex are able to bind to the free sites of iron. This is reflected upon the adsorption energies of the complex, calculated as:

$$E_{\text{ads}} = E^{Fe}_{\text{mMoDTC}} - E_{\text{mMoDTC}} - E_{\text{iron}} \tag{5.2}$$

where E^{Fe}_{mMoDTC} and E_{iron} are the total energies of the chemisorbed complex on the substrate and of the iron slab alone, respectively. The adsorption energies of cationic mMoDTC turned out to be -11.4 and -9.7 eV in the case of the clean and the passivated surface, respectively. Such favorable values of energy for the chemisorption are due to the stabilization effect of the positive charge of the complex interacting with the metallic substrate. In particular, a Bader charge analysis [151–154] revealed that the positive charge is completely redistributed only on the topmost iron layer, which is the closest to the complex, with almost no effect on the underlying layers. The absence of the positive charge, in fact, leads to adsorption energies of -3.2 and -1.4 eV for the clean and the passivated surfaces, respectively.

We additionally verified what is the most favorable fragmentation pattern for the complexes adsorbed on iron. For this purpose, we optimized the geometry of the fragments of mMoDTC on iron, in analogy to the investigation carried out for the dimeric complex [175], and we calculated the dissociation energies as:

$$\Delta E^{Fe}_{\text{frag}} = \frac{1}{2}\left(2E^{Fe}_{\text{ligand}} + E^{Fe}_{\text{central}} - E^{Fe}_{\text{mMoDTC}} - 2E_{\text{iron}}\right) \tag{5.3}$$

where E^{Fe}_{frag1} and E^{Fe}_{frag2} are the total energies of the lateral ligands and the central units of mMoDTC adsorbed on iron, respectively. Cuts 1 and 3 were the dissociative patterns considered to generate the molecular fragments adsorbed on iron. The most favorable fragmentation for the complex on the substrate turned out to be Cut 3 with a favorable fragmentation energy of -2.2 eV, compared to an unfavorable value of 0.2 eV for Cut 1. This result is in contrast with the case of the isolated compound. We observed that this phenomenon occurs also for the dimeric MoDTC structures and complexes with a similar structure [citare]. This phenomenon is due to the capability of the metallic substrate to stabilize more efficiently the fragments originated by separating the complexes between the chalcogen atoms and the carbon atom of the ligand unit. Mononuclear MoDTC compounds follow the general rules derived for these small organometallic complexes:

- While the fragmentation of isolated complexes is not favorable, the metallic substrate is able to stabilize the molecular fragments and the dissociation energies become favorable.
- The complexes on the metallic substrates can follow alternative dissociative patterns, in which the weakest bonds are not the first ones to be broken. It is more probable to break the molecules between the carbon atom and the chalcogen atoms of the ligand unit.

The fragmentation energies obtained from Eq. 5.3 actually correspond to the average of the two values corresponding to the dissociation of the two ligand units, one after the other. A more precise estimation would require to calculate the dissociation energies for each step of the reaction. We carried out these calculations for both cationic and neutral mMoDTC, with the results summarized in Table 5.5. Figure 5.8 shows all the fragments originated by the individual steps of the dissociation. Additional adsorption configuration could be possible for the molecular fragments on iron than the ones presented in the figure. However, the complete screening of all the possible adsorption geometries of these fragments goes beyond the purpose of this work. These adsorption configurations were chosen to merely show that the dissociation mechanism of these compounds on iron is a complex multi-step reaction. It turns out that the first dissociative step is always more favorable than the second dissociation step. By comparing the dissociation energies of mMoDTC and sMoDTC, the values for Cut 3 are essentially similar, while for Cut 1, mMoDTC is much harder to break. Moreover, the dissociation energies of the neutral compound are generally lower, hence more favorable, than the ones of the cation. This is due to the strong chemisorption of the cationic compound induced by the strong reactivity of the metallic core hosting a radical electron. Such electronic configuration makes the mMoDTC cation stickier than the neutral compound, and the stronger binding between the complex and the substrate can hinder the subsequent dissociative steps which can be useful to form the desired MoS_2 clusters. These features can be an explanation for the behavior observed in the tribological tests. In fact, the fraction which is the richest in mononuclear MoDTC presents slower kinetics in the activation to form MoS_2. An unbalance between monomeric and dimeric structures of MoDTC in oil mixtures limits the friction reduction performances of the lubricants, as MoS_2 needs to be generated continuously during sliding.

Finally, in order to better understand whether the central units of mMoDTC adsorbed on iron are more stable than the central units of sMoDTC in the same conditions, we considered an ideal chemical reaction where two central units of mMoDTC iron combine into one central unit of sMoDTC and release two sulfur atoms on the iron surface. The energy exchanged in this reaction can be written as:

$$\Delta E_{\text{r}} = E^{Fe}_{\text{Mo}_2\text{O}_2\text{S}_6} - 2E^{Fe}_{\text{MoOS}_4} + 2E^{Fe}_{\text{S}} - E_{\text{iron}} \tag{5.4}$$

Table 5.5: Fragmentation energies of cationic and neutral mMoDTC, expressed in eV, for each individual step of the dissociation.

	Cationic		Neutral	
	Cut 1	Cut 3	Cut 1	Cut 3
First detachment	-0.1	-3.0	-0.4	-3.4
Second detachment	0.4	-1.4	-0.1	-1.7
Total	0.3	-4.3	-0.5	-5.0

where $E^{Fe}_{Mo_2O_2S_6}$, $E^{Fe}_{MoOS_4}$ and E^{Fe}_{S} are the total energies of the central units of sMoDTC and mMoDTC and of an S atom adsorbed on iron, respectively. The reaction energy turned out to be -0.53 eV, meaning that a single central unit of the binuclear compound and two sulfur atoms adsorbed on iron are more stable than two central units of the mononuclear compound. This suggests that central units obtained from mMoDTC could recombine into binuclear cores on the iron substrates, becoming more similar to MoS_2 in terms of stoichiometry, in combination with the release of two S atoms. After providing enough energy in the system to cause the dissociation of mMoDTC, the central units of the complex near each other have the possibility to assemble into wider structures, which is an advantage for the formation of MoS_2. On the other hand, starting to build a MoS_2 tribolayer from the dimeric MoDTC structures can be more beneficial, as the central units of the dimers require one recombination step less than the monomers.

5.4 Conclusions

In this work, we described the properties of one of the components of lubricant mixtures containing MoDTC: the mononuclear structure called mMoDTC. Mononuclear structures are, in fact, a group of MoDTC compounds present in the lubricants along with the binuclear compounds. For the first time, we were able to separate chemically different fractions from the MoDTC-containing lubricant S525 and to characterize such fractions by means of XRF, MS, UV/Vis spectroscopy and tribology tests. These fractions turned out to be different in terms of composition, elemental concentration of molybdenum and sulfur, electronic absorption and tribological performance. In particular, fractions containing a larger amount of mononuclear MoDTC showcase a green color instead of yellow and they present slower kinetics in the formation of the MoS_2 tribolayers. To shed light on these aspects, we calculated the electronic and structural properties of mMoDTC, which are similar to the ones of the dimeric structures. However, the lower ionization energy and fundamental gap make the monomer a reactive compound that can quickly interact with other chemical species present in the mixtures. A consequence of this enhanced reactivity is that the chemisorption to the metallic substrate is stronger than in the case of the dimer. This is reflected upon the higher dissociation energies of Cut 1 compared to the corresponding values of the dimer, while the dissociation energies of Cut 3 are very similar between the two complexes. The fact that mMoDTC can easily interact with other chemical species through the unpaired electron could be seen as a drawback for the lubricant oil, as undesired chemical species can be formed in tribological conditions, slowing down the kinetics to form MoS_2. However, some features of the mononuclear compound are still beneficial in the friction performance of the lubricant mixture, namely the strong interaction of mMoDTC with the metallic substrate, its dissociation mechanism, which is essentially the same compared to the one of sMoDTC, and the fact the central core units obtained after dissociation can recombine into larger units. The combination of experimental and

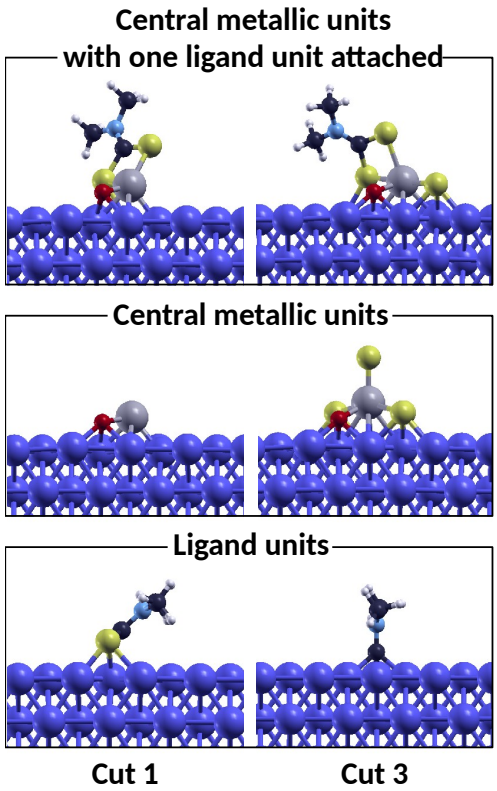


Figure 5.8: Fragments of mMoDTC originated by each individual step of the dissociation of the ligand units: central metallic units with one ligand unit attached, central metallic units alone and ligand units alone obtained from Cut 1 and 3, respectively.

computational investigations showed that only a good balance between the different MoDTC structures ensures the low-friction performances of the lubricant, because the mononuclear and binuclear compounds have different roles to play during sliding.

Chapter 6

Adsorption and Dissociation of $Ni(acac)_2$ on Iron by Ab Initio Calculations

6.1 Introduction

Metal β-diketonates are a class of metallorganic compounds widely employed as chemical precursors for their volatility, rich reactivity and commercial availability. Because of their catalytic properties, these compounds are ideal for several applications [185]. In fact, nickel acetylacetonate, $Ni(acac)_2$, a member of this group of complexes, is employed in optoelectronics [186, 187], electrocatalysis [188], polymer chemistry [189, 190], film growth [191, 192], synthesis of nanoparticles [193] and nanocomposites [194–196].

However, the properties of $Ni(acac)_2$ adsorbed on iron are still scarcely described in literature. In 1967, Kishi and coworkers proposed a description of the adsorption of acetylacetonate units on nickel and iron, based on infrared and ultraviolet spectroscopy [197]. The adsorption and the decomposition of $Ni(acac)_2$ on a metallic substrate was never investigated, to the best of our knowledge. In fact, this compound was never studied for tribological purposes, yet its interaction with metallic substrates is worthy to explore because of its interesting catalytic activity that may eventually turn out to be different under mechanical stresses. Therefore, understanding the atomistic mechanism of dissociation of this complex on a metal can be useful to clarify its functionality. Here, we present a study based on density functional theory (DFT) concerning the adsorption and the dissociation of $Ni(acac)_2$ on iron. After completing the existing data in literature with structural and electronic properties which were never calculated before for isolated $Ni(acac)_2$ by means of DFT, we present in this work the adsorption and the dissociation energies of this complex on different sites of the iron surface.

6.2 Methods

We focused on the monomeric form of the $Ni(acac)_2$ complex shown in Figure 6.1.

To study the properties of $Ni(acac)_2$ and its interaction with an iron surface, the Quantum Espresso package][128, 129] was used to perform first-principle calculations within the framework of DFT. The Perdew, Burke and Ernzerhof (PBE) approximation [127] was used to describe electronic exchange and correlation. The plane wave/pseudopotential approach was empoloyed, with cutoffs of 35 Ry and 280 Ry applied to the kinetic energy of the wavefunctions and the charge density, respectively, as the pseudopotentials were ultrasoft. The choice for these values of the cutoffs is justified in Appendix E. Spin polarization was used and a smearing with Gaussian functions was applied with a width of 0.02 Ry to better describe electronic occupations around the Fermi level. For the geometry optimization of the isolated complex, a cubic supercell of 60 Å was used to avoid interactions between the periodic replicas. The adsorption of the molecule on

Reproduced with permission from C. Corsini, **S. Peeters**, M. C. Righi, J. Phys. Chem. A 2020, 124, 39, 8005-8010. Copyright 2020 American Chemical Society.

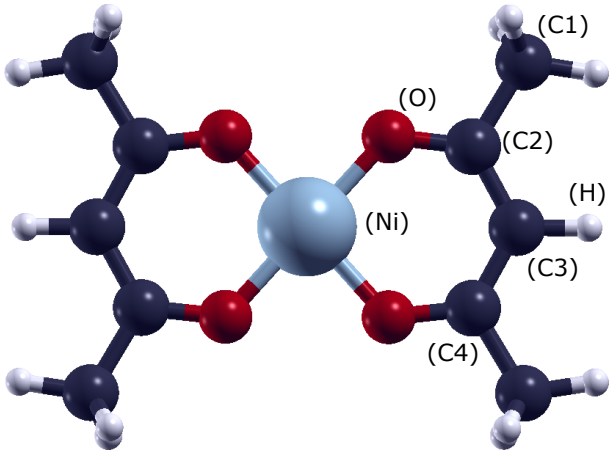


Figure 6.1: Chemical structure of Ni(acac)$_2$.

iron was studied considering the (110) surface, as it is the most stable surface for this metal [146, 182]. A supercell of iron with $5 \times 3\sqrt{2}$ in-plane size and a height of $6\sqrt{2}$ times the lattice parameter of bulk iron was used, containing a slab composed of four layers with 30 atoms each. Integrations were carried out at the Γ point for the calculations in the cubic cell, while for the orthorhombic cell a 2x2x1 Γ-centered grid was chosen. An initial guess for the geometry of the complex was obtained with the software Avogadro [130]. The molecular structure was then optimized, with the total energy and the forces converged under the thresholds of 10^{-4} Ry and 10^{-3} Ry, respectively.

6.3 Results and Discussion

6.3.1 Properties of isolated Ni(acac)$_2$

The chemical structure of Ni(acac)$_2$ obtained from the geometry optimization agrees with the other existing data in literature [198–200]. Calculated bond lengths and angles, reported in Table 6.1, differ no more than 2% and 3% in absolute value, respectively, compared to previous experimental and theoretical observations. The symmetry of the complex was also verified by analyzing the discrepancies among equivalent bonds. Such discrepancies always lied below 0.1%, which is a low enough value to reasonably confirm the symmetry of the chemical structure.

Electronic properties of the Ni(acac)$_2$ complex were also evaluated. The ionization energy E_i was calculated as:

$$E_i = E_{Ni(acac)_2^+} - E_{Ni(acac)_2} \tag{6.1}$$

where $E_{Ni(acac)_2^+}$ and $E_{Ni(acac)_2}$ are the total energies of the cationic complex obtained by removing one electron and of the neutral complex, respectively. The calculated value of 6.25 eV is comparable to the experimental one of 7.41 eV [201], with an underestimation of about 16%, most probably due to the well-known problem of the fundamental gap in DFT [183].

Table 6.1: Bond lengths and angles of Ni(acac)$_2$. The atomic labels correspond to the ones shown in Figure 6.1.

Bond	Length (Å)	Angle	Size (°)
Ni-O	1.85	O-Ni-O	95.9
O-C2	1.28	Ni-O-C2	125.6
C2-C3	1.40	O-C2-C3	125.0
C2-C1	1.51	O-C2-C1	114.5
C3-H	1.09	C2-C3-C4	122.9

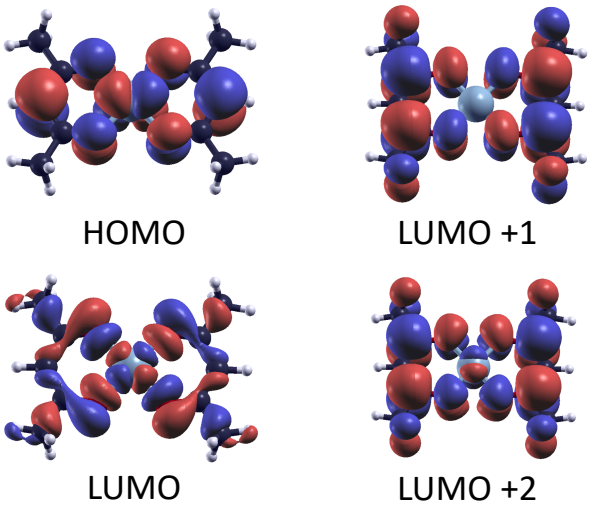


Figure 6.2: Frontier molecular orbitals of Ni(acac)$_2$ plotted with an isovalue of 0.003. The red and the blue colors of the isosurfaces identify the positive and negative sign of the wave function, respectively.

The frontier molecular orbitals of Ni(acac)$_2$ are shown in Figure 6.2. The lowest energy state corresponds to a singlet state in which the highest occupied molecular orbital (HOMO) is the result of a combination of the d_{xz} orbital of Ni, accounting for almost 70% of the wave function, and one p_z orbital for each of the O and C3 atoms, collectively accounting for more than 20% of the wave function. The LUMO is composed of almost 60% of the Ni d_{xy} orbital and of the O p_y orbitals, which collectively account for almost 25% of the wave function. LUMO+1 and LUMO+2, which are mostly obtained by combining p_z orbitals of the C and O atoms of the ligand units, are in perfect agreement with the plots proposed in literature for the LUMO and LUMO+1 [202]. In fact, the high number of nodal planes in the lowest unoccupied molecular orbital (LUMO) may suggest that the calculated energy of this orbital is underestimated, and it should lie above LUMO+2.

In order to estimate which could be the most favorable dissociation pattern for the isolated complex, the fragmentation energy E_{frag} was determined as:

$$E_{frag} = E_{frag_1} + E_{frag_2} - E_{Ni(acac)_2} \tag{6.2}$$

where E_{frag_1} and E_{frag_2} are the total energies of the individual fragments obtained after molecular dissociation. This analysis aims at comparing different ways of breaking the molecules in order to evaluate the strength of the broken bonds. The absolute values of fragmentation energies obtained in Equation 6.2 cannot represent realistic dissociative events, where the fragments can rearrange and can be stabilized by the presence of other chemical species. However, it is instructive to compare the fragmentation energies of different possible fragmentation patterns to understand which are the strongest bonds in the complex. We considered nine different fragmentation patterns in total, shown in Figure 6.3. These patterns do not exhaust all the possible combinations for the molecular dissociation, yet they were chosen among the most representative cuts for this complex.

The lowest fragmentation energy is observed in the case of Cut 2, where two Ni-O bonds are broken. Breaking two C-C bonds is more difficult, requiring 5.8 (Cut 8) to 7.4 (Cut 1) eV more than Cut 2. As expected, the fragmentation energy of mixed patterns where a Ni-O bond and a C-C bond are broken lie in the middle. Therefore, Cut 2 could be the most likely to occur for isolated molecules, as the energy required to separate the two fragments is lower with this scheme. However, the effect of a metallic substrate can change the picture provided by these calculations, as the fragments of the molecules can be stabilized differently on the surface of the metal, in favor of a dissociative pattern which involves the stronger C-O bonds.

One could roughly estimate the strength of individual bonds in the complex by considering half of the fragmentation energies of Cuts 1, 2 and 4. This calculation would provide 5.96, 2.25 and 5.46 eV for C-O, Ni-O and C-CH bonds, respectively. Cuts 5-9 are indeed the combination of these fragmentation patterns and summing up the fragmentation energies of the individual bonds would provide 7.71, 8.21 and 11.4 eV for Ni-O + C-CH (Cuts 5 and 6), Ni-O + C-O (Cut 7) and C-O + C-CH (Cut 8 and 9), respectively. These last values differ from the energies on the right side of Figure 6.3. Such discrepancies are most probably due to the different electronic structure of the fragments, which is left to relax to the minimum energy configuration in all the calculations. Constraining the electronic configurations by assigning specific spin multiplicities to the fragments would probably provide a better agreement between the calculated bond strengths, yet such a detailed analysis goes beyond the purpose of this study, as a qualitative consistency can already be observed in the fragmentation energies calculated with the present approach.

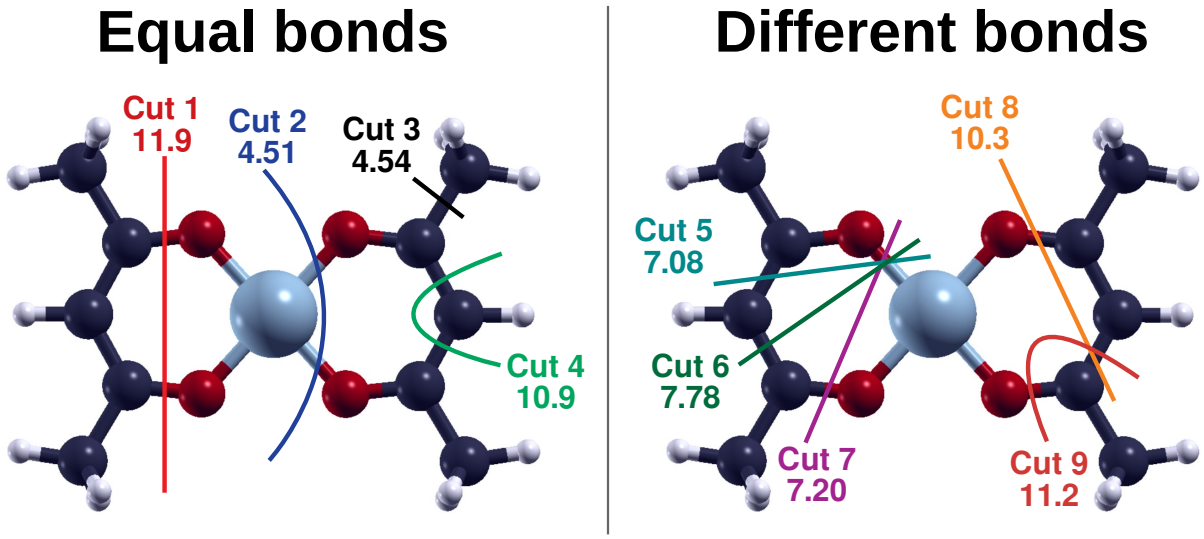


Figure 6.3: Fragmentation patterns considered for Ni(acac)$_2$, divided in two groups depending whether equal or different bonds are broken. An exception is Cut 3, in which a single bond is broken, compared to all the other patterns in which two bonds are broken. The fragmentation energies, calculated as in Equation 6.2 and expressed in eV, accompany each pattern.

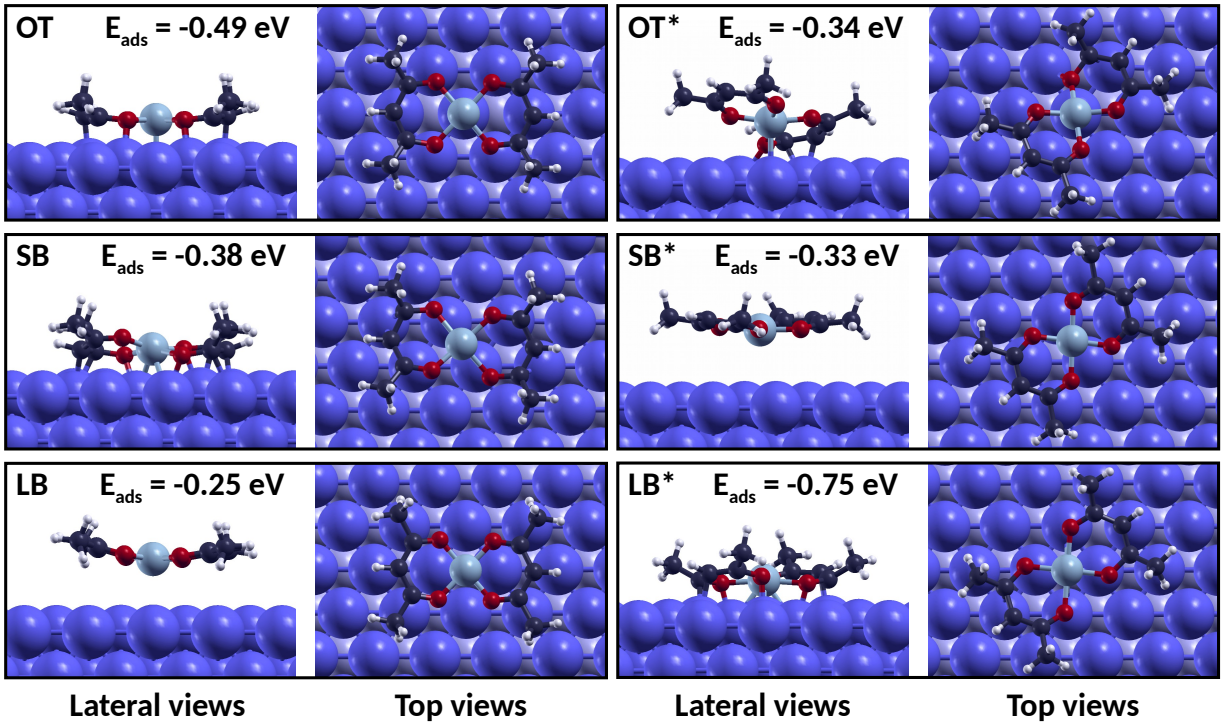


Figure 6.4: Optimized geometries of $Ni(acac)_2$ on the iron (110) surface, with the complex placed in the *on top* (OT), *short bridge* (SB), *long bridge* (LB) configurations and their rotated counterparts, marked by an asterisk, along with the respective adsorption energies. The size of the blue-colored iron atoms was increased by 50% in the pictures. In the top views, the iron atoms below the first layer were colored with a lighter blue to better distinguish the relevant sites on the surface.

6.3.2 Adsorption and fragmentation on iron

To better understand the effect of a metallic substrate on the chemical properties of $Ni(acac)_2$, the $Ni(acac)_2$ complex was adsorbed on the iron (110) surface. Three non-equivalent sites of the surface were chosen as the initial position of the Ni atom of the complex: the position *on top* of on iron atom (OT), the two-fold coordination site, called *short bridge* (SB), and the four-fold coordination site, called *long bridge* (LB). Two different orientations of the complex were considered for all the three sites: with the ligand units parallel to the y axis of the supercell (OT, SB and LB) and with the complex rotated by 45° (OT*, SB* and LB*). During the geometry optimization of the complexes on the iron surfaces, the x and y coordinates of the Ni atom were kept fixed, while all the other degrees of freedom were allowed to relax. The final configurations of the adsorbed systems are shown in Figure 6.4.

When the complex was in the OT, OT*, SB and LB* configurations, the complex chemisorbed on the iron surface, while in the case of the SB* and LB configuration only physisorption could be established. For all of these systems, the adsorption energy E_{ads} was evaluated as:

$$E_{ads} = E^{iron}_{Ni(acac)_2} - E_{Ni(acac)_2} - E_{iron} \tag{6.3}$$

where $E^{iron}_{Ni(acac)_2}$ and E_{iron} are the total energies of the system composed by the complex adsorbed on the iron slab, and of the iron slab alone, respectively. The adsorption energy for each configuration is included in Figure 6.4. One of the most favorable configuration for the Ni atom on the surface is the OT position. However the LB* configuration is especially favorable because all the O and C3 atoms are almost on top of iron atoms, increasing the number of bonding interactions and leading to a more stable configuration. In fact, rotating the complex by 45° is favorable only when the Ni atom is on the LB site. In the other cases, instead, the rotated complex cannot efficiently adsorb on the surface, resulting in twisted geometries (OT*) or weak physisorption (SB*).

6.3.3 Bond dissociation on iron

The metallic substrate can play an important role in modifying the mechanisms of molecular dissociation. In order to verify whether the dissociation mechanism predicted for isolated Ni(acac)$_2$ is still the most favorable also on iron, we calculated the dissociation energies on the substrate E^{iron}_{frag} as:

$$E^{iron}_{frag} = E^{iron}_{central} + 2E^{iron}_{ligand} - E^{iron}_{Ni(acac)_2} - 2E_{iron} \tag{6.4}$$

where $E^{iron}_{central}$ and E^{iron}_{ligand} are the total energies of the fragments corresponding to the central metallic unit and to a single ligand unit, respectively, adsorbed on the iron surface. The total energy of the iron slab must be subtracted twice in Equation 6.4 to balance the number of iron atoms. The dissociation energies on iron were calculated for different placements of the metallic centers and ligand units originated by Cut 1 and Cut 2. Lateral and top views of the fragments considered are included in Figure 6.5. The sites and orientations considered for the central metallic units were the most favorable found in the adsorption calculations, namely OT, SB and LB*. Three different orientations were considered for each of the ligand units, which were left to relax freely on the surface. Each ligand unit was placed on the iron surface with the carbon chain parallel to the x axis, rotated by 45°, and parallel to the y axis, in order to explore different adsorption configurations on the surface. For both the fragments, the most favorable configurations turned out to be the ones in which the units were rotated by 45°. These adsorption configurations, shown in the bottom panels of Figure 6.5, were the ones considered for the calculation of the dissociation energy in Equation 6.4.

Table 6.2 reports the calculated dissociation energies of the Ni(acac)$_2$ complex on the iron surface. All the calculated dissociation energies are negative, meaning that the dissociation of the complex is favorable on the substrate. Cut 1 is the most favorable way of breaking the complex, as the energies obtained from this pattern are higher in absolute value than the ones of Cut 2. This result shows that the preferred dissociation pattern changes from Cut 2 for the isolated molecule to Cut 1 for the complex adsorbed on the iron substrate. The fragments obtained upon dissociation on the iron surface can be stabilized differently with respect to the isolated molecular fragments, which are unable to relax their strained geometry. In particular, for Cut 1, such favorable values of dissociation energies are also due to the detachment of the oxygen atoms of the central metallic cores, leading to a significantly higher stability of the system. For both dissociation patterns, the most favorable destination for the metallic core is the SB position, providing the lowest (highest in absolute value) dissociation energy.

Since only part of the O atoms detached from the Ni atom in the central units originated by Cut 1, we verified whether the full dissociation of the NiO_4 unit on iron is thermodynamically favorable, by calculating the following reaction energy:

$$E^{iron}_{frag,central} = E^{iron}_{Ni} + 4E^{iron}_{O} - E^{iron}_{NiO_4} - 4E_{iron} \tag{6.5}$$

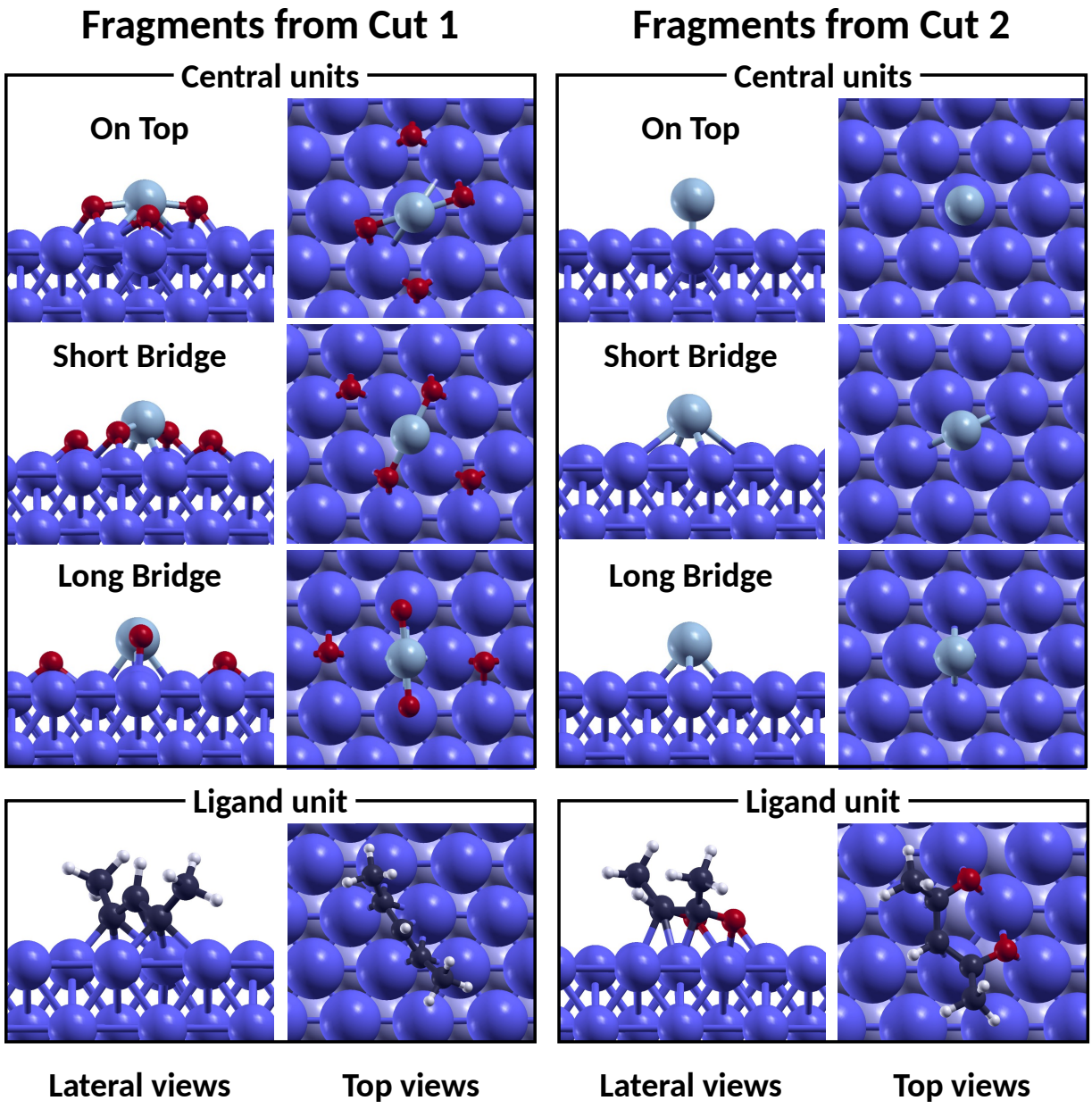


Figure 6.5: Optimized geometries of the fragments of Ni(acac)$_2$ obtained from Cut 1 and Cut 2 on the iron surface. In the top views, the size of all the iron atoms was increased by 50% and the atoms below the first layer were colored with a lighter blue.

where $E^{iron}_{frag,central}$ is the energy required to fully divide the NiO_4 central unit and E^{iron}_{Ni}, E^{iron}_{O} and $E^{iron}_{NiO_4}$ are the total energies of the respective isolated species, all adsorbed on iron. The values of $E^{iron}_{frag,central}$ vary by changing the adsorption site of the Ni atom on the surface, yet they range from -1.33 (SB) to -2.20 eV (LB), with the negative sign indicating that the full dissociation of the NiO_4 central unit is favorable and that the final product of the dissociation will most probably consist of Ni and O atoms fully separated on the iron surface, as long as enough energy is provided to the system to overcome the dissociation barriers.

Table 6.2: Reaction energies for the dissociation on the iron substrate E^{iron}_{frag} in eV.

	OT	SB	LB*
Cut 1	-1.88	-2.70	-1.62
Cut 2	-0.82	-1.49	-1.27

In a previous study regarding molybdenum dithiocarbamates we discovered that the most probable fragmentation pattern for these complexes on iron differs from the one for the isolated complexes, predicted by analyzing the strength of the bonds that take part in the dissociation [167, 175]. The results of the fragmentation analysis are in perfect agreement with the ones obtained in this work for Ni(acac)$_2$ and they suggest the following general rules for small metallorganic complexes interacting with the iron surface:

1. While the molecular dissociation of the isolated complexes is energetically unfavorable, the iron substrate is capable to stabilize the fragments of the dissociation, turning it into a favorable process.

2. The dissociation pattern in which the weakest bonds of the isolated complexes are broken is not the most probable when the complexes are on the iron surface. Alternative paths can be observed in which stronger bonds are broken, due to the stabilization of the relative fragments by the substrate.

In fact, Ni(acac)$_2$ and most of the MoDTC structures on iron can be broken more preferably between the chalcogen atoms and the adjacent carbon atoms of the ligand units. These chalcogen atoms remain near the central metallic units, completing the coordination of the metal, and possibly detach in a subsequent step, while the carbon atoms with broken bonds strongly bind to the iron surface.

6.4 Conclusions

We presented a study concerning the interaction of Ni(acac)$_2$ with an iron surface by means of DFT. After confirming a good agreement between the optimized geometry of the complex with the existing structural data available, we calculated the frontier orbitals and the ionization energy of this complex for the first time with DFT. A fragmentation analysis both for the isolated complex and for the complex adsorbed on iron was performed and different adsorption sites were considered to understand which is the most preferable configuration of Ni(acac)$_2$ on the iron surface. The main results are summarized in the following:

- For isolated Ni(acac)$_2$, the most favorable fragmentation pattern is *Cut 2*, corresponding to the dissociation of the acetylacetonate ligand units from the nickel atom.

- The most favorable adsorption configuration for Ni(acac)$_2$ on the iron surface is LB*, requiring the nickel atom to be in the *long bridge* position and the oxygen atoms to be on top of the nearest iron atoms. After dissociation, the central metallic unit of the complex is more stabilized in the *short bridge* position.
- Both dissociation patterns, which are not favorable for the isolated complex, become favorable on iron. The most favorable fragmentation pattern for the complex adsorbed on iron becomes *Cut 1* due to the stabilization effect of the substrate. These observations, in agreement with the ones drawn for MoDTC complexes, suggest a possible generalization of the dissociation mechanism on the iron surface for small metallorganic complexes where the ligand units are connected to the metallic center through chalcogen atoms.

The reaction energies for the fragmentation calculated in this work do not take into account the energy barriers associated to the dissociation. A further step of the study could include the estimation of such barriers and the dynamic simulations of the dissociation, to better understand the kinetics of the different mechanisms.

Chapter 7

Final remarks and future perspectives

The aim of this thesis is to provide insight on the chemical and physical properties of organometallic complexes of particular interest for tribology, with a focus on the tribochemistry of MoDTC. All the computational results obtained in this work were obtained by first-principles atomistic simulations, which are the only appropriate tool available today to accurately describe the chemical reactivity in the presence of mechanical stresses. Unravelling the tribochemistry of MoDTC is complicated because of the different chemical reactions occurring at the tribological interface, the wide number of chemical compounds present in the lubricant at the same time and the dependence of the friction reduction performance on several experimental conditions, i.e. normal load, temperature, concentration of the additives in the mixture. A systematic approach is necessary to tackle such a complex problem.

One of the open questions was the role of oxygen. Oxidation was shown to occur experimentally in samples containing MoDTC, yet the effect of additional oxygen atoms in the chemical structures was unclear. Firstly, we showed that the oxidation of the complexes is favorable in a wide range of conditions and the most favorable position for oxygen atoms is the ligand position. The MoDTC structures hosting O atoms in ligand position are able to release central units containing only Mo and S on the metallic substrate with the correct stoichiometry to form MoS_2. Oxygen atoms are in fact seized by the ligand units and do not interfere with the formation of the tribofilm. However, oxygen also plays a negative role when it covers the adsorption sites of the metallic substrate. We have shown by means of a combined experimental and computational approach that the activation of MoDTC additives is delayed when the surface of iron is oxidized. The bare metal needs to be exposed first in order to achieve a stable adsorption of MoDTC on the metal and, therefore, a durable MoS_2 tribofilm.

The dissociation mechanism of MoDTC is an issue debated since long time, because different reaction paths were proposed based on experimental observations. The catalytic effect of the metallic substrate is key to govern the decomposition, because this process changes whether the compound is isolated or adsorbed on iron. For the isolated complex with sulfur in ligand position the weakest bonds are the ones between molybdenum and sulfur. When this compound is adsorbed on iron, however, the C-S bonds are broken first, in agreement with the mechanism proposed by Khaemba and coworkers. The chemistry of the complexes also influences the dissociation mechanism, because MoDTC compounds with oxygen in ligand position undergo a different mechanism, in agreement with the one proposed by Grossiord and coworkers. In that case, the O-Mo bonds are broken first while the C-O bond remains intact even when the complex is adsorbed on iron.

The dissociation of the additives did not occur only because of the catalytic activity of the substrate. This thesis demonstrates the importance of mechanical stresses in promoting chemical reactivity. In fact, simulations helped to decouple the different effects that are generally in play at the same time in experimental systems. Load and shear stress imposed on the substrates were the key to activate the chemical decomposition of MoDTC additives at the interface of iron and the reorganization of their central units, as showrn in Appendix C. In particular, while load destabilizes the chemical structures due to the repulsion of the electronic wave functions of the different species, shear force allows the atoms to overcome

energy barriers. The sliding motion helps the species to escape from the local minima of the potential energy surface and reach the absolute minima.

The chemical composition of commercial MoDTC products is heterogeneous and for this reason the structural, electronic and vibrational properties of MoDTC compounds were never described in literature, despite the wide use of these additives in commercial lubricants. We presented a complete characterization of dimeric and monomeric MoDTC structures, along with their interaction with the metallic substrate. All the properties calculated in this work can be useful to distinguish these complexes in experimental samples and to connect the fundamental aspects of their chemistry to their remarkable friction reduction performances. The mononuclear MoDTC compounds are of particular interest for this field because they can be commonly found in the lubricant mixtures. They have different chemical properties than their dimeric analogues, yet they have been completely neglected in the scientific literature until very recently [203].

The similarities in the dissociation mechanism of MoDTC and other organometallic complexes such as $Ni(acac)_2$ on iron suggests that it is possible to generalize such a decomposition model. Our computational protocol was demonstrated to be capable of offering valuable predictions on the chemistry and the reaction mechanism of lubricant additives. Clarifying the decomposition mechanism of these compounds and, possibly, proposing models for the tribochemistry of friction modifiers are extremely beneficial in the pursuit of improved lubrication technologies.

The results contained in this work have been summarized in the following articles:

- S. Peeters, P. Restuccia, S. Loehlé, B. Thiebaut and M. C. Righi, *Characterization of Molybdenum Dithiocarbamates by First-Principles Calculations*, J. Phys. Chem. A 2019, 123, 32, 7007-7015.
- S. Peeters, P. Restuccia, S. Loehlé, B. Thiebaut and M. C. Righi, *Tribochemical Reactions of MoDTC Lubricant Additives with Iron by Quantum Mechanics/Molecular Mechanics Simulations*, J. Phys. Chem. C 2020, 124, 25, 13688-13694.
- C. Corsini, S. Peeters and M. C. Righi, *Adsorption and Dissociation of Ni(acac)$_2$ on Iron by Ab Initio Calculations*, J. Phys. Chem. A 2020, 124, 39, 8005-010.
- G. Losi, S. Peeters, F. Delayens, H. Vezin, S. Loehlé, B. Thiebaut and M. C. Righi, *Experimental and Ab-Initio Characterization of Mononuclear Molybdenum Dithiocarbamates in Lubricant Mixtures*, accepted for publication in Langmuir.
- S. Peeters, C. Charrin, I. Duron, S. Loehlé, B. Thiebaut and M. C. Righi, *Importance of the catalytic effect of the substrate in the functionality of lubricant additives: the case of MoDTC*, submitted for publication.
- S. Peeters, P. Restuccia, G. Losi, S. Loehlé, B. Thiebaut and M. C. Righi, *Crystallization of MoS_2 from central units of MoDTC by ab-initio simulations*, in preparation.

7.1 Future perspectives

Concerning the computational characterization of MoDTC structures, it may be interesting to further study the interaction of the additives with the rest of the molecules of the lubricant. In Chapter 2 the effect of solvents on the geometry and the vibrational properties of the compounds was simply studied by employing the polarizable continuum model (PCM) and the presence of 1-hexene. The results showed that no significant changes occur on the structure or the normal modes of MoDTC, yet the effect of temperature

and the interaction among several molecules was not considered and could be useful to take them into account in order to bridge the gap between computational and experimental observations. Furthermore, an important aspect is the interaction between different MoDTC molecules. In this study we focused on the properties of single molecules and their interaction with iron to gain a fundamental understanding of their physico-chemical properties. Two MoDTC molecules were able to interact in many of our dynamic simulations. A further step could include the interaction of several MoDTC structures in the same simulation cell, because the MoS_2 tribofilm can be generated thanks to the cooperation of many of these molecules. In that case, one would need to properly design the compuational system. Our preliminary attempt to tackle this problem is presented in Appendix C, although there is plenty of room for extension.

Ab-initio molecular dynamics, especially in the form of the QM/MM approach, represent one of the most efficient ways to accurately represent tribochemical reactions. Yet, the size of the dynamic systems simulated in this work are still an important computational effort. Machine-learning techniques have been proven successful in the design of force fields able to reproduce the quality of ab-initio simulations [204, 205]. Therefore, with the development of machine-learned force fields based on DFT calculations it may be possible to extend the size and the timescales of these dynamic simulations, allowing to describe the interactions of several MoDTC molecules, the diffusion of molecular fragments that do not take part in the formation of the tribofilm and possibly the full tribochemical reaction.

To better put the results on the interaction between MoDTC and the substrate in perspective, it may be worth to explore different substrates such as iron oxide and DLC. The latter has been recently considered for an experimental investigation involving the lubrication by MoDTC and MoS_2 [159]. Here we only focused on iron, as it can be considered a simplified model for steel. Within DFT, an accurate description of iron already represents a considerable task. We also took into account iron surfaces covered by oxygen, because bare iron can be exposed to the additives only after removing the oxide layers at the surface of the metal. While the results presented in this thesis could be reasonably extended to other metallic systems, simulating the tribochemistry of MoDTC on different substrates would help to generalize the results and predict the reactivity of MoDTC for a wide range of materials. Yet, this interesting issue goes beyond the purpose of this work.

The experimental work presented in Chapter 5 could be extended by optimizing the separation protocol of the MoDTC commercial product. Although the studied fractions were already chemically different, improving the separation would provide more homogeneous fractions. The identification of physico-chemical properties specific to sub-groups of MoDTC structures would then become easier. Dynamic simulations could also be performed to verify the predictions on mononuclear MoDTC offered by static calculations.

The investigation of $Ni(acac)_2$ provided results which are perfectly aligned with the ones obtained for MoDTC. Even though the properties of this compound were studied here in the abscence of mechanical stresses, Chapter 6 demonstrated the full capability of the computational protocol adopted here to gain fundamental insight on systems of potential interest for tribology. To better understand whether $Ni(acac)_2$ could indeed be useful for tribological applications, dynamic simulations should be carried out to extend the predictions offered in Chapter 6. Whether the reactivity and the catalytic properties of $Ni(acac)_2$ change in the presence of mechanical stresses should be verified, with the aid of experiments.

Appendix A

Supporting Information for: Characterization of Molybdenum Dithiocarbamates by First Principles Calculations

A.1 Convergence test on the relative stability of isomers

In order to accurately describe the simulated systems while maintaining the computational effort feasible, one has to appropriately select the kinetic energy cutoff for the wave functions to reach a compromise between the two requirements. Figure A.1 reports the convergence test for the energy difference ΔE, calculated as follows:

$$\Delta E = E_{IsoA} - E_{sMoDTC} \tag{A.1}$$

where E_{IsoA} and E_{sMoDTC} are the total energies of Isomer A and sMoDTC, respectively, by varying the kinetic energy cutoff for the wave functions. The chemical structures of sMoDTC and Isomer A are shown in Figures 1 and 5 of the main text, respectively. The cutoff was increased by 5 Ry for each step of the test and the value of 40 Ry was chosen for the energy cutoff to ensure that the difference between two values of ΔE calculated at two consecutive steps was globally below 2 meV. The difference between the values of ΔE calculated at 45 Ry and 40 Ry turned out to be 1.5 meV ($5 \cdot 10^{-5}$ eV per atom).

A.2 Comparison of calculated structural data with experiments

In order to validate the structural data calculated for MoDTC, we carried out a geometry optimization of two isolated anions, $Mo_2O_2S_6{}^{2-}$ and $Mo_2O_2S_8{}^{2-}$, having a chemical structure similar to MoDTC. These two chemical structures were more extensively described in the literature, offering experimental data to compare with the simulations. Figures A.2 and A.3 represent the chemical structures of the two anions, while Tables A.1 and A.2 report a selection of the corresponding structural data.

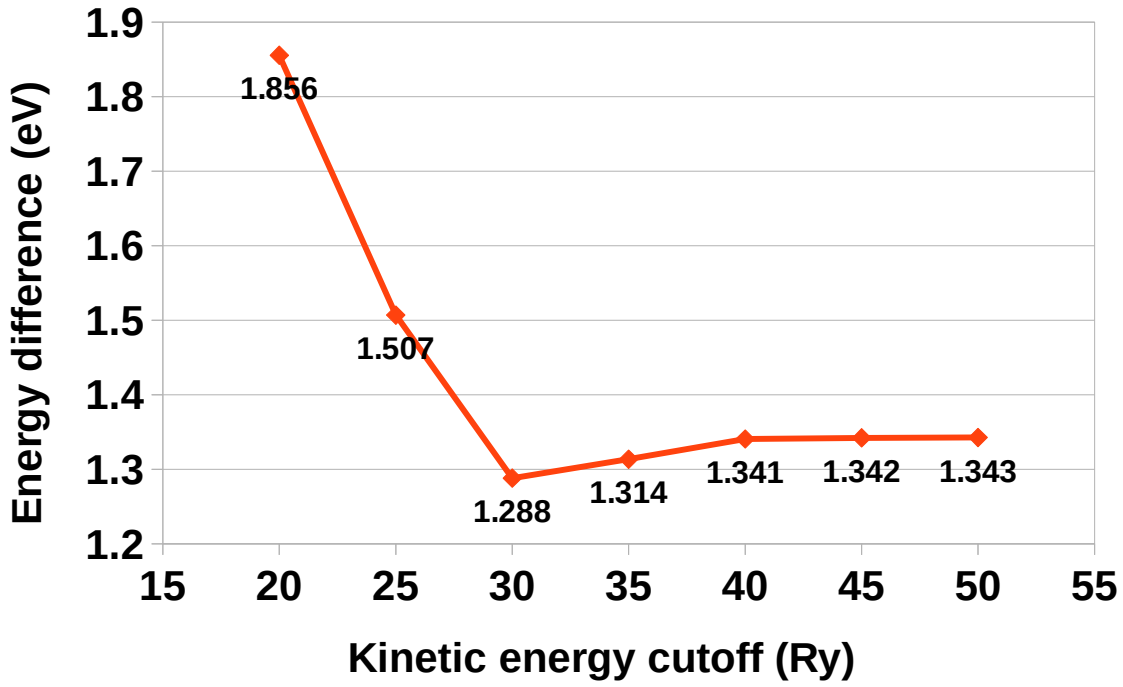


Figure A.1: Convergence test of the energy difference ΔE between sMoDTC and Isomer A by varying the kinetic energy cutoff for the wave functions. For each step of the test, the value of ΔE is included in the graph.

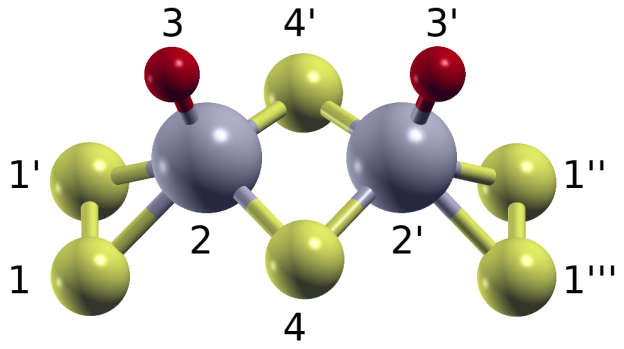


Figure A.2: Molecular structure of the $Mo_2O_2S_6{}^{2-}$ anion. Red, yellow and gray colors correspond to oxygen, sulfur and molybdenum, respectively.

Table A.1: Lengths and angles of selected bonds. The numbers in brackets follow the numbering proposed in Figure A.2. [a] Experimental data from literature [138]. [b] Simulated data in the present work.

Bond	Exp. (Å)[a]	Sim. (Å)[b]	Angle	Exp. (°)[a]	Sim. (°)[b]
S(1)-S(1')	2.066	2.070	S(1)-Mo(2)-S(1')		50.2
S(1)-Mo(2)	2.402	2.438	Mo(2)-S(1)-S(1')		64.9
S(1')-Mo(2)	2.385	2.439	S(1)-Mo(2)-O(3)		109.7
Mo(2)-O(3)	1.687	1.719	O(3)-Mo(2)-S(4)		109.4
Mo(2')-O(3')	1.679	1.719	S(4)-Mo(2)-S(4')	102.1	102.1
Mo(2)-S(4)	2.323	2.344	S(1)-Mo(2)-S(4)		90.4
Mo(2)-S(4')	2.321	2.345	Mo(2)-S(4)-Mo(2')	75.0	75.1
Mo(2)-Mo(2')	2.828	2.858	O(3)-Mo(2)-Mo(2')		107.5

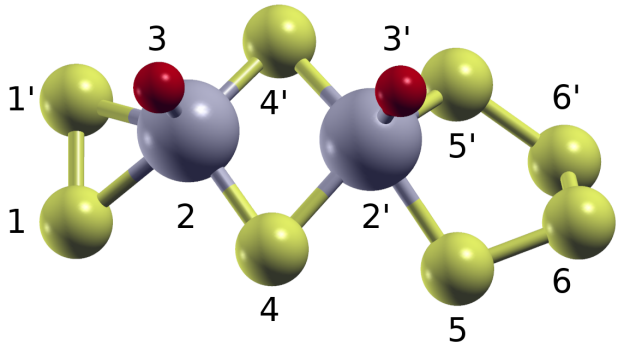


Figure A.3: Molecular structure of the $Mo_2O_2S_8{}^{2-}$ anion. Red, yellow and gray colors correspond to oxygen, sulfur and molybdenum, respectively.

Table A.2: Lengths and angles of selected bonds. The numbers in brackets follow the numbering proposed in Figure A.3. [a] Experimental data from literature [139]. [b] Simulated data in the present work.

Bond	Exp. (Å)[a]	Sim. (Å)[b]	Angle	Exp. (°)[a]	Sim. (°)[b]
S(1)-S(1')	2.071	2.070	S(1)-Mo(2)-S(1')	51.4	50.3
S(1)-Mo(2)	2.389	2.429	S(1)-Mo(2)-S(4')	131.4	130.3
S(1')-Mo(2)	2.385	2.442	S(1)-Mo(2)-S(4)	91.4	90.1
Mo(2)-O(3)	1.663	1.719	S(1)-Mo(2)-O(3)	109.2	109.7
Mo(2')-O(3')	1.684	1.715	S(4)-Mo(2)-O(3)	108.8	108.2
Mo(2)-S(4)	2.312	2.312	S(4)-Mo(2)-S(4')	101.7	102.9
Mo(2')-S(4)	2.349	2.372	Mo(2)-S(4)-Mo(2')	74.7	75.9
Mo(2)-S(4')	2.288	2.317	Mo(2)-S(4')-Mo(2')	74.8	75.5
Mo(2')-S(4')	2.364	2.400	S(4)-Mo(2')-S(5)	76.9	76.5
Mo(2')-S(5)	2.411	2.432	O(3')-Mo(2')-S(5)	105.9	104.0
Mo(2')-S(5')	2.422	2.461	O(3')-Mo(2')-S(5')	108.8	109.2
Mo(2)-Mo(2')	2.827	2.889	Mo(2')-S(5)-S(6)	102.7	103.3
S(5)-S(6)	2.062	2.080	Mo(2')-S(5')-S(6')	112.3	111.9
S(5')-S(6')	2.088	2.129	S(5)-S(6)-S(6')	102.3	101.3
S(6)-S(6')	2.014	2.046	S(5')-S(6')-S(6)	102.7	102.0

A.3 Comparison between the computer programs

In this section we report a comparison of the results obtained with Quantum ESPRESSO (QE) and Gaussian 09: the formation energy of sMoDTC from isolated atoms, the energy difference between isomers and sMoDTC, the energy difference between substituted compounds and sMoDTC were calculated with both computer programs and compared.

A.3.1 Formation energy of sMoDTC

Firstly, we calculated the formation energy of sMoDTC from isolated atoms by employing the following formula:

$$E_{form} = E_{sMoDTC} - 12 \cdot E_H - 6 \cdot E_C - 2 \cdot E_N - 2 \cdot E_O - 6 \cdot E_S - 2 \cdot E_{Mo} \tag{A.2}$$

where E_{sMoDTC}, E_H, E_C, E_N, E_O, E_S and E_{Mo} are the total energies of sMoDTC and isolated H, C, N, O, S and Mo atoms, respectively.

The same cells and parameters were used for all the calculations with QE, as explained in the main text, and the formation energy was -130.4 eV in this framework. For all the calculations with Gaussian, the proper spin multiplicity of the isolated atoms was taken into account and all the other parameters were chosen as explained in the main text. The formation energy with Gaussian was -132.5 eV, approximately 1.6% lower than the one estimated by QE. To the best of our knowledge, no experimental value of the formation energy of MoDTC has ever been reported.

A.3.2 Energy difference between isomers and sMoDTC

The geometry of all the isomers presented in Figure 5 of the main text was optimized both with QE and Gaussian. Since some discrepancies appeared in the calculated energy differences between the isomers and sMoDTC with the two softwares, we carried out an additional geometry optimization by employing the B3LYP functional [142–145] to better understand the source of such discrepancies. Table A.3 reports the energy differences obtained with the three methods.

Table A.3: Energy differences in eV between the isomers and sMoDTC.

Isomer	Quantum ESPRESSO	Gaussian PBE	Gaussian B3LYP
Isomer a	1.34	1.52	1.45
Isomer b	0.57	0.66	0.61
Isomer c	0.54	0.76	0.58
Isomer d	0.53	0.71	0.55
Isomer e	-0.02	0.17	-0.09
Isomer f	-0.04	0.07	-0.06
Isomer g	-0.04	0.17	-0.09
Isomer h	-0.13	0.10	-0.13

The bridging position of oxygen atoms was confirmed to be unfavourable with all the methods employed. However, the energy ordering of the chemical structures was not fully maintained from QE to the Gaussian

PBE picture. With Gaussian PBE, sMoDTC was found to be the most stable structure with respect to all the other isomers. The ligand position was still one of the most favourable positions for oxygen atoms in MoDTC. We believe these discrepancies to be strictly related to the nature of the PBE functional employed for the calculations with Gaussian. Indeed, by comparing the results of Gaussian B3LYP with QE a much better agreement appeared and the ligand position was found to be the most favourable for O atoms. We do not expect the optimized geometry of the molecules nor periodic cells in the case of QE to be the source of such discrepancies.

In order to understand why sMoDTC appears to be more stable than Isomer h in the Gaussian PBE picture, we compared the NBO analyses of these two compounds calculated both with the PBE and the B3LYP functionals. While most of the interactions appeared to be similar for each structure by varying the functional, a bond and an antibond between sulfur atoms in ligand position of sMoDTC arose in the PBE picture. These bonds were purely covalent and almost entirely of p character. Particularly, the bond between S atoms had a strong interaction with the adjacent N-C bond of approximately 106 kcal/mol. Such interaction was absent in the structure calculated with B3LYP. As the geometry of sMoDTC was optimized both with PBE and B3LYP, we ensured that such interactions were not originated by the different atomic positions, by repeating the calculation of the electronic structure and the NBO analysis with PBE at the geometry optimized with B3LYP and vice versa. Consistently, the interactions between S atoms in ligand position and the relative stabilization effect involving the adjacent N-C bond were found only by employing PBE to calculate the electronic structure, regardless of the atomic positions. Since no other major difference was identified between the results of the NBO analyses for Isomer h with the two different functionals, we believe that these interactions can play a role in modifying the energetic ordering of sMoDTC and its isomers.

The bond between sulfur atoms in ligand position of sMoDTC, found in the Gaussian PBE picture, can be observed by plotting the difference between the charge densities calculated with the two functionals, as shown in Figure A.4. The blue colour of the isosurfaces, representing the excess of density calculated by PBE with respect to B3LYP, can be seen between the S atoms. In this figure, the geometry optimized with B3LYP is shown, however no substantial difference can be observed for the charge density difference on the geometry optimized with PBE (not shown).

We also compared the vibrational spectra of sMoDTC calculated with the PBE and the B3LYP functionals. The comparison is shown in Figure A.5. While most features are very similar in the simulated vibrational spectra, the major discrepancy is the shift to higher frequencies of the peaks obtained with B3LYP. Such shift is more important for high-frequency vibrations rather than low-frequency vibrations, as it reaches approximately 70 cm^{-1} for the C-H vibrations at around 3000 cm^{-1}. The intensity of the corresponding peaks is also slightly affected by the change of the functional. As shown in the comparison between experimental and simulated spectra in the main text, in reality the vibrational peaks are found at lower frequency than in the simulation. Therefore, the PBE functional was chosen to simulate the spectra of all the compounds, as it reproduces slightly more faithfully the features of the experimental spectra, despite providing a different energy ordering for the chemical structures.

A.3.3 Energy difference between substituted compounds and sMoDTC

We complete the comparison between QE and Gaussian (PBE) by showing the calculated energy differences between the substituted compounds, including the oxygen-free complex, and sMoDTC, as reported in Equation 3 of the main text. The chemical structures taken into account with three and four oxygen atoms can be viewed in Figure 6 of the main text. The results, summarized in Table A.4, confirm the higher stability of oxidized compounds, despite the significant discrepancy in the energy differences for

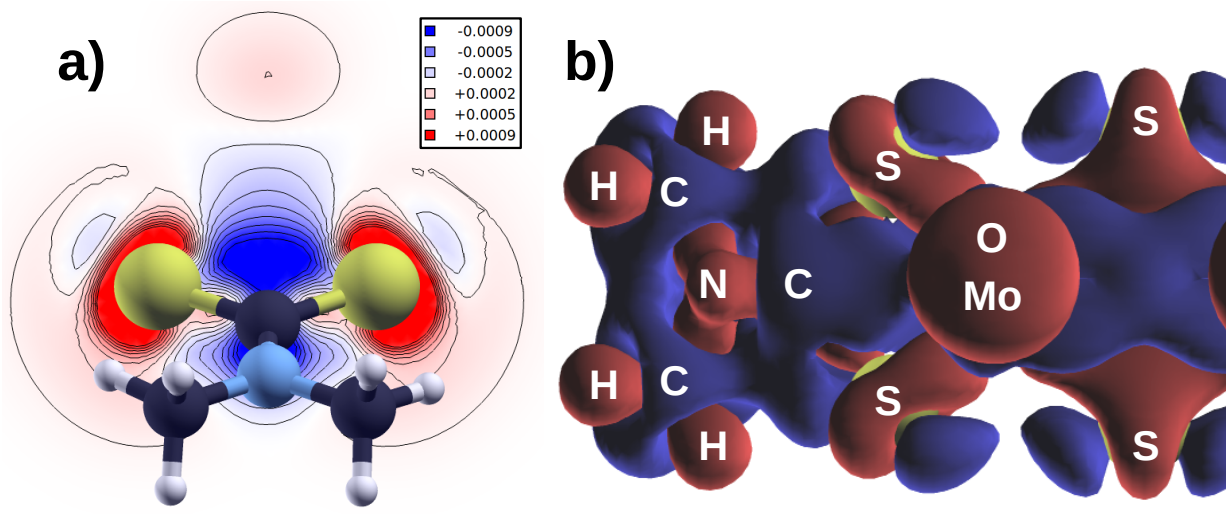


Figure A.4: Charge density difference between PBE and B3LYP. The blue (red) colour is associated to an excess of charge density calculated by PBE (B3LYP). a) Plot of the density difference on a YZ plane passing through S atoms in ligand position. The isovalues of the plot are shown in legend in units of charge. b) Top view of the 3D isosurface of the charge density difference plotted with an isovalue of 0.0004 units of charge.

each compound. Such discrepancy may arise because the values of $E_{ads,S}$ and $E_{ads,O}$ were not calculated with Gaussian. As seen with the isomers, the energy ordering of the chemical structures with the same number of oxygen atoms changes from QE to Gaussian for the reasons explained previously.

A.4 Partial charges

Here we report the complete charge analysis, including both the Bader and the Löwdin techniques. The partial charges on the Mo atoms were calculated as $\Delta\rho = \rho_{\text{Complex}} - \rho_{\text{sMoDTC}}$, where $\rho_{\text{sMoDTC}} = -12.32\,e$, as reported in the main text.

A.5 Experimental IR spectrum of MoDTC

The experimental infrared spectrum of MoDTC presented in Figure 9 of the main text was provided by Total Marketing and Services. The spectrum was recorded with a Nicolet iS50FT-IR spectrometer in the range 400-4000 cm^{-1} with a resolution of 4 cm^{-1} and a DTGS detector. The sample, containing a mixture of MoDTC structures with butyl chains in the carbamate units, was measured without prior preparation, by employing the ATR press.

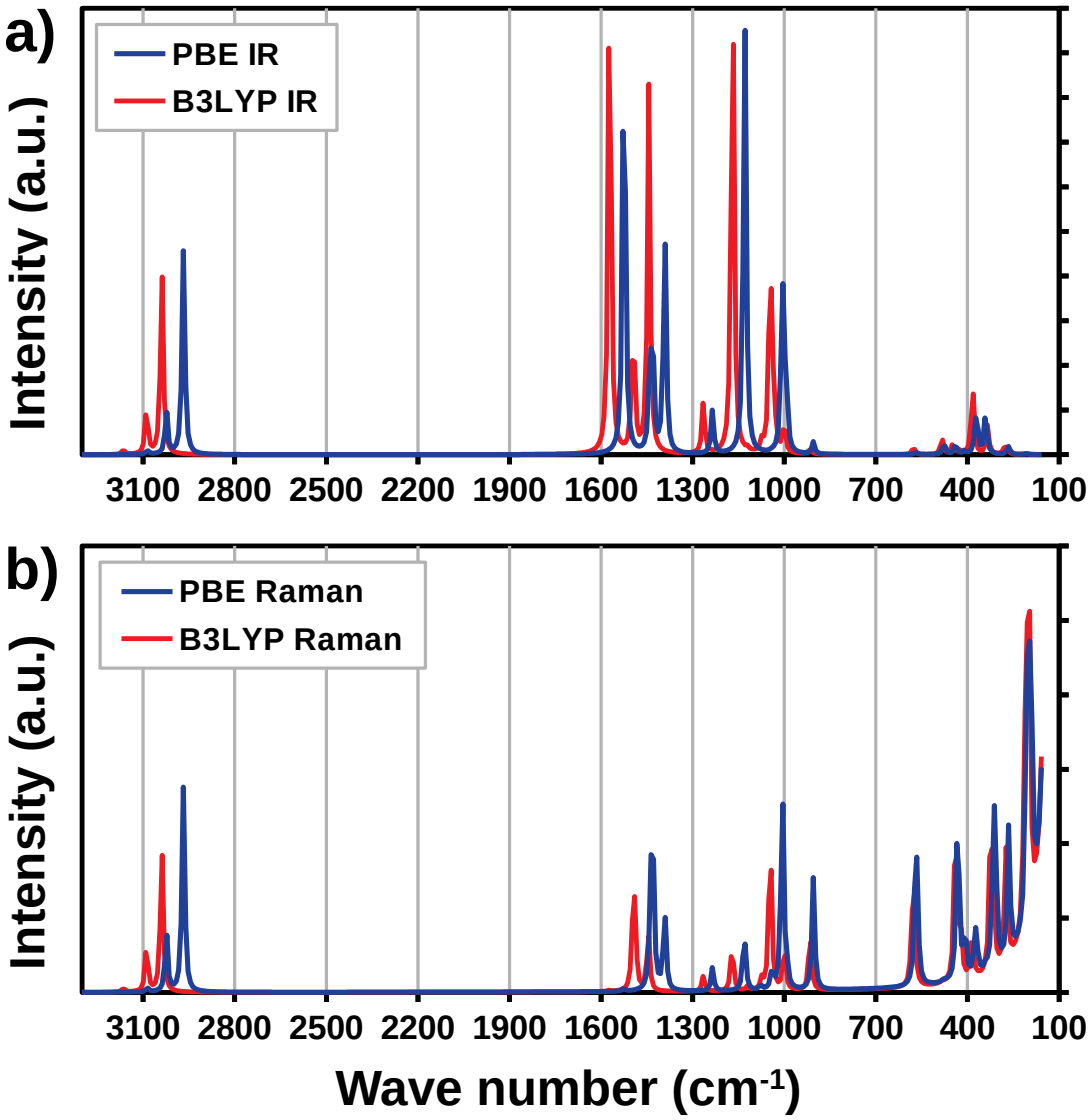


Figure A.5: a) IR and b) Raman spectra of sMoDTC calculated with the PBE (blue) and the B3LYP (red) functionals. No shift nor scaling were performed on the spectra.

Table A.4: Energy differences in eV between the substituted compounds and sMoDTC.

Substitution	Quantum ESPRESSO	Gaussian PBE
Substitution a	-2.47	-4.86
Substitution b	-3.08	-5.44
Substitution c	-3.15	-5.42
Substitution d	-3.16	-5.32
Substitution e	-3.19	-5.44
Substitution f	-5.65	-10.33
Substitution g	-5.66	-10.21
Substitution h	-5.68	-10.35
Substitution i	-6.20	-10.94
Substitution j	-6.20	-10.85
Substitution k	-6.20	-10.84
Substitution l	-6.27	-10.80
OfMoDTC	6.01	11.03

Table A.5: Partial charges on Mo atoms. The structures in the table are represented in Figures 5 and 6 of the main text.

Structure	Löwdin		Bader	
	Mo 1 (e)	Mo 2 (e)	Mo 1 (e)	Mo 2 (e)
Substitution j	-0.35	0.22	-0.21	0.19
Substitution e	-0.35	0.39	-0.21	0.29
Substitution a	-0.22	-0.22	-0.16	-0.16
Substitution f	-0.20	-0.20	-0.11	-0.13
Isomer a	-0.06	-0.07	-0.03	-0.04
Substitution l	0.04	0.03	0.08	0.08
Substitution d	0.04	0.22	0.08	0.19
Isomer h	0.04	0.39	0.09	0.29
Isomer f	0.22	0.00	0.18	0.01

Appendix B

Supporting Information for: Tribochemical Reactions of MoDTC Lubricant Additives with Iron by Quantum Mechanics/Molecular Mechanics Simulations

B.1 Preparation of the QM/MM systems

The initial geometry of the two systems simulated with the QM/MM approach was obtained by first adsorbing two MoDTC complexes (sMoDTC in Simulation A, Substitution L in Simulation B) on an iron [110] bilayer. The lateral cell dimensions were $7 \times 3\sqrt{2}$ times the lattice parameter of the iron bulk [146], while the height of the cell was approximately 20 Å to avoid interaction with the vertical periodic replicas. After chemisorption of the complexes on the metallic substrates, a variable-cell calculation was performed where a load of 2 GPa was applied along the z axis of the supercell. In this way, the iron bilayer of the periodic replica above the simulation cell was forced to approach the chemisorbed complex, creating an interface under load. Only the z axis was allowed to resize during the simulation. The results of the variable-cell calculations were taken to build the QM/MM cells and the remaining iron layers were subsequently added to create 8-layered iron slabs.

B.2 Cutoff for the kinetic energy of the wave functions

The cutoff for the kinetic energy of the wave functions in these calculations was chosen as 30 Ry to ensure an accurate description of the iron bulk while maintaining the electronic structure minimization cycles computationally affordable. In a previous publication, we showed that the errors on the lattice parameter, bulk modulus and magnetic moment of the iron bulk calculated with this setup are 0.5%, 5.3% and -3.2%, respectively, compared to the experimental values [146]. The energy difference between sMoDTC and one of its isomers calculated at 30 and 35 Ry differ by 8.6×10^{-4} eV per atom [167], which is reasonably low to consider the chosen value of the kinetic energy cutoff at convergence for our desired accuracy. The charge density cutoff was then set as eight times the value of the kinetic energy cutoff.

B.3 Details on the dissociation of MoDTC complexes on iron

In a recent publication from our group we estimated the strength of the different bonds in the MoDTC complex by calculating the energy difference between two fragments and the whole structure [167]. To estimate such strength, the total energy of the fragments was evaluated by keeping their geometry fixed in the same position as they were in the entire complex. In this study, however, we are interested in the stabilization of the fragments due to the presence of the metallic substrate. Therefore, we let the fragments freely relax on iron in order to fully take into account the effect of the reactive surface. Our intention was

to compare the energy values corresponding to the dissociation of the complexes on the iron surface with the ones required to break bonds in isolated MoDTC structures.

By considering sMoDTC, Isomer H and Substitution L, a wide variety of molecular fragments can be generated by dissociating these compounds on iron. The overall dissociation can be divided in two steps. First, one of the two DTC units is detached, then the remaining DTC unit is detached. A general schematic representation of these two steps could be:

$$ABC \rightarrow A + BC \tag{B.1}$$

$$BC \rightarrow B + C \tag{B.2}$$

where A, B and C correspond to the first detached DTC unit, the central unit and the second detached DTC, respectively. ABC and BC are the entire MoDTC complex and the central unit with the second DTC unit still attached, respectively. Therefore, we calculated the fragmentation energies of the two steps, $E_{frag,1}$ and $E_{frag,2}$, resulting from the two dissociative patterns, namely Cut 1 and Cut 3, for the three complexes:

$$E_{frag,1} = E_{A,iron} + E_{BC,iron} - E_{ABC,iron} - E_{iron} \tag{B.3}$$

$$E_{frag,2} = E_{B,iron} + E_{C,iron} - E_{BC,iron} - E_{iron} \tag{B.4}$$

where $E_{X,iron}$ are the total energies of the X species adsorbed on iron (X = A, B, C, BC, ABC) and E_{iron} is the total energy of the pristine iron slab. The total energy of the iron slab must be substracted in the *r.h.s.* of Equations B.3 and B.4 in order to balance the number of iron atoms in the equations. The resulting fragmentation energies include the contribution required to break the bonds of the complex as well as the stabilization arising from the new bonds formed between the adsorbates and the iron atoms.

Appendix C

Reorganization of central units of MoDTC to form amorphous MoS_x

We employed density functional theory (DFT) to simulate the tribochemical transformation of the central units of MoDTC to form an amorphous MoS_x structure in different steps, taking into account the effect of oxygen. Firstly, we performed static calculations of the central units under load to monitor how compression can destabilize the geometry of these molecular fragments. Dynamic calculations, following the scheme of quantum mechanics/molecular mechanics (QM/MM) [87, 88], were then performed to introduce the effect of temperature and shear stress on the destabilized central units. We also explored the role of oxygen in the central units of MoDTC, as it is known that the presence of oxygen does not necessarily prevent the formation of MoS_2 layers [179], yet O atoms modify the morphology and composition of the layers of this solid lubricant [173].

C.1 Methods and Systems

The ab initio calculations were carried out by employing the Quantum ESPRESSO suite [128], following the same computational scheme adopted in our previous works.

Twelve central units of MoDTC, enclosed by two crystalline MoS_2 layers, were put inside a periodic $5x3\sqrt{3}$ cell with respect to the unit cell of MoS_2, with the cell dimensions being $16.62 \times 15.99 \times 33.59$, expressed in Å. Such a cell height ensure at least 15 Å of vacuum to separate the periodic replicas. Two different kinds of central units were considered: in one group of simulations central units containing only molybdenum and sulfur were considered, while in a second group central units with two oxygen atoms in terminal position were considered. To simulate a compressive stress on the central units of MoDTC, external forces were imposed on the molybdenum atoms of the crystalline MoS_2 layers. The initial load experienced by the central units was 10 GPa. After the first geometry optimization, the load was increased to 20 and then 40 GPa.

To introduce the effect of shear on the compressed central units, we carried out dynamic calculations following the QM/MM approach already described in detail previously. Three QM/MM simulations were carried out depending on the type of central units in the system and their interaction with the external crystalline layers:

- A: Central units containing only Mo and S atoms
- B: Central units containing also O atoms. The interactions between the oxygen atoms and the external MoS_2 layers were described by an attractive Lennard-Jones potential
- C: Central units containing also O atoms. The interactions between the oxygen atoms and the external MoS_2 layers were described by a repulsive Lennard-Jones potential

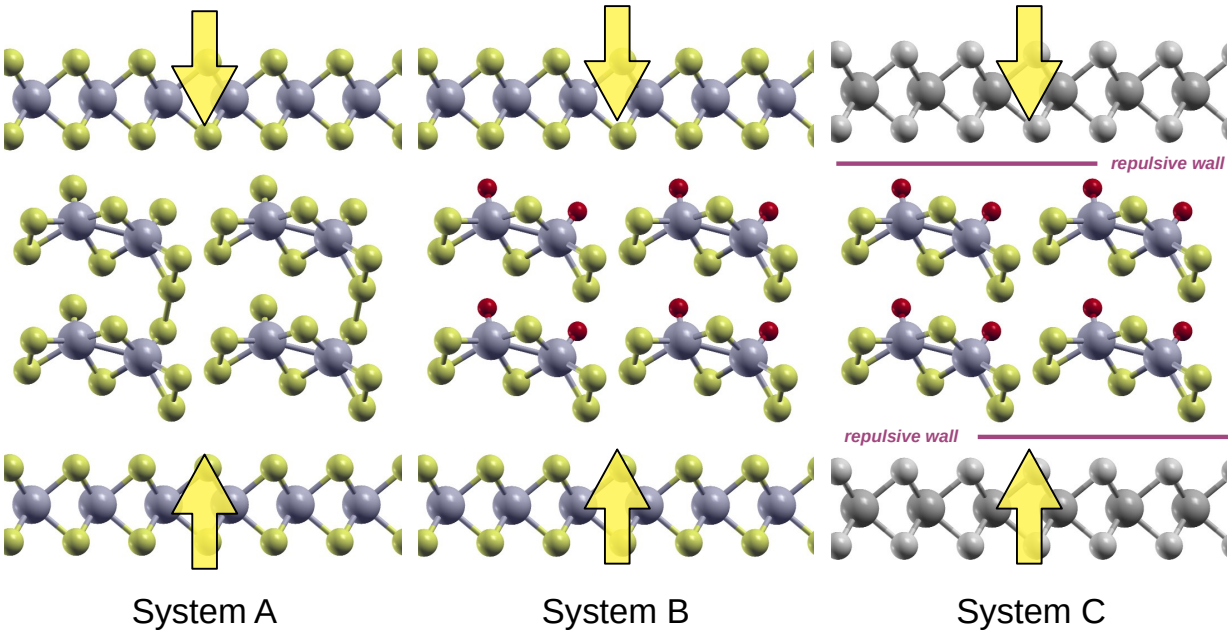


Figure C.1: Lateral views of the initial configurations containing the central units of MoDTC with only sulfur atoms (left, System A) and with oxygen atoms (middle and right, Systems B and C, respectively). The yellow arrows indicate the presence of load, while the purple lines in System C indicate that the outer MoS_2 layers interact with the oxygen atoms merely as repulsive walls.

In order to qualitatively describe the interaction between the oxygen atoms in the quantum region and the classical molybdenum and sulfur atoms, Lennard-Jones potentials were employed. The attractive potential was parametrized according to the values reported in literature for Mo, S [206] and O atoms [207] and the values of ϵ for the different species were multiplied by 2 in order to enhance the stability of the Mo-O and S-O interactions. The parameters for both the attractive and repulsive Lennard-Jones potentials for the O-S and O-Mo interactions are reported in Table C.1.

Selecting different potentials to describe the interactions of O atoms with the external layers in Systems B and C allowed to investigate the behavior of the oxygen in two different environments and to describe the diffusion of the O atoms in the central layer independently of the chemistry of the external layers. The interactions between the Mo and S atoms of the central units and the external MoS_2 layers were described by the REBO-MoS_2 potential by Liang et al. [208, 209] in all the systems. An initial thermalization process, lasted one picosecond, allowed the system to globally reach 300 K by employing a Nosé-Hoover thermostat with a damping parameter of 33.3 fs. An ensemble of velocities for all the atoms was generated from a Gaussian distribution with a standard deviation scaled to produce the temperature of 300 K. After the thermalization process, the temperature of the chemically reactive region was left free to evolve and, in order to simulate the sliding of the surfaces, a shear motion of the top iron slab was applied on the Mo atoms of the external layers, with velocity kicks of 600 m/s applied at the first and second picosecond, of 800 m/s at the third and fourth picosecond, and of 1000 m/s onwards. Such high values of shear speed were chosen to counteract the huge values of friction originated by the very high load. The timestep of

Table C.1: Parameters for the attractive and repulsive Lennard-Jones potentials describing the O-S and O-Mo interactions. ϵ and σ are expressed in eV and angstrom, respectively.

	ϵ_{O-S}	σ_{O-S}	ϵ_{O-Mo}	σ_{O-Mo}
Attractive	3.148	0.0197654198	3.683	0.00406400943
Repuslive	0.0002535	4.0264	0.0002535	4.0264

the simulation was 1 fs. The central units experienced a load of 40 GPa for the whole duration of the simulation.

C.2 Results

Figure C.1 shows the initial configurations of the systems containing the central units of MoDTC enclosed by two MoS_2 layers. The effect of the load destabilized the molecular units, which rearranged their geometry. After reaching 40 GPa, the original geometry of the central units is completely lost, yet the Mo atoms are still clustered in the same locations where the central units were initially positioned. To allow further reorganization, the optimized configurations at 40 GPa were chosen as the initial geometry of the QM/MM dynamic simulations, in which the effect of temperature and the shear motion along the y direction were introduced. All the atoms from the central units were treated at the quantum level, while the atoms of the external MoS_2 layers were treated by means of classical molecular mechanics. A schematic representation of the QM/MM partitioning is shown in Figure C.2.

It is instructive to compare the density of Mo, S and O atoms along the three axes at the beginning of the simulation and after 4 ps. Initially, the atoms are found at specific positions, even in the presence of a displacement caused by the very high load, and the density plots are characterized by clear peaks. After 4 ps, most of the atoms are displaced. This is particularly evident in the plots relative to the z axis, shown in Figure C.3, where in all the systems the Mo atoms tend to move towards the center of the inner layer, while S and O atoms tend to diffuse to the outside. This phenomenon is an inherent feature of the inner layer, and is mainly due to the tendency of Mo atoms to reach a high coordination. Oxygen, in fact, always tends to reach the end of the inner layer, even when a repulsion is imposed between the external MoS_2 layers and the O atoms (System C). This geometric arrangement can be achieved even in the presence of high loads and is independent of the chemical nature of the substrates. S and O atoms in excess in the amorphous layer may be seized by a clean metallic substrate through this diffusion mechanism, allowing the amorphous layer to reach the correct stoichiometry to form crystalline MoS_2.

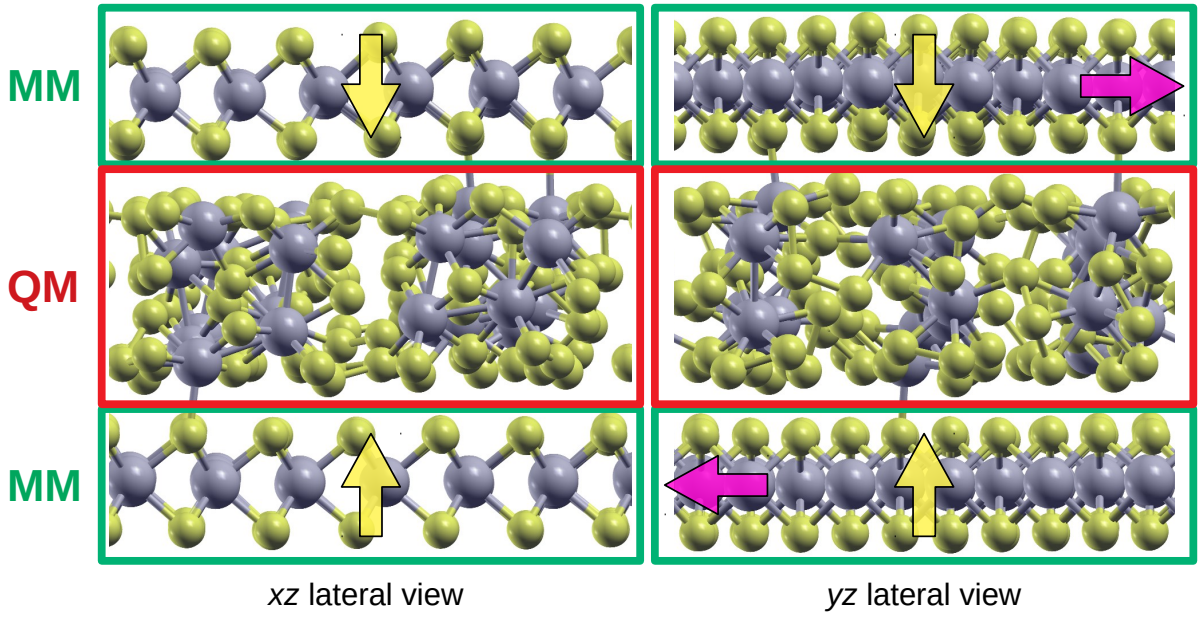


Figure C.2: Lateral views of the initial configuration of the QM/MM system with only sulfur atoms in the central units, as an example. Both the xz and the yz orientations are shown. Yellow and purple arrows identify load and shear, respectively.

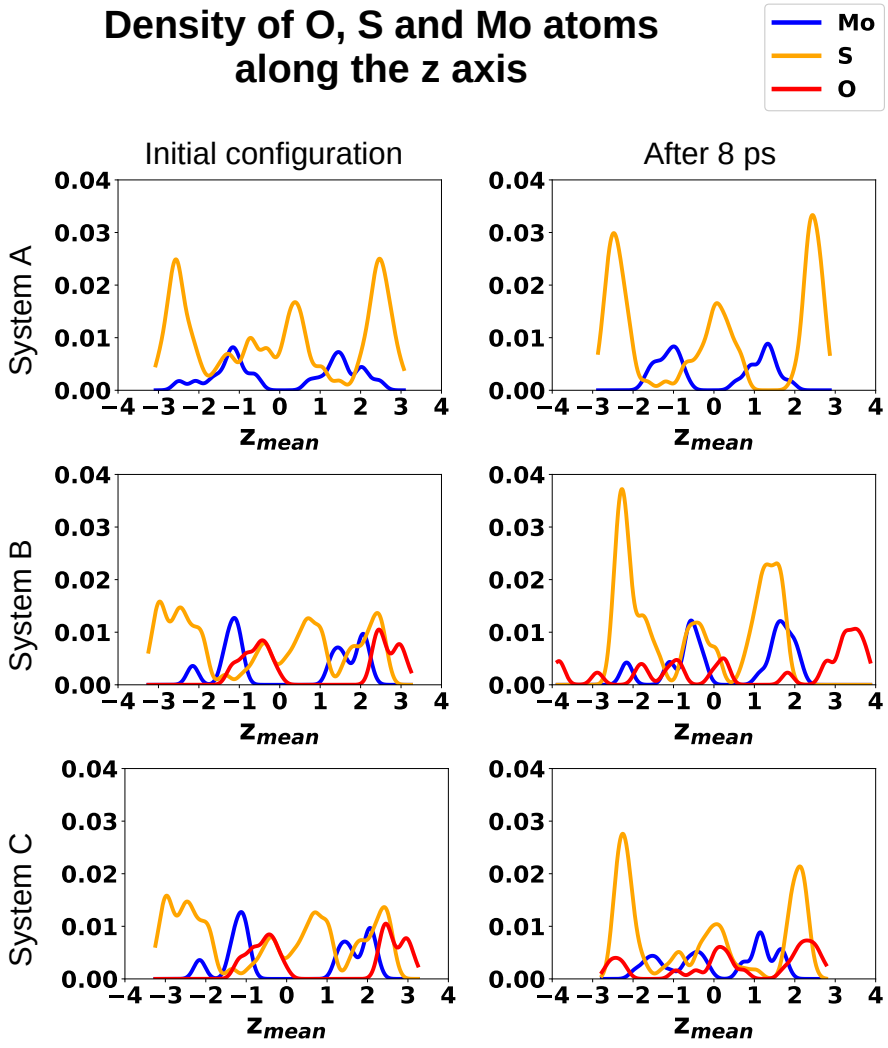


Figure C.3: Densities of O (red), S (yellow) and Mo (blue) atoms along the z axis of the cell during the QM/MM simulations.

Appendix D

Supporting Information for: Experimental and Ab-Initio Characterization of Mononuclear Molybdenum Dithiocarbamates in Lubricant Mixtures

D.1 Concentration of sulfur and molybdenum in the collected fractions

Table D.1 reports the concentrations of sulfur and molybdenum in most of the collected fractions obtained by the separation of S525. Fractions 7, 8 and 9 are the most concentrated in terms of product, as they showcase the highest sulfur and molybdenum concentration. The values of Mo/S ratio reported in Table D.1 can be compared with the ideal Mo/S ratio in individual MoDTC structures shown in Table D.2.

Table D.1: Concentrations of sulfur and molybdenum in the collected fractions.

Fraction	S (ppm)	Mo (ppm)	Mo/S ratio %
5	0.0	<5	N/A
6	32.9	26.8	81.4
7	456.3	392.6	86.0
8	415.5	402.2	96.8
9	434.3	432.0	99.5
10	32.9	31.4	95.4
11	20.4	15.6	76.5
17	42.8	29.7	69.4

D.2 Electronic spectra

Figure D.1 shows the electronic spectra of Fractions 7, 8 and 9. In the UV range, the differences between the fractions are small, although still detectable, while an increased absorption can be detected between 500-700 nm for Fraction 9, justifying the lack of the green color observed in the other samples.

Table D.2: Mo/S mass ratio in individual MoDTC compounds. In the columns labelled as "#O-#S", the first (second) number corresponds to the number of O (S) atoms in the chemical structures.

Mononuclear (1 Mo)		Binuclear (2 Mo)	
#O-#S	Mo/S ratio %	#O-#S	Mo/S ratio %
0-5	59.8	0-8	74.8
1-4	74.8	1-7	85.5
2-3	99.7	2-6	99.7
3-2	149.6	3-5	119.7
4-1	299.2	4-4	149.6
		5-3	199.4
		6-2	299.2
		7-1	598.5

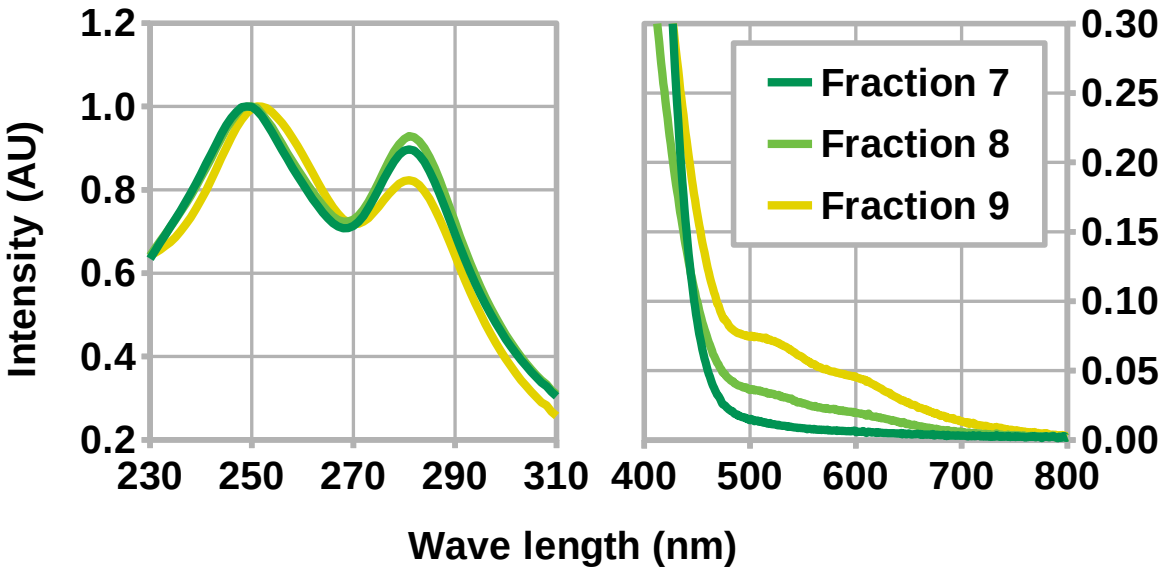


Figure D.1: UV (left) and visible (right) spectra of Fractions 7, 8 and 9. The intensity of the UV peaks at 250 nm was normalized, while the visible spectra were not scaled.

Appendix E

Supporting Information for: Adsorption and Dissociation of $Ni(acac)_2$ on Iron by Ab Initio Calculations

E.1 Convergence test

In order to choose a proper value for the cutoff on the kinetic energy of the wave functions, a convergence test was carried out by taking into account the ionization energy of the molecule, which is a property directly comparable with the data available in literature. The ionization energy was calculated at different energy cutoffs according to Equation 1 in the main text. The ionization energy was found at convergence below 0.3 meV/atom for a cutoff of 35 Ry, as shown in Table E.1 in the present document. A plot of the convergence test is shown in Figure E.1 in the present document.

E_{cut}	E_i	ΔE_i
25	6.380726083	0.00451
35	**6.250050137**	**0.00022**
45	6.243631648	0.00001
55	6.243631648	0.00010
65	6.240372947	

Table E.1: Kinetic energy cutoffs (E_{cut}) in Ry, ionization energies (E_i) in eV and the differences in ionization energies between two adjacent lines (ΔE_i) in $eV/atom$.

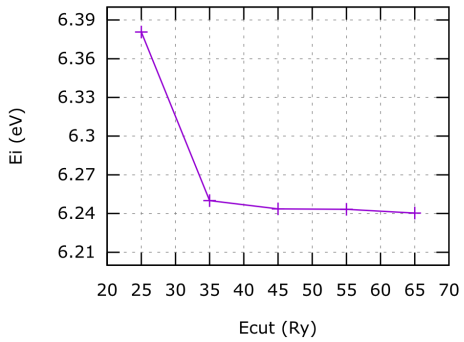


Figure E.1: Ionization energy values (eV) calculated at different kinetic energy cutoffs (Ry).

Bibliography

1. Holmberg, K. & Erdemir, A. Global impact of friction on energy consumption, economy and environment. *FME Transactions* **43,** 181–185 (2015).
2. Holmberg, K. & Erdemir, A. Influence of Tribology on Global Energy Consumption, Costs and Emissions. *Friction* **5,** 263–284. https://doi.org/10.1007/s40544-017-0183-5 (2017).
3. Yamamoto, Y. & Gondo, S. Friction and Wear Characteristics of Molybdenum Dithiocarbamate and Molybdenum Dithiophosphate. *Tribology Transactions* **32,** 251–257. https://doi.org/10.1080/10402008908981886 (1989).
4. Hähner, G. & Spencer, N. Rubbing and Scrubbing. *Physics Today* **51,** 22–27. https://physicstoday.scitation.org/doi/10.1063/1.882435 (1998).
5. Coulomb, C. *Théorie des machines simples en ayant égard au frottement de leurs parties et à la roideur des cordages* (Bachelier, 1821).
6. Reynolds, O. IV. On the theory of lubrication and its application to Mr. Beauchamp tower's experiments, including an experimental determination of the viscosity of olive oil. *Philosophical Transactions of the Royal Society of London* **177,** 157–234. https://royalsocietypublishing.org/doi/abs/10.1098/rstl.1886.0005 (1886).
7. Stribeck, R. *Kugellager für beliebige Belastungen* (Springer, 1901).
8. Stribeck, R. *Die wesentlichen Eigenschaften der Gleit- und Rollenlager* (Julius Springer, 1903).
9. Bowden, F. & Tabor, D. *The Friction and Lubrication of Solids International series of monographs on physics* **1.** ISBN: 9780198507772 (Clarendon Press, 2001).
10. Tabor, D. & Winterton, R. H. S. The direct measurement of normal and retarded van der Waals forces. *Proceedings of the Royal Society of London. A. Mathematical and Physical Sciences* **312,** 435–450. https://royalsocietypublishing.org/doi/abs/10.1098/rspa.1969.0169 (1969).
11. Israelachvili, J. N. & Tabor, D. The measurement of van der Waals dispersion forces in the range 1.5 to 130 nm. *Proceedings of the Royal Society of London. A. Mathematical and Physical Sciences* **331,** 19–38. https://royalsocietypublishing.org/doi/abs/10.1098/rspa.1972.0162 (1972).
12. Binnig, G., Quate, C. F. & Gerber, C. Atomic Force Microscope. *Phys. Rev. Lett.* **56,** 930–933. https://link.aps.org/doi/10.1103/PhysRevLett.56.930 (1986).
13. Carpick, R. W. & Salmeron, M. Scratching the Surface: Fundamental Investigations of Tribology with Atomic Force Microscopy. *Chemical Reviews* **97,** 1163–1194. https://doi.org/10.1021/cr960068q (1997).
14. Szlufarska, I., Chandross, M. & Carpick, R. W. Recent advances in single-asperity nanotribology. *Journal of Physics D: Applied Physics* **41,** 123001. https://doi.org/10.1088%5C%2F0022-3727%5C%2F41%5C%2F12%5C%2F123001 (2008).
15. Hirano, M. & Shinjo, K. Atomistic locking and friction. *Phys. Rev. B* **41,** 11837–11851. https://link.aps.org/doi/10.1103/PhysRevB.41.11837 (1990).

16. Hofmann, F. & Toennies, J. P. High-Resolution Helium Atom Time-of-Flight Spectroscopy of Low-Frequency Vibrations of Adsorbates. *Chemical Reviews* **96,** 1307–1326. https://doi.org/10.1021/cr9502209 (1996).

17. Weber, R. E. & Peria, W. T. Use of LEED Apparatus for the Detection and Identification of Surface Contaminants. *Journal of Applied Physics* **38,** 4355–4358. https://doi.org/10.1063/1.1709128 (1967).

18. Palmberg, P. & Peria, W. Low energy electron diffraction studies on Ge and Na-covered Ge. *Surface Science* **6,** 57–97. http://www.sciencedirect.com/science/article/pii/0039602867900155 (1967).

19. Atkinson, S. J., Brundle, C. R. & Roberts, M. W. Ultra-violet and X-ray photoelectron spectroscopy (UPS and XPS) of CO, CO2, O2 and H2O on molybdenum and gold films. *Faraday Discuss. Chem. Soc.* **58,** 62–79. http://dx.doi.org/10.1039/DC9745800062 (1974).

20. Adams, H. *et al.* Modeling Mechanochemical Reaction Mechanisms. *ACS Applied Materials & Interfaces* **9,** 26531–26538. https://doi.org/10.1021/acsami.7b05440 (2017).

21. Dong, Y., Li, Q. & Martini, A. Molecular dynamics simulation of atomic friction: A review and guide. *Journal of Vacuum Science & Technology A* **31,** 030801. https://doi.org/10.1116/1.4794357 (2013).

22. Takacs, L. M. Carey Lea, the first mechanochemist. *Journal of Materials Science* **39,** 4987–4993. https://doi.org/10.1023/B:JMSC.0000039175.73904.93 (2004).

23. Ostwald, W. & Drucker, C. *Handbuch der allgemeinen Chemie* **1** (Akademische Verlagsgesellschaft, 1919).

24. Friščić, T., Mottillo, C. & Titi, H. M. Mechanochemistry for Synthesis. *Angewandte Chemie International Edition* **59,** 1018–1029. https://onlinelibrary.wiley.com/doi/abs/10.1002/anie.201906755 (2020).

25. Fischer, T. E. Tribochemistry. *Annual Review of Materials Science* **18,** 303–323. https://doi.org/10.1146/annurev.ms.18.080188.001511 (1988).

26. Zhurkov, S. N. Kinetic concept of the strength of solids. *International Journal of Fracture* **26,** 295–307. https://doi.org/10.1007/BF00962961 (1984).

27. Jacobs, T. D. B. & Carpick, R. W. Nanoscale wear as a stress-assisted chemical reaction. *Nature Nanotechnology* **8,** 108–112. https://doi.org/10.1038/nnano.2012.255 (2013).

28. Felts, J. R. *et al.* Direct mechanochemical cleavage of functional groups from graphene. *Nature Communications* **6,** 6467. https://doi.org/10.1038/ncomms7467 (2015).

29. Willermet, P., Dailey, D., Carter, R., Schmitz, P. & Zhu, W. Mechanism of formation of antiwear films from zinc dialkyldithiophosphates. *Tribology International* **28,** 177–187. http://www.sciencedirect.com/science/article/pii/0301679X9598965G (1995).

30. Somayaji, A. & Aswath, P. B. The Role of Antioxidants on the Oxidation Stability of Oils with F-ZDDP and ZDDP, and Chemical Structure of Tribofilms Using XANES. *Tribol. T.* **52,** 511–525. https://doi.org/10.1080/10402000902745499 (2009).

31. Liping, W., Dongya, Z., Hongxing, W., Youbai, X. & Guangneng, D. Effects of phosphorus-free antioxidants on oxidation stability and high-temperature tribological properties of lubricants. *Proceedings of the Institution of Mechanical Engineers, Part J: Journal of Engineering Tribology* **231,** 1527–1536. https://doi.org/10.1177/1350650117700343 (2017).

32. Suzuki, A., Ulfiati, R. & Masuko, M. Evaluation of antioxidants in rapeseed oils for railway application. *Tribology International* **42,** 987–994. http://www.sciencedirect.com/science/article/pii/S0301679X09000231 (2009).

33. Polcar, T., Kubart, T., Novák, R., Kopecký, L. & Široký, P. Comparison of tribological behaviour of TiN, TiCN and CrN at elevated temperatures. *Surface and Coatings Technology* **193,** 192–199. http://www.sciencedirect.com/science/article/pii/S0257897204005444 (2005).

34. Papay, A. G. Antiwear and extreme-pressure additives in lubricants. *Lubrication Science* **10,** 209–224. https://onlinelibrary.wiley.com/doi/abs/10.1002/ls.3010100304 (1998).

35. Righi, M. C. in *Advanced Analytical Methods in Tribology* (eds Dienwiebel, M. & De Barros Bouchet, M.-I.) 309–323 (Springer International Publishing, 2018). https://doi.org/10.1007/978-3-319-99897-8_12.

36. Ronkainen, H., Likonen, J., Koskinen, J. & Varjus, S. Effect of tribofilm formation on the tribological performance of hydrogenated carbon coatings. *Surface and Coatings Technology* **79,** 87–94. ISSN: 0257-8972. http://www.sciencedirect.com/science/article/pii/0257897295024336 (1996).

37. Equey, S. *et al.* Tribofilm formation from ZnDTP on diamond-like carbon. *Wear* **264,** 316–321. http://www.sciencedirect.com/science/article/pii/S004316480700498X (2008).

38. Erdemir, A. *et al.* Carbon-based Tribofilms from Lubricating Oils. *Nature* **536,** 67–71. https://doi.org/10.1038/nature18948 (2016).

39. Johnson, B. *et al.* Direct Formation of Lubricious and Wear-Protective Carbon Films from Phosphorus- and Sulfur-Free Oil-Soluble Additives. *Tribology Letters* **66,** 2. https://doi.org/10.1007/s11249-017-0945-2 (2017).

40. Ramirez, G. *et al.* Tribochemical Conversion of Methane to Graphene and Other Carbon Nanostructures: Implications for Friction and Wear. *ACS Applied Nano Materials* **3,** 8060–8067. https://doi.org/10.1021/acsanm.0c01527 (2020).

41. McDevitt, N., Donley, M. & Zabinski, J. Utilization of Raman spectroscopy in tribochemistry studies. *Wear* **166,** 65–72. http://www.sciencedirect.com/science/article/pii/004316489390280Y (1993).

42. Mangolini, F., Rossi, A. & Spencer, N. D. Tribochemistry of Triphenyl Phosphorothionate (TPPT) by In Situ Attenuated Total Reflection (ATR/FT-IR) Tribometry. *The Journal of Physical Chemistry C* **116,** 5614–5627. https://doi.org/10.1021/jp209697a (2012).

43. Martin, J., Le Mogne, T., Boehm, M. & Grossiord, C. Tribochemistry in the analytical UHV tribometer. *Tribology International* **32,** 617–626. http://www.sciencedirect.com/science/article/pii/S0301679X99000900 (1999).

44. Wakabayashi, T., Williams, J. A. & Hutchings, I. M. The Kinetics of Gas-Phase Lubrication in the Orthogonal Machining of an Aluminium Alloy. *Proceedings of the Institution of Mechanical Engineers, Part J: Journal of Engineering Tribology* **209,** 131–136. https://doi.org/10.1243/PIME_PROC_1995_209_415_02 (1995).

45. Philippon, D., de Barros-Bouchet, M.-I., Mogne, T. L., Gresser, E. & Martin, J.-M. Experimental simulation of phosphites additives tribochemical reactions by gas phase lubrication. *Tribology - Materials, Surfaces & Interfaces* **1,** 113–123. https://doi.org/10.1179/175158408X273586 (2007).

46. Righi, M. C., Loehlé, S., de Barros Bouchet, M. I., Philippon, D. & Martin, J. M. Trimethyl-phosphite dissociative adsorption on iron by combined first-principle calculations and XPS experiments. *RSC Adv.* **5,** 101162–101168. http://dx.doi.org/10.1039/C5RA14446A (2015).

47. De Barros-Bouchet, M. I. *et al.* Tribochemistry of phosphorus additives: experiments and first-principles calculations. *RSC Adv.* **5,** 49270–49279. http://dx.doi.org/10.1039/C5RA00721F (2015).

48. Righi, M. C., Loehlé, S., De Barros Bouchet, M. I., Mambingo-Doumbe, S. & Martin, J. M. A comparative study on the functionality of S- and P-based lubricant additives by combined first principles and experimental analysis. *RSC Adv.* **6,** 47753–47760. http://dx.doi.org/10.1039/C6RA07545B (2016).

49. Strawhecker, K., Asay, D. B., McKinney, J. & Kim, S. H. Reduction of adhesion and friction of silicon oxide surface in the presence of n-propanol vapor in the gas phase. *Tribology Letters* **19,** 17–21. https://doi.org/10.1007/s11249-004-4261-2 (2005).

50. De Barros Bouchet, M.-I. & Martin, J.-M. in *Advanced Analytical Methods in Tribology* (eds Dienwiebel, M. & De Barros Bouchet, M.-I.) 107–128 (Springer International Publishing, 2018). ISBN: 978-3-319-99897-8. https://doi.org/10.1007/978-3-319-99897-8_4.

51. De Barros Bouchet, M.-I. *et al.* Friction of Diamond in the Presence of Water Vapor and Hydrogen Gas. Coupling Gas-Phase Lubrication and First-Principles Studies. *The Journal of Physical Chemistry C* **116,** 6966–6972. https://doi.org/10.1021/jp211322s (2012).

52. Tersoff, J. New empirical approach for the structure and energy of covalent systems. *Phys. Rev. B* **37,** 6991–7000. https://link.aps.org/doi/10.1103/PhysRevB.37.6991 (1988).

53. Tersoff, J. Empirical interatomic potential for silicon with improved elastic properties. *Phys. Rev. B* **38,** 9902–9905. https://link.aps.org/doi/10.1103/PhysRevB.38.9902 (1988).

54. Brenner, D. W. Relationship between the embedded-atom method and Tersoff potentials. *Phys. Rev. Lett.* **63,** 1022–1022. https://link.aps.org/doi/10.1103/PhysRevLett.63.1022 (1989).

55. Brenner, D. W. Erratum: Empirical potential for hydrocarbons for use in simulating the chemical vapor deposition of diamond films. *Phys. Rev. B* **46,** 1948–1948. https://link.aps.org/doi/10.1103/PhysRevB.46.1948.2 (1992).

56. Stuart, S. J., Tutein, A. B. & Harrison, J. A. A reactive potential for hydrocarbons with intermolecular interactions. *The Journal of Chemical Physics* **112,** 6472–6486. https://doi.org/10.1063/1.481208 (2000).

57. Van Duin, A. C. T., Dasgupta, S., Lorant, F. & Goddard, W. A. ReaxFF: A Reactive Force Field for Hydrocarbons. *The Journal of Physical Chemistry A* **105,** 9396–9409. https://doi.org/10.1021/jp004368u (2001).

58. Hohenberg, P. & Kohn, W. Inhomogeneous Electron Gas. *Phys. Rev.* **136,** B864–B871 (1964).

59. Kohn, W. & Sham, L. J. Self-Consistent Equations Including Exchange and Correlation Effects. *Phys. Rev.* **140,** A1133–A1138 (1965).

60. Qi, Y., Yang, J. & Rappe, A. M. Theoretical Modeling of Tribochemical Reaction on Pt and Au Contacts: Mechanical Load and Catalysis. *ACS Applied Materials & Interfaces* **8,** 7529–7535. https://doi.org/10.1021/acsami.5b12350 (2016).

61. Borgoo, A., Tozer, D. J., Geerlings, P. & De Proft, F. Influence of confinement on atomic and molecular reactivity indicators in DFT. *Phys. Chem. Chem. Phys.* **10,** 1406–1410. http://dx.doi.org/10.1039/B716727J (2008).

62. Ta, D. *et al.* Physical and chemical insights into molecular adsorption of copolymer's monomers on Rutile surface. *Chemical Physics* **520,** 8–20. http://www.sciencedirect.com/science/article/pii/S0301010418307365 (2019).

63. Tran, N. V. *et al.* An ab initio study on the effects of Na passivation on friction reduction of an iron oxide surface. *Journal of Applied Physics* **127,** 065305. https://doi.org/10.1063/1.5133078 (2020).

64. Fatti, G. & Righi, M. C. Selenium Chemisorption Makes Iron Surfaces Slippery. *Tribology Letters* **67,** 125. https://doi.org/10.1007/s11249-019-1235-y (2019).

65. Wolloch, M., Levita, G., Restuccia, P. & Righi, M. C. Interfacial Charge Density and Its Connection to Adhesion and Frictional Forces. *Phys. Rev. Lett.* **121,** 026804. https://link.aps.org/doi/10.1103/PhysRevLett.121.026804 (2018).

66. Billes, F., Holmgren, A. & Mikosch, H. A combined DFT and vibrational spectroscopy study of the nickel and zinc O,O-diethyldithiophosphate complexes. *Vibrational Spectroscopy* **53,** 296–306. http://www.sciencedirect.com/science/article/pii/S0924203110000822 (2010).

67. Bezerra da Silva, M., Santos, R. C. R., Freire, P. T. C., Caetano, E. W. S. & Freire, V. N. Vibrational Properties of Bulk Boric Acid 2A and 3T Polymorphs and Their Two-Dimensional Layers: Measurements and Density Functional Theory Calculations. *The Journal of Physical Chemistry A* **122,** 1312–1325. https://doi.org/10.1021/acs.jpca.7b10083 (2018).

68. Coustel, R. *et al.* Vibrational frequencies of hydrogenated silicon carbonitride: A DFT study. *Surface and Coatings Technology* **325,** 437–444. http://www.sciencedirect.com/science/article/pii/S0257897217306205 (2017).

69. Peng, Q., Ji, W. & De, S. Mechanical properties of the hexagonal boron nitride monolayer: Ab initio study. *Computational Materials Science* **56,** 11–17. http://www.sciencedirect.com/science/article/pii/S0927025611006902 (2012).

70. Ghorbanzadeh Ahangari, M., Fereidoon, A., Jahanshahi, M. & Ganji, M. Electronic and mechanical properties of single-walled carbon nanotubes interacting with epoxy: A DFT study. *Physica E: Low-dimensional Systems and Nanostructures* **48,** 148–156. http://www.sciencedirect.com/science/article/pii/S1386947712004985 (2013).

71. Roldan, A., Santos-Carballal, D. & de Leeuw, N. H. A comparative DFT study of the mechanical and electronic properties of greigite Fe3S4 and magnetite Fe3O4. *The Journal of Chemical Physics* **138,** 204712. https://doi.org/10.1063/1.4807614 (2013).

72. Levita, G., Molinari, E., Polcar, T. & Righi, M. C. First-principles comparative study on the interlayer adhesion and shear strength of transition-metal dichalcogenides and graphene. *Phys. Rev. B* **92,** 085434. https://link.aps.org/doi/10.1103/PhysRevB.92.085434 (2015).

73. Wolloch, M., Losi, G., Ferrario, M. & Righi, M. C. High-throughput screening of the static friction and ideal cleavage strength of solid interfaces. *Scientific Reports* **9,** 17062. https://doi.org/10.1038/s41598-019-49907-2 (2019).

74. Kohlhauser, B. *et al.* How to get noWear? - A new take on the design of in-situ formed high performing low-friction tribofilms. *Materials and Design* **190,** 108519. http://www.sciencedirect.com/science/article/pii/S0264127520300526 (2020).

75. Ou, L. & Chen, S. Comparative Study of Oxygen Reduction Reaction Mechanisms on the Pd(111) and Pt(111) Surfaces in Acid Medium by DFT. *The Journal of Physical Chemistry C* **117,** 1342–1349. https://doi.org/10.1021/jp309094b (2013).

76. Catapan, R. C., Oliveira, A. A. M., Chen, Y. & Vlachos, D. G. DFT Study of the Water–Gas Shift Reaction and Coke Formation on Ni(111) and Ni(211) Surfaces. *The Journal of Physical Chemistry C* **116,** 20281–20291. https://doi.org/10.1021/jp302488f (2012).

77. Righi, G., Magri, R. & Selloni, A. H2 Dissociation on Noble Metal Single Atom Catalysts Adsorbed on and Doped into CeO2 (111). *The Journal of Physical Chemistry C* **123,** 9875–9883. https://doi.org/10.1021/acs.jpcc.9b00609 (2019).

78. Righi, G., Magri, R. & Selloni, A. Methane Activation on Metal-Doped (111) and (100) Ceria Surfaces with Charge-Compensating Oxygen Vacancies. *The Journal of Physical Chemistry C* **124,** 17578–17585. https://doi.org/10.1021/acs.jpcc.0c03320 (2020).

79. Levita, G. & Righi, M. C. Effects of Water Intercalation and Tribochemistry on MoS_2 Lubricity: An Ab Initio Molecular Dynamics Investigation. *ChemPhysChem* **18,** 1475–1480. https://doi.org/10.1002/cphc.201601143 (2017).

80. Righi, M. C., Zilibotti, G., Corni, S., Ferrario, M. & Bertoni, C. M. First-Principle Molecular Dynamics of Sliding Diamond Surfaces: Tribochemical Reactions with Water and Load Effects. *Journal of Low Temperature Physics* **185,** 174–182. https://doi.org/10.1007/s10909-016-1620-y (2016).

81. Ewen, J. P., Fernández, E. R., Smith, E. R. & Dini, D. in *Modeling and Simulation of Tribological Problems in Technology* (eds Paggi, M. & Hills, D.) 95–130 (Springer International Publishing, 2020). ISBN: 978-3-030-20377-1. https://doi.org/10.1007/978-3-030-20377-1_3.

82. Zilibotti, G., Corni, S. & Righi, M. C. Load-Induced Confinement Activates Diamond Lubrication by Water. *Phys. Rev. Lett.* **111,** 146101 (2013).

83. Kajita, S. & Righi, M. A fundamental mechanism for carbon-film lubricity identified by means of ab initio molecular dynamics. *Carbon* **103,** 193–199. ISSN: 0008-6223. http://www.sciencedirect.com/science/article/pii/S0008622316301713 (2016).

84. Loehlé, S. & Righi, M. C. Ab Initio Molecular Dynamics Simulation of Tribochemical Reactions Involving Phosphorus Additives at Sliding Iron Interfaces. *Lubricants* **6,** 31. http://dx.doi.org/10.3390/lubricants6020031 (2018).

85. Car, R. & Parrinello, M. Unified Approach for Molecular Dynamics and Density-Functional Theory. *Phys. Rev. Lett.* **55,** 2471–2474. https://link.aps.org/doi/10.1103/PhysRevLett.55.2471 (1985).

86. Tuckerman, M. E. Ab Initio Molecular Dynamics: Basic Concepts, Current Trends and Novel Applications. *Journal of Physics: Condensed Matter* **14,** R1297–R1355. https://doi.org/10.1088%5C%2F0953-8984%5C%2F14%5C%2F50%5C%2F202 (2002).

87. Warshel, A. & Karplus, M. Calculation of Ground and Excited State Potential Surfaces of Conjugated Molecules. I. Formulation and Parametrization. *Journal of the American Chemical Society* **94,** 5612–5625. https://doi.org/10.1021/ja00771a014 (1972).

88. Warshel, A. & Levitt, M. Theoretical Studies of Enzymic Reactions: Dielectric, Electrostatic and Steric Stabilization of the Carbonium Ion in the Reaction of Lysozyme. *Journal of Molecular Biology* **103,** 227–249. ISSN: 0022-2836. http://www.sciencedirect.com/science/article/pii/0022283676903119 (1976).

89. Senn, H. M. & Thiel, W. QM/MM Methods for Biomolecular Systems. *Angewandte Chemie International Edition* **48,** 1198–1229. https://onlinelibrary.wiley.com/doi/abs/10.1002/anie.200802019 (2009).

90. Restuccia, P., Ferrario, M. & Righi, M. C. Quantum Mechanics/Molecular Mechanics (QM/MM) Applied to Tribology: Real-Time Monitoring of Tribochemical Reactions of Water at Graphene Edges. *Computational Materials Science,* 109400. ISSN: 0927-0256. http://www.sciencedirect.com/science/article/pii/S0927025619306998 (2019).

91. Restuccia, P., Ferrario, M. & Righi, M. Monitoring Water and Oxygen Splitting at Graphene Edges and Folds: Insights into the Lubricity of Graphitic Materials. *Carbon* **156,** 93–103. ISSN: 0008-6223. http://www.sciencedirect.com/science/article/pii/S0008622319309455 (2020).

92. E, W. *Principles of Multiscale Modeling* ISBN: 9781107096547 (Cambridge University Press, 2011).

93. Spikes, H. Friction Modifier Additives. *Tribology Letters* **60,** 5. ISSN: 1573-2711. https://doi.org/10.1007/s11249-015-0589-z (2015).

94. Fry, B. M., Chui, M. Y., Moody, G. & Wong, J. S. Interactions between organic friction modifier additives. *Tribology International* **151,** 106438. http://www.sciencedirect.com/science/article/pii/S0301679X20302759 (2020).

95. Smith, H. G., Cantrell, T. L. & Peters, J. G. *Mineral oil compositions containing amidic acids or salts thereof* U.S. Patent 2699427. 1955.

96. Schick, J. W. & Kaminski, J. M. *Lubricant composition for reduction of fuel consumption in internal combustion engines* U.S. Patent 4304678. 1981.

97. Spikes, H. The History and Mechanisms of ZDDP. *Tribology Letters* **17,** 469–489. https://doi.org/10.1023/B:TRIL.0000044495.26882.b5 (2004).

98. Spikes, H. Low- and zero-sulphated ash, phosphorus and sulphur anti-wear additives for engine oils. *Lubrication Science* **20,** 103–136. https://onlinelibrary.wiley.com/doi/abs/10.1002/ls.57 (2008).

99. Spengler, G. & Weber, A. Über die Schmierfähigkeit organischer Molybdänverbindungen. *Chemische Berichte* **92,** 2163–2171. https://chemistry-europe.onlinelibrary.wiley.com/doi/abs/10.1002/cber.19590920931 (1959).

100. Feng, I.-M., Perilstein, W. L. & Adams, M. R. Solid Film Deposition and Non-Sacrificial Boundary Lubrication. *ASLE Transactions* **6,** 60–66. https://doi.org/10.1080/05698196308971999 (1963).

101. Grossiord, C. *et al.* MoS2 Single Sheet Lubrication by Molybdenum Dithiocarbamate. *Tribol. Int.* **31,** 737–743. ISSN: 0301-679X. http://www.sciencedirect.com/science/article/pii/S0301679X98000942 (1998).

102. Khaemba, D. N., Neville, A. & Morina, A. New Insights on the Decomposition Mechanism of Molybdenum DialkyldiThioCarbamate (MoDTC): a Raman Spectroscopic Study. *RSC Adv.* **6,** 38637–38646. http://dx.doi.org/10.1039/C6RA00652C (2016).

103. Okrent, E. H. The Effect of Lubricant Viscosity and Composition on Engine Friction and Bearing Wear. *ASLE Transactions* **4,** 97–108. https://doi.org/10.1080/05698196108972423 (1961).

104. Okrent, E. H. The Effect of Lubricant Viscosity and Composition on Engine Friction and Bearing Wear. II. *ASLE Transactions* **4,** 257–262. https://doi.org/10.1080/05698196108972437 (1961).

105. Müller, M., Topolovec-Miklozic, K., Dardin, A. & Spikes, H. A. The Design of Boundary Film-Forming PMA Viscosity Modifiers. *Tribology Transactions* **49,** 225–232. https://www.tandfonline.com/doi/abs/10.1080/05698190600614833 (2006).

106. Müller, M., Fan, J. & Spikes, H. Design of Functionalized PAMA Viscosity Modifiers to Reduce Friction and Wear in Lubricating Oils. *J. ASTM Int.* **4,** 1–10. https://doi.org/10.1520/JAI100956 (2007).

107. Mansot, J., Hallouis, M. & Martin, J. Colloidal antiwear additives 2. Tribological behaviour of colloidal additives in mild wear regime. *Colloids and Surfaces A: Physicochemical and Engineering Aspects* **75,** 25–31. http://www.sciencedirect.com/science/article/pii/0927775793804128 (1993).

108. Burris, D. L. & Sawyer, W. G. A low friction and ultra low wear rate PEEK/PTFE composite. *Wear* **261,** 410–418. http://www.sciencedirect.com/science/article/pii/S004316480500520X (2006).

109. Fatti, G., Righi, M. C., Dini, D. & Ciniero, A. First-Principles Insights into the Structural and Electronic Properties of Polytetrafluoroethylene in Its High-Pressure Phase (Form III). *The Journal of Physical Chemistry C* **123,** 6250–6255. https://doi.org/10.1021/acs.jpcc.8b11631 (2019).

110. Ciniero, A., Fatti, G., Righi, M. C., Dini, D. & Reddyhoff, T. A Combined Experimental and Theoretical Study on the Mechanisms Behind Tribocharging Phenomenon and the Influence of Triboemission. *Tribology Online* **14,** 367–374 (2019).

111. Zabinski, J. S., Donley, M. S., Prasad, S. V. & McDevitt, N. T. Synthesis and characterization of tungsten disulphide films grown by pulsed-laser deposition. *Journal of Materials Science* **29,** 4834–4839. https://doi.org/10.1007/BF00356530 (1994).

112. Muratore, C., Bultman, J., Aouadi, S. & Voevodin, A. In situ Raman spectroscopy for examination of high temperature tribological processes. *Wear* **270,** 140–145. http://www.sciencedirect.com/science/article/pii/S0043164810002693 (2011).

113. Bhushan, B. *Modern Tribology Handbook, Two Volume Set* chap. 24. ISBN: 9780849377877 (CRC Press, 2000).

114. Ramadanoff, D. & Glass, S. W. High-altitude brush problem. *Electrical Engineering* **63,** 825–829 (1944).

115. Berman, D., Deshmukh, S. A., Sankaranarayanan, S. K. R. S., Erdemir, A. & Sumant, A. V. Extraordinary Macroscale Wear Resistance of One Atom Thick Graphene Layer. *Advanced Functional Materials* **24,** 6640–6646. https://onlinelibrary.wiley.com/doi/abs/10.1002/adfm.201401755 (2014).

116. Huang, Y. *et al.* Wear evolution of monolayer graphene at the macroscale. *Carbon* **115,** 600–607. http://www.sciencedirect.com/science/article/pii/S0008622317300660 (2017).

117. Chen, Z., He, X., Xiao, C. & Kim, S. Effect of Humidity on Friction and Wear—A Critical Review. *Lubricants* **6,** 74. http://dx.doi.org/10.3390/lubricants6030074 (2018).

118. Scharf, T. W. & Prasad, S. V. Solid lubricants: a review. *Journal of Materials Science* **48,** 511–531. https://doi.org/10.1007/s10853-012-7038-2 (2013).

119. Eryilmaz, O. & Erdemir, A. Surface analytical investigation of nearly-frictionless carbon films after tests in dry and humid nitrogen. *Surface and Coatings Technology* **201,** 7401–7407. http://www.sciencedirect.com/science/article/pii/S0257897207001168 (2007).

120. Bec, S., Tonck, A., Georges, J. M. & Roper, G. W. Synergistic Effects of MoDTC and ZDTP on Frictional Behaviour of Tribofilms at the Nanometer Scale. *Tribol. Lett.* **17,** 797–809. ISSN: 1573-2711. https://doi.org/10.1007/s11249-004-8088-7 (2004).

121. Bouchet, M. D. B. *et al.* Mechanisms of MoS2 Formation by MoDTC in Presence of ZnDTP: Effect of Oxidative Degradation. *Wear* **258,** 1643–1650. ISSN: 0043-1648. http://www.sciencedirect.com/science/article/pii/S0043164804004326 (2005).

122. Okubo, H., Yonehara, M. & Sasaki, S. In Situ Raman Observations of the Formation of MoDTC-Derived Tribofilms at Steel/Steel Contact Under Boundary Lubrication. *Tribol. T.* **61,** 1040–1047. https://doi.org/10.1080/10402004.2018.1462421 (2018).

123. De Feo, M., Minfray, C., De Barros Bouchet, M. I., Thiebaut, B. & Martin, J. M. MoDTC Friction Modifier Additive Degradation: Correlation Between Tribological Performance and Chemical Changes. *RSC Adv.* **5,** 93786–93796. http://dx.doi.org/10.1039/C5RA15250J (2015).

124. Tang, Z. & Li, S. A Review of Recent Developments of Friction Modifiers for Liquid Lubricants (2007-Present). *Curr. Opin. Solid St. M.* **18,** 119–139. ISSN: 1359-0286. http://www.sciencedirect.com/science/article/pii/S1359028614000059 (2014).

125. Khaemba, D. N., Neville, A. & Morina, A. A Methodology for Raman Characterisation of MoDTC Tribofilms and Its Application in Investigating the Influence of Surface Chemistry on Friction Performance of MoDTC Lubricants. *Tribol. Lett.* **59,** 38. ISSN: 1573-2711. https://doi.org/10.1007/s11249-015-0566-6 (2015).

126. Feo, M. D. *et al.* MoDTC Lubrication of DLC-Involving Contacts. Impact of MoDTC Degradation. *Wear* **348-349,** 116–125. ISSN: 0043-1648. http://www.sciencedirect.com/science/article/pii/S0043164815005074 (2016).

127. Perdew, J. P., Burke, K. & Ernzerhof, M. Generalized Gradient Approximation Made Simple. *Phys. Rev. Lett.* **77,** 3865–3868. https://link.aps.org/doi/10.1103/PhysRevLett.77.3865 (1996).

128. Giannozzi, P. *et al.* QUANTUM ESPRESSO: a Modular and Open-source Software Project for Quantum Simulations of Materials. *J. Phys. Condens. Matter* **21,** 395502. http://stacks.iop.org/0953-8984/21/i=39/a=395502 (2009).

129. Giannozzi, P. *et al.* Advanced Capabilities for Materials Modelling with Quantum ESPRESSO. *J. Phys. Condens. Matter* **29,** 465901. http://stacks.iop.org/0953-8984/29/i=46/a=465901 (2017).

130. *Avogadro: an open-source molecular builder and visualization tool* (accessed Jun 8, 2019). http://avogadro.cc/.

131. Hanwell, M. D. *et al.* Avogadro: an Advanced Semantic Chemical Editor, Visualization, and Analysis Platform. *J. Cheminformatics* **4,** 17. ISSN: 1758-2946. https://doi.org/10.1186/1758-2946-4-17 (2012).

132. Weigend, F. & Ahlrichs, R. Balanced Basis Sets of Split Valence, Triple Zeta Valence and Quadruple Zeta Valence Quality for H to Rn: Design and Assessment of Accuracy. *Phys. Chem. Chem. Phys.* **7,** 3297–3305. http://dx.doi.org/10.1039/B508541A (2005).

133. Weigend, F. Accurate Coulomb-Fitting Basis Sets for H to Rn. *Phys. Chem. Chem. Phys.* **8,** 1057–1065. http://dx.doi.org/10.1039/B515623H (2006).

134. Frisch, M. J. *et al. Gaussian 09 Revision D.01* Gaussian Inc. Wallingford CT. 2013.

135. Varetto, U. *Molekel 5.4* (accessed June 8, 2019). https://ugovaretto.github.io/molekel/wiki/pmwiki.php/Main/DownloadBinary.html.

136. O'Boyle, N. M., Tenderholt, A. L. & Langner, K. M. cclib: a Library for Package-Independent Computational Chemistry Algorithms. *J. Comput. Chem.* **29,** 839–845. https://onlinelibrary.wiley.com/doi/abs/10.1002/jcc.20823 (2007).

137. Allen, F. H. *et al.* Tables of Bond Lengths Determined by X-Ray and Neutron Diffraction. Part 1. Bond Lengths in Organic Compounds. *J. Chem. Soc., Perkin Trans. 2,* S1–S19. http://dx.doi.org/10.1039/P298700000S1 (1987).

138. Coucouvanis, D., Toupadakis, A. & Hadjikyriacou, A. Synthesis of Thiomolybdenyl Complexes with $[Mo_2(S)_2(O)_2]^{2+}$ Cores and Substitutionally Labile Ligands. Crystal and Molecular Structure of the Tris(dimethylformamide)dioxotetrasulfidodimolybdenum Complex. *Inorg. Chem.* **27,** 3272–3273. https://doi.org/10.1021/ic00292a005 (1988).

139. Bhattacharyya, R. *et al.* Reaction of Tetraoxomolybdate^{2-} and Tetraoxotungstate^{2-} with Aqueous Polysulfides: Synthesis, Structure, and Electrochemistry of η2-polysulfido Complexes Containing a Bridging S,S M2O2S2^{2+} (M = Molybdenum, Tungsten) Core. *Inorg. Chem* **30,** 3948–3955. https://doi.org/10.1021/ic00020a031 (1991).

140. Onodera, T. *et al.* A Theoretical Investigation on the Dynamic Behavior of Molybdenum Dithiocarbamate Molecule in the Engine Oil Phase. *Tribology Online* **3,** 80–85. https://doi.org/10.2474/trol.3.80 (2008).

141. Onodera, T. *et al.* Development of a Quantum Chemical Molecular Dynamics Tribochemical Simulator and Its Application to Tribochemical Reaction Dynamics of Lubricant Additives. *Model. Simul. Mater. Sc.* **18,** 034009. https://iopscience.iop.org/article/10.1088/0965-0393/18/3/034009 (2010).

142. Becke, A. D. Density-Functional Thermochemistry. III. The Role of Exact Exchange. *J. Chem. Phys.* **98,** 5648–5652. https://aip.scitation.org/doi/10.1063/1.464913 (1993).

143. Lee, C., Yang, W. & Parr, R. G. Development of the Colle-Salvetti Correlation-Energy Formula into a Functional of the Electron Density. *Phys. Rev. B* **37,** 785–789. https://link.aps.org/doi/10.1103/PhysRevB.37.785 (1988).

144. Vosko, S. H., Wilk, L. & M., N. Accurate Spin-Dependent Electron Liquid Correlation Energies for Local Spin Density Calculations: a Critical Analysis. *Can. J. Phys.* **58,** 1200–1211. https://doi.org/10.1139/p80-159 (1980).

145. Stephens, P., Devlin, F., Chabalowski, C. & Frisch, M. J. Ab Initio Calculation of Vibrational Absorption and Circular Dichroism Spectra Using Density Functional Force Fields. *J. Phys. Chem.* **98,** 11623–11627. https://doi.org/10.1021/j100096a001 (1994).

146. Fatti, G., Restuccia, P., Calandra, C. & Righi, M. C. Phosphorus Adsorption on Fe(110): An Ab Initio Comparative Study of Iron Passivation by Different Adsorbates. *J. Phys. Chem. C* **122,** 28105–28112. https://doi.org/10.1021/acs.jpcc.8b0883 (2018).

147. Zilibotti, G., Righi, M. C. & Ferrario, M. Ab Initio Study on the Surface Chemistry and Nanotribological Properties of Passivated Diamond Surfaces. *Phys. Rev. B* **79,** 075420. https://link.aps.org/doi/10.1103/PhysRevB.79.075420 (2009).

148. Reuter, K. & Scheffler, M. Composition, Structure, and Stability of RuO_2 (110) as a Function of Oxygen Pressure. *Phys. Rev. B* **65,** 035406. https://link.aps.org/doi/10.1103/PhysRevB.65.035406 (2001).

149. Lozovoi, A., Alavi, A. & Finnis, M. Surface Energy and the Early Stages of Oxidation of NiAl(110). *Comput. Phys. Commun.* **137,** 174–194. ISSN: 0010-4655. http://www.sciencedirect.com/science/article/pii/S0010465501001783 (2001).

150. Sawyer, D. T., Howie, J. K. & Doub, W. H. Oxidation-Deduction Chemistry of Oxo- and Sulphldo-Bridged Binuclear Molybdenum(V) Complexes in Aprotic Media. *J. Less-Common Met.* **54,** 425–436. ISSN: 0022-5088. http://www.sciencedirect.com/science/article/pii/0022508877900650 (1977).

151. Tang, W., Sanville, E. & Henkelman, G. A Grid-Based Bader Analysis Algorithm Without Lattice Bias. *J. Phys. Condens. Matter* **21,** 084204. http://stacks.iop.org/0953-8984/21/i=8/a=084204 (2009).

152. Sanville, E., Kenny, S. D., Smith, R. & Henkelman, G. Improved Grid-Based Algorithm for Bader Charge Allocation. *J. Comput. Chem.* **28,** 899–908. https://onlinelibrary.wiley.com/doi/abs/10.1002/jcc.20575.

153. Henkelman, G., Arnaldsson, A. & Jónsson, H. A Fast and Robust Algorithm for Bader Decomposition of Charge Density. *Comp. Mater. Sci.* **36,** 354–360. ISSN: 0927-0256. http://www.sciencedirect.com/science/article/pii/S0927025605001849 (2006).

154. Yu, M. & Trinkle, D. R. Accurate and Efficient Algorithm for Bader Charge Integration. *J. Chem. Phys.* **134,** 064111. https://doi.org/10.1063/1.3553716 (2011).

155. Miertuš, S., Scrocco, E. & Tomasi, J. Electrostatic Interaction of a Solute with a Continuum. A Direct Utilizaion of Ab Initio Molecular Potentials for the Prevision of Solvent Effects. *Chem. Phys.* **55,** 117–129. ISSN: 0301-0104. http://www.sciencedirect.com/science/article/pii/0301010481850902 (1981).

156. Tomasi, J., Mennucci, B. & Cammi, R. Quantum Mechanical Continuum Solvation Models. *Chem. Rev.* **105,** 2999–3094. https://doi.org/10.1021/cr9904009 (2005).

157. Grimme, S. Semiempirical GGA-Type Density Functional Constructed with a Long-Range Dispersion Correction. *J. Comput. Chem.* **27,** 1787–1799. https://onlinelibrary.wiley.com/doi/abs/10.1002/jcc.20495 (2006).

158. Guegan, J., Southby, M. & Spikes, H. Friction Modifier Additives, Synergies and Antagonisms. *Tribology Letters* **67,** 83. ISSN: 1573-2711. https://doi.org/10.1007/s11249-019-1198-z (2019).

159. Espejo, C. *et al.* MoDTC Tribochemistry in Steel/Steel and Steel/Diamond-Like-Carbon Systems Lubricated With Model Lubricants and Fully Formulated Engine Oils. *Journal of Tribology* **141.** https://doi.org/10.1115/1.4041017 (2019).

160. Al-Jeboori, Y., Kosarieh, S., Morina, A. & Neville, A. Investigation of Pure Sliding and Sliding/Rolling Contacts in a DLC/Cast Iron System When Lubricated in Oils Containing MoDTC-Type Friction Modifier. *Tribology International* **122,** 23–37. ISSN: 0301-679X. http://www.sciencedirect.com/science/article/pii/S0301679X18300963 (2018).

161. Pan, Y. *et al.* Effect of Adding MoDTC on the Properties of Carbon Black Rubber and the Friction and Wear of Metal during Mixing Process. *Materials* **13,** 1071. https://doi.org/10.3390/ma13051071 (2020).

162. Khaemba, D. N., Azam, A., See, T., Neville, A. & Salehi, F. M. Understanding the Role of Surface Textures in Improving the Performance of Boundary Additives, Part I: Experimental. *Tribology International* **146,** 106243. ISSN: 0301-679X. https://doi.org/10.1016/j.triboint.2020.106243 (2020).

163. Guo, Z. *et al.* Interactions of Cu nanoparticles with conventional lubricant additives on tribological performance and some physicochemical properties of an ester base oil. *Tribology International* **141,** 105941. ISSN: 0301-679X. https://doi.org/10.1016/j.triboint.2019.105941 (2020).

164. Deshpande, P. *et al.* Effect of Adding TiO_2 Nanoparticles to a Lubricant Containing MoDTC on the Tribological Behavior of Steel/Steel Contacts Under Boundary Lubrication Conditions. *Tribology Letters* **68.** https://doi.org/10.1007/s11249-020-1278-0 (2020).

165. Grossiord, C. *et al.* Tribochemical Interactions Between Zndtp, Modtc and Calcium Borate. *Tribology Letters* **8,** 203–212. ISSN: 1573-2711. https://doi.org/10.1023/A:1019155822710 (2000).

166. Kasrai, M. *et al.* The Chemistry of Antiwear Films Generated by the Combination of ZDDP and MoDTC Examined by X-ray Absorption Spectroscopy. *Tribology Transactions* **41,** 69–77. https://doi.org/10.1080/10402009808983723 (1998).

167. Peeters, S., Restuccia, P., Loehlé, S., Thiebaut, B. & Righi, M. C. Characterization of Molybdenum Dithiocarbamates by First-Principles Calculations. *The Journal of Physical Chemistry A* **123,** 7007–7015. https://doi.org/10.1021/acs.jpca.9b03930 (2019).

168. Philippon, D. *et al.* Role of nascent metallic surfaces on the tribochemistry of phosphite lubricant additives. *Tribology International* **44,** 684–691. ISSN: 0301-679X. http://www.sciencedirect.com/science/article/pii/S0301679X0900351X (2011).

169. Daw, M. S. & Baskes, M. I. Embedded-Atom Method: Derivation and Application to Impurities, Surfaces, and Other Defects in Metals. *Phys. Rev. B* **29,** 6443–6453. https://link.aps.org/doi/10.1103/PhysRevB.29.6443 (1984).

170. Mendelev, M. I. *et al.* Development of New Interatomic Potentials Appropriate for Crystalline and Liquid Iron. *Philosophical Magazine* **83,** 3977–3994. https://doi.org/10.1080/14786430310001613264 (2003).

171. Plimpton, S. Fast Parallel Algorithms for Short-Range Molecular Dynamics. *Journal of Computational Physics* **117,** 1–19. ISSN: 0021-9991. http://www.sciencedirect.com/science/article/pii/S002199918571039X (1995).

172. Eder, S. J., Cihak-Bayr, U., Bianchi, D., Feldbauer, G. & Betz, G. Thermostat Influence on the Structural Development and Material Removal during Abrasion of Nanocrystalline Ferrite. *ACS Applied Materials & Interfaces* **9,** 13713–13725. https://doi.org/10.1021/acsami.7b01237 (2017).

173. Fleischauer, P. D. & Lince, J. R. A Comparison of Oxidation and Oxygen Substitution in MoS_2 Solid Film Lubricants. *Tribology International* **32,** 627–636. ISSN: 0301-679X. http://www.sciencedirect.com/science/article/pii/S0301679X99000882 (1999).

174. Peto, J. *et al.* Spontaneous Doping of the Basal Plane of MoS_2 Single Layers Through Oxygen Substitution Under Ambient Conditions. *Nature Chemistry* **10,** 1246–1251. ISSN: 1755-4349. https://doi.org/10.1038/s41557-018-0136-2 (2018).

175. Peeters, S., Restuccia, P., Loehlé, S., Thiebaut, B. & Righi, M. C. Tribochemical Reactions of MoDTC Lubricant Additives with Iron by Quantum Mechanics/Molecular Mechanics Simulations. *J. Phys. Chem. C* **124,** 13688–13694. https://doi.org/10.1021/acs.jpcc.0c02211 (2020).

176. Neville, A., Morina, A., Haque, T. & Voong, M. Compatibility Between Tribological Surfaces and Lubricant Additives—How Friction and Wear Reduction Can Be Controlled by Surface/Lube Synergies. *Tribology International* **40.** Tribology at the Interface: Proceedings of the 33rd Leeds-Lyon Symposium on Tribology (Leeds, 2006), 1680–1695. http://www.sciencedirect.com/science/article/pii/S0301679X07000230 (2007).

177. Graham, J., Spikes, H. & Korcek, S. The Friction Reducing Properties of Molybdenum Dialkyldithiocarbamate Additives: Part I — Factors Influencing Friction Reduction. *Tribology Transactions* **44,** 626–636. https://doi.org/10.1080/10402000108982504 (2001).

178. Cousseau, T., Ruiz Acero, J. S. & Sinatora, A. Tribological Response of Fresh and Used Engine Oils: The Effect of Surface Texturing, Roughness and Fuel Type. *Tribology International* **100,** 60–69. http://www.sciencedirect.com/science/article/pii/S0301679X15005241 (2016).

179. Khaemba, D. N. *Raman Spectroscopic Studies of Friction Modifier Molybdenum DialkyldiThioCarbamate (MoDTC)* http://etheses.whiterose.ac.uk/12923/. PhD thesis (University of Leeds, 2016).

180. Ossowski, T. & Kiejna, A. Oxygen Adsorption on Fe(110) Surface Revisited. *Surface Science* **637-638,** 35–41. http://www.sciencedirect.com/science/article/pii/S0039602815000618 (2015).

181. Spencer, M. J., Hung, A., Snook, I. K. & Yarovsky, I. Sulfur Adsorption on Fe(110): a DFT Study. *Surface Science* **540,** 420–430. http://www.sciencedirect.com/science/article/pii/S0039602803008835 (2003).

182. Rufael, T. S., Batteas, J. D. & Friend, C. The Influence of Surface Oxidation on the Reactions of Methanol on Fe(110). *Surf. Sci.* **384,** 156–167. http://www.sciencedirect.com/science/article/pii/S0039602897001970 (1997).

183. Perdew, J. P. Density Functional Theory and the Band Gap Problem. *Int. J. Quantum Chem.* **28,** 497–523. https://onlinelibrary.wiley.com/doi/abs/10.1002/qua.560280846 (1985).

184. Adamo, C. & Barone, V. Toward reliable density functional methods without adjustable parameters: The PBE0 model. *The Journal of Chemical Physics* **110,** 6158–6170. https://doi.org/10.1063/1.478522 (1999).

185. Sodhi, R. K. & Paul, S. An Overview of Metal Acetylacetonates: Developing Areas/Routes to New Materials and Applications in Organic Syntheses. *Catal. Surv. Asia* **22,** 31–62. https://doi.org/10.1007/s10563-017-9239-9 (2018).

186. Zhou, Z. *et al.* Graphene-Beaded Carbon Nanofibers with Incorporated Ni Nanoparticles as Efficient Counter-Electrode for Dye-sensitized Solar Cells. *Nano Energy* **22,** 558–563. http://www.sciencedirect.com/science/article/pii/S2211285516300143 (2016).

187. El-Mahalawy, A. M. Structural and Optical Characteristics of Nickel Bis(acetylacetonate) Thin Films as a Buffer Layer for Optoelectronic Applications. *Mat. Sci. Semicon. Proc.* **100,** 145–158. http://www.sciencedirect.com/science/article/pii/S1369800119302641 (2019).

188. Wang, J. *et al.* In Situ Formation of Molecular Ni-Fe Active Sites on Heteroatom-doped Graphene as a Heterogeneous Electrocatalyst Toward Oxygen Evolution. *Sci. Adv.* **4.** https://advances.sciencemag.org/content/4/3/eaap7970 (2018).

189. van Ommen, J., van Berkel, P. & Gellings, P. The Polymerization of Propadiene by $Ni(acac)_2$, C_3H_4, R_nAlX_{3-n} Catalysts. *Eur. Polym. J.* **16,** 745–752 (1980).

190. Endo, K. & Inukai, A. Polymerization of Methyl Methacrylate with $Ni(acac)_2$-methylaluminoxane Catalyst. *Polym. Int.* **49,** 110–114 (2000).

191. Utriainen, M., Kröger-Laukkanen, M., Johansson, L.-S. & Niinistö, L. Studies of Metallic Thin Film Growth in an Atomic Layer Epitaxy Reactor Using M(acac)$_2$ (M = Ni, Cu, Pt) Precursors. *Appl. Surf. Sci.* **157,** 151–158 (2000).

192. Gun'ko, V., Leboda, R., Skubiszewska-Zieba, J. & Rynkowski, J. Silica Gel Modified Due to Pyrolysis of Acetylacetone and Metal (Ti, Cr, Co, Ni, Zn, Zr) Acetylacetonates. *J. Colloid Interf. Sci.* **231,** 13–25. http://www.sciencedirect.com/science/article/pii/S0021979700971194 (2000).

193. Puniredd, S. R., Weiyi, S. & Srinivasan, M. Pd-Pt and Fe-Ni Nanoparticles Formed by Covalent Molecular Assembly in Supercritical Carbon Dioxide. *J. Colloid Interf. Sci.* **320,** 333–340. http://www.sciencedirect.com/science/article/pii/S0021979707016530 (2008).

194. Cui, L., Tarte, N. H. & Woo, S. I. Synthesis and Characterization of PMMA/MWNT Nanocomposites Prepared by in Situ Polymerization with Ni(acac)2 Catalyst. *Macromolecules* **42,** 8649–8654. https://doi.org/10.1021/ma901609r (2009).

195. Lin, Y. *et al.* Facile Synthesis of (Ni,Co)@(Ni,Co)$_x$Fe$_{3-x}$O$_4$ Core@shell Chain Structures and (Ni,Co)@(Ni,Co)$_x$Fe$_{3-x}$O$_4$/Graphene Composites with Enhanced Microwave Absorption. *RSC Adv.* **5,** 70849–70855. http://dx.doi.org/10.1039/C5RA12645B (2015).

196. Nasibulin, A. G., Moisala, A., Brown, D. P. & Kauppinen, E. I. Carbon Nanotubes and Onions from Carbon Monoxide Using Ni(acac)$_2$ and Cu(acac)$_2$ as Catalyst Precursors. *Carbon* **41,** 2711–2724. http://www.sciencedirect.com/science/article/pii/S0008622303003336 (2003).

197. Kishi, K., Ikeda, S. & Hirota, K. Infrared and Ultraviolet Studies of the Adsorption of Acetylacetone on Evaporated Iron and Nickel Films. *J. Phys. Chem.-US* **71,** 4384–4389. https://doi.org/10.1021/j100872a034 (1967).

198. Bullen, G. J., Mason, R. & Pauling, P. The Crystal and Molecular Structure of Bis(acetylacetonato)nickel (II). *Inorg. Chem.* **4,** 456–462. https://doi.org/10.1021/ic50026a005 (1965).

199. Korochentsev, V. V., Vovna, V. I., L'vov, I. B. & Shapkin, N. P. Electronic and Geometric Structure of the Protonated Forms of Nickel β-Diketonates. *Russ. J. Coord. Chem.+* **37,** 371–376. https://doi.org/10.1134/S1070328411040075 (2011).

200. Vovna, V. I., Korochentsev, V. V., Komissarov, A. A. & L'vov, I. B. Electronic Structure and Photoelectron Spectra of Nickel(II) Acetylacetonate. *Russ. J. Phys. Chem. B* **7,** 220–224. https://doi.org/10.1134/S1990793113030135 (2013).

201. Cauletti, C. & Furlani, C. He(I) Photoelectron Spectra of Bis(β-diketonate)nickel(II) Complexes and Their Mono- and Di-thio Analogues. *J. Electron Spectrosc.* **6,** 465–471. http://www.sciencedirect.com/science/article/pii/0368204875800338 (1975).

202. Lewis, F. D., Salvi, G. D., Kanis, D. R. & Ratner, M. A. Electronic Structure and Spectroscopy of Nickel(II), Palladium(II), and Platinum(II) acetylacetonate complexes. *Inorg. Chem.* **32,** 1251–1258. https://doi.org/10.1021/ic00059a037 (1993).

203. Al Kharboutly, M. *et al.* Mo(VI) dithiocarbamate with no pre-existing Mo-S-Mo core as an active lubricant additive. *Tribology International* **154,** 106690. http://www.sciencedirect.com/science/article/pii/S0301679X20305156 (2021).

204. Botu, V., Batra, R., Chapman, J. & Ramprasad, R. Machine Learning Force Fields: Construction, Validation, and Outlook. *The Journal of Physical Chemistry C* **121,** 511–522. https://doi.org/10.1021/acs.jpcc.6b10908 (2017).

205. Jinnouchi, R., Karsai, F. & Kresse, G. On-the-fly machine learning force field generation: Application to melting points. *Phys. Rev. B* **100,** 014105. https://link.aps.org/doi/10.1103/PhysRevB.100.014105 (2019).

206. Stewart, J. A. & Spearot, D. E. Atomistic Simulations of Nanoindentation on the Basal Plane of Crystalline Molybdenum Disulfide (MoS2). *Modelling and Simulation in Materials Science and Engineering* **21,** 045003. https://doi.org/10.1088%5C%2F0965-0393%5C%2F21%5C%2F4%5C%2F045003 (2013).

207. Berendsen, H. J. C., Grigera, J. R. & Straatsma, T. P. The Missing Term in Effective Pair Potentials. *The Journal of Physical Chemistry* **91,** 6269–6271. https://doi.org/10.1021/j100308a038 (1987).

208. Liang, T., Phillpot, S. R. & Sinnott, S. B. Parametrization of a Reactive Many-body Potential for Mo-S Systems. *Phys. Rev. B* **79,** 245110. https://link.aps.org/doi/10.1103/PhysRevB.79.245110 (24 2009).

209. Liang, T., Phillpot, S. R. & Sinnott, S. B. Erratum: Parametrization of a reactive many-body potential for Mo–S systems [Phys. Rev. B 79, 245110 (2009)]. *Phys. Rev. B* **85,** 199903. https://link.aps.org/doi/10.1103/PhysRevB.85.199903 (19 2012).